

2013

A New Class of Improved Bandwidth Planar Ultrawideband Modular Antenna (puma) Arrays Scalable to mm-Waves

John Logan

University of Massachusetts Amherst

Follow this and additional works at: <https://scholarworks.umass.edu/theses>



Part of the [Electrical and Electronics Commons](#), [Electromagnetics and Photonics Commons](#), and the [Systems and Communications Commons](#)

Logan, John, "A New Class of Improved Bandwidth Planar Ultrawideband Modular Antenna (puma) Arrays Scalable to mm-Waves" (2013). *Masters Theses 1911 - February 2014*. 1060.

Retrieved from <https://scholarworks.umass.edu/theses/1060>

This thesis is brought to you for free and open access by ScholarWorks@UMass Amherst. It has been accepted for inclusion in Masters Theses 1911 - February 2014 by an authorized administrator of ScholarWorks@UMass Amherst. For more information, please contact scholarworks@library.umass.edu.

**A NEW CLASS OF IMPROVED BANDWIDTH PLANAR
ULTRAWIDEBAND MODULAR ANTENNA (PUMA)
ARRAYS SCALABLE TO MM-WAVES**

A Thesis Presented

by

JOHN LOGAN

Submitted to the Graduate School of the
University of Massachusetts Amherst in partial fulfillment
of the requirements for the degree of

MASTER OF SCIENCE IN ELECTRICAL AND COMPUTER ENGINEERING

May 2013

Electrical and Computer Engineering

**A NEW CLASS OF IMPROVED BANDWIDTH PLANAR
ULTRAWIDEBAND MODULAR ANTENNA (PUMA)
ARRAYS SCALABLE TO MM-WAVES**

A Thesis Presented

by

JOHN LOGAN

Approved as to style and content by:

Marinos N. Vouvakis, Chair

Do-Hoon Kwon, Member

Robert W. Jackson, Member

Christopher V. Hollot, Department Head
Electrical and Computer Engineering

ABSTRACT

A NEW CLASS OF IMPROVED BANDWIDTH PLANAR ULTRAWIDEBAND MODULAR ANTENNA (PUMA) ARRAYS SCALABLE TO MM-WAVES

MAY 2013

JOHN LOGAN

BSEE, UNIVERSITY OF RHODE ISLAND

MSECE, UNIVERSITY OF MASSACHUSETTS AMHERST

Directed by: Professor Marinos N. Vouvakis

A new class of Planar Ultrawideband Modular Antenna (PUMA) arrays, termed PUMAv3, is introduced to offer improved performance and further meet demand needs for multifunctional systems. PUMAv3 extends the frequency scalability of PUMA arrays to mm-waves (approximately 50 GHz) and improves bandwidth by 50% without the use of a matching network or external baluns. The major enabling technical innovation is the advent of a new common-mode mitigation mechanism that relies upon capacitively-loaded shorting vias to push broadside catastrophic resonances below the operating band without inhibiting low-end bandwidth performance. Ridged waveguide models are employed to explain the operational principles and accurately predict the location of the common-mode frequency within the new array topology. Additionally, the superstrate loading scheme is split into two exclusive layers to enhance broadside and wide angle impedance levels while maintaining the highest frequency at 97% of the grating lobe frequency and reducing the overall array

profile by up to 30%. The PUMAv3 also retains the attractive practical advantages inherent to the PUMA array family: aperture modularity, direct 50-ohm feeding, and low-cost planar multilayer PCB fabrication. Infinite array full-wave simulations of a dual-polarized PUMAv3 satisfying manufacture guidelines suggest 10.6-47.6 GHz (4.5:1) operation with strong VSWR levels out to 45 degrees, high port isolation and low cross-polarization.

TABLE OF CONTENTS

	Page
ABSTRACT	iii
LIST OF TABLES	vii
LIST OF FIGURES	viii
 CHAPTER	
1. INTRODUCTION	1
1.1 Problem Statement	1
1.2 Significance	2
1.2.1 Multi-Band, Multifunctional Systems	2
1.2.2 Wide Instantaneous Bandwidth Applications	5
1.3 Previous Work	8
1.3.1 Low-Profile Vertically-Integrated UWB Arrays	8
1.3.2 “Quasi-Planar” UWB Arrays	12
1.3.3 PUMA Arrays	15
1.4 Challenges	17
1.5 Contributions	19
1.6 Thesis Overview	22
 2. COMMON-MODE PHENOMENA IN UNBALANCED FED DUAL-POLARIZED UWB DIPOLE ARRAYS	 25
2.1 Introduction	25
2.2 Direct Unbalanced Feeding	25
2.3 Unbalanced Feeding with Shorting Vias (PUMAv1 and v2)	31
2.4 Conclusion	36

LIST OF TABLES

Table		Page
1.1	Performance evolution of PUMA arrays.	23
3.1	Calculated common-mode frequencies (f_{cm}) and dominant TE_{10} mode cut-off frequencies (f_c) for various plate radii (r_p) and ridge discontinuity gaps (d) within unbalanced-fed dual-polarized dipole infinite array and ridged waveguides of similar structure.	65
4.1	4.5:1 50 GHz Dual-pol PUMAv3 array dimensions	76

LIST OF FIGURES

Figure	Page
1.1 Comparison of fractional instantaneous bandwidths (FBW $[\%] = \frac{f_{high} - f_{low}}{f_{mid}} \times 100$) of several established array technologies over different operating frequencies, including the stacked microstrip patch, Vivaldi, and PUMA arrays. (a) Available options at frequencies up to 21 GHz; (b) Available options at frequencies up to 45 GHz.	2
1.2 VSWR chart over a wide frequency range highlighting several narrowband applications that could be serviced by a single ultrawideband aperture as opposed to multiple narrowband sub-systems.	3
1.3 A photo taken of the USS George Washington mast highlighting its utilization of several antennas in a dense, cluttered area.	4
1.4 A picture of an RC-12N Guardrail aircraft, specifically created to intercept enemy communications for intelligence, surveillance, and reconnaissance (ISR) at several frequencies through the use of many narrowband antennas.	4
1.5 A soldier prepares an Unmanned Aerial Vehicle (UAV) for an Afghanistan flight, where future plans include utilizing UAVs as flying nodes in mm-wave communication networks with steerable, high-bandwidth antennas [16].	6
1.6 A special operations team employing a UWB through-wall imaging radar for tactical use [20].	6
1.7 A soldier using a handheld UWB device to scan for underground threats such as unexploded ordinances (UXO) [23].	7
1.8 Artistic depiction of a multi-beam array utilized for radio telescropy [27].	7
1.9 Depiction of a coincident phase center dipole array with orthogonally integrated Marchand baluns [32].	9

1.10	An isometric view of a 9×9 Bunny-Ear array operating over 1-5 GHz [30].	9
1.11	Unit cells of a dual-pol. Balanced Antipodal Vivaldi Antenna (DpBAVA) array and its doubly-mirrored extension (DmDpBAVA) [36].	10
1.12	Isometric views of Banyan Tree Antenna (BTA) arrays utilizing shorting strips connected to the radiating arms [38]. (a) Single-polarized configuration; (b) Dual-polarized configuration.	10
1.13	A 10:1 dual-polarized BAVA array [39]. (a) Unit cell of a single-polarized array; (b) 8×9 prototype of a dual-polarized configuration.	11
1.14	Current Sheet Antenna (CSA) arrays [40]. (a) Single-polarized CSA array highlighting the interdigitated capacitors to achieve high inter-element coupling; (b) Dual-polarized CSA array aperture and feed network designed for operation over 2-18 GHz.	12
1.15	A Fragmented Aperture Array (FAA) optimized for operation over 1.25 to 10 GHz [42]. (a) A 2×2 FAA; (b) A 17×8½ FAA mounted on a brass plate for measurement.	13
1.16	A single-polarized long slot array designed for operation over 0.2 to 2 GHz while backed by a ferrite loaded ground plane [40]. (a) Top view; (b) Side view of the array with a 5 cm air gap.	14
1.17	Cross-sectional view of a typical quasi-planar UWB array unit cell as depicted from [1].	14
1.18	Three fabricated 8×8 PUMAv1 modules that operate over 7-21 GHz with a modular architecture while connected to a standard unbalanced 50Ω interface [1].	16
1.19	Full-wave model of the 1-5 GHz PUMAv2 unit cell with its microstrip backplane matching network designed within [1]. (a) Top view; (b) Isometric view.	17

1.20	Comparison of fractional instantaneous bandwidths (FBW $[\%] = \frac{f_{high} - f_{low}}{f_{mid}} \times 100$) of several established array technologies over different operating frequencies, including the stacked microstrip patch, Vivaldi, PUMAv1, and PUMAv3 arrays. (a) Available options at frequencies up to 21 GHz; (b) Available options at frequencies up to 45 GHz.	22
2.1	Top view of an unbalanced-fed dual-polarized dipole array. The common-mode resonant dimensions intrinsically reduced to its unit cell dimensions, D_x and D_y	27
2.2	Magnitude of the self active reflection coefficient, Γ_{11}^a , of an unbalanced-fed dual-polarized dipole array compared to its balanced-fed equivalent.	28
2.3	Magnitude of the active port transmission coefficient, Γ_{21}^a , of an unbalanced-fed dual-polarized dipole array compared to its balanced-fed equivalent.	29
2.4	Co- and cross-polarization (Ludwigs 3rd definition [59]) radiated power vs. frequency of an unbalanced-fed dual-polarized dipole array.	30
2.5	Top view of an unbalanced-fed dual-polarized dipole array with shorting vias. The common-mode resonant dimensions are reduced to its unit cell dimensions, L_{co} and L_{cx}	32
2.6	Magnitude of the self active reflection coefficient, Γ_{11}^a , of an unbalanced-fed dual-polarized dipole array with shorting vias compared to its balanced-fed equivalent.	33
2.7	Magnitude of the active port transmission coefficient, Γ_{21}^a , of an unbalanced-fed dual-polarized dipole array with shorting vias compared to its balanced-fed equivalent.	34
2.8	Co- and cross-polarization (Ludwigs 3rd definition [59]) radiated power vs. frequency of an unbalanced-fed dual-polarized dipole array with shorting vias.	35

2.9	Common-mode manifestation in infinite dual-polarized unbalanced fed dipole arrays with (PUMAv1 and v2) and without (direct unbalanced feeding) shorting vias. (a) Broadside active reflection and orthogonal port transmission (isolation) coefficients; (b) Broadside co- and cross-polarized (Ludwig's 3rd definition [59]) radiated power.	37
3.1	PUMAv3 topological viewpoints (not to scale). (a) Cross-sectional view of a $1 \times 2 \times 2$ PUMAv3 array displaying via connections and dielectric layers stack-up; (b) Top view of a $3 \times 3 \times 2$ array's metallized components and perforated dielectric layers; (c) Cross-sectional view of a $3 \times 3 \times 2$ PUMAv3 between feed lines. 40	
3.2	Waveguide vs. unbalanced-fed dual-polarized dipole array structural and cut-off/common-mode frequency comparisons for when $a = D_x \approx 6mm$, $b = H \approx 3mm$, and both topologies are filled with a homogenous dielectric material of $\epsilon_r = 1.96$	43
3.3	Waveguide vs. PUMAv1 (unbalanced-fed dual-polarized dipole array) structural and cut-off/common-mode frequency comparisons with shorting pins/vias for when $a = D_x \approx 6mm$, $b = H \approx 3mm$, $w = 1mm$, and both topologies are filled with a homogenous dielectric material of $\epsilon_r = 1.96$	44
3.4	Ridged waveguide vs. a new idea of unbalanced-fed dual-polarized dipole array with metallic disconnected vias with unknown properties. Ideally, f_{cm} will be shifted beneath the low-end operating edge of the band near $f_{cut-off}$ of the ridged waveguide without limiting the low band-edge by inducing loop modes.	45
3.5	A standard ridged waveguide with important labeled dimensions.	46
3.6	Charts of individual functions and their differences within the ridged waveguide equation for varying waveguide parameters s , L , and d and a fixed a and b (6mm and 3mm, respectively) versus the relative guide wavelength in the \hat{x} direction and frequency. (a) $s = 0.2L$; (b) $s = 0.5L$; (c) $s = 0.8L$	48
3.7	Ridged waveguides and discontinuity susceptance [57]. (a) Chart of the discontinuity susceptance, B/Y_{01} , within a ridged waveguide, for varying b versus $\frac{b'}{b}$; (b) Cross-section from a forward view of a ridged waveguide; (c) Side-view of a ridged waveguide with the discontinuity dimension b'	49

3.8	Variations of the ridge height (b/d ratio) and its effect on the propagation of the TE_{10} mode.	50
3.9	A ridged waveguide with a loaded capacitance (discontinuity susceptance) and labeled dimensions. (a) Straightforward circuit representation to heighten the discontinuity susceptance; (b) Realized implementation to heighten the discontinuity susceptance.	52
3.10	Variations of the waveguide ridge parallel plate ($\frac{2L+s}{2c}$ ratio) for a static ridge height and its effect on the propagation of the TE_{10} mode	53
3.11	Comparisons of different feeding techniques for unbalanced fed arrays and their broadside VSWR vs. frequency. (a) No via; (b) Connected via (PUMAv1); (c) Broadside VSWR vs. frequency; (d) Desired broadside VSWR vs. frequency combining the better low-end when no vias are present and better high-end when vias are present (seen in (c)).	55
3.12	Different viewpoints of the PUMAv3 metallized components attempting to embody a ridged waveguide with a disconnected via. (a) Isometric view; (b) Side view with critical dimensions labeled.	56
3.13	Effect of varying the height of a disconnected via for a PUMAv3 array on the broadside VSWR. The via is centered underneath the dipole tips (centered on the unit cell). The common-mode frequency shifts downwards with increasing via height, whereas the low end region remains unaffected.	58
3.14	Top-view of a PUMAv3 unit cell highlighting the important capacitive junctions between the disconnected via and dipole arms.	59
3.15	Different viewpoints of the PUMAv3 metallized components with the added metallic plate onto the disconnected via. (a) Isometric view; (b) Side view with critical dimensions labeled.	60
3.16	Infinite array VSWR performance for a PUMAv3 array with varying disconnected via heights and plate radii. (a) $h/H = 0.39$; (b) $h/H = 0.58$; (c) $h/H = 0.76$; (d) $h/H = 0.95$	61

3.17	Infinite dual-polarized array broadside active reflection and orthogonal-port transmission coefficient magnitudes for different via configurations. (a) Reflection coefficient (return-loss); (b) Orthogonal port transmission coefficient (isolation).	63
3.18	An unbalanced-fed dual-polarized dipole array with capacitively-loaded via (PUMAv3) translated to a ridged waveguide model with identical critical dimensions. (a) Unbalanced-fed dual-polarized dipole array with capacitively-loaded via (PUMAv3); (b) Ridged waveguide.	65
3.19	Comparison of common-mode frequencies in unbalanced-fed infinite dual-polarized dipole arrays with capacitively-loaded vias and dominant TE_{10} mode cut-off frequencies in ridged waveguides for varying ridge discontinuity heights d and plate radius $r_p = \lambda/24$. The critical dimensions of the two are identical as seen in Fig. 3.18.	66
3.20	Comparison of common-mode frequencies in unbalanced-fed infinite dual-polarized dipole arrays with capacitively-loaded vias and dominant TE_{10} mode cut-off frequencies in ridged waveguides for varying ridge discontinuity heights d and plate radius $r_p = \lambda/12$. The critical dimensions of the two are identical as seen in Fig. 3.18	67
3.21	Comparison of common-mode frequencies in unbalanced-fed infinite dual-polarized dipole arrays with capacitively-loaded vias and dominant TE_{10} mode cut-off frequencies in ridged waveguides for varying ridge discontinuity heights d and plate radius $r_p = \lambda/8$. The critical dimensions of the two are identical as seen in Fig. 3.18	68
3.22	PUMA dielectric compositions with standard rectangular dipoles, omitting the metallization layer, modified from [1]. (a) PUMAv1 and PUMAv2 uniform superstrate composition; (b) PUMAv3 multi-layer superstrates, enabling more refined tuning for WAIM by breaking the superstrate into two different permittivity layers with different perforation sizes, D_1 and D_2	69
3.23	Magnitude of the active reflection coefficient, $ \Gamma_a $, versus E-/H-plane scan angles at $f_{high} = 24.05$ GHz ($98\%f_g$) for varying the perforation diameter D_1 with fixed permittivities ($\epsilon_{r1} = 4.5$, $\epsilon_{r2} = 1.96$), thicknesses ($t_1 = t_2 = t_4/2$), and D_2 (5mm).	71

4.1	Viewpoints of a PUMAv3 array unit cell. (a) Top view; (b) Cross-sectional view.	74
4.2	Infinite PUMAv3 array VSWR vs. frequency for varying scan angles. (a) E-plane scan; (b) H-plane scan.	77
4.3	Infinite PUMAv3 array co- and cross-polarization (Ludwig's 3rd definition [59]) radiated power vs. frequency for various scan planes.	78
4.4	Infinite PUMAv3 array broadside realized gain (incorporates mismatch, port coupling, dielectric, and conductor losses) and ideal directivity vs. frequency.	79
4.5	Simulated co-/cross-polarized normalized E-plane element patterns for different frequencies ($f = 15, 30, 45$ GHz).	80
4.6	Simulated co-/cross-polarized normalized D-plane embedded element patterns for different frequencies ($f = 15, 30, 45$ GHz).	80
4.7	Simulated co-/cross-polarized normalized H-plane embedded element patterns for different frequencies ($f = 15, 30, 45$ GHz).	81

CHAPTER 1

INTRODUCTION

1.1 Problem Statement

This work develops a new class of low-cost, improved bandwidth, mm-wave scalable Planar Ultrawideband Modular Antenna (PUMA) arrays to meet demand needs for future multifunctional systems and other phased array applications, e.g. communications, sensing, electronic warfare. Several ultrawideband (UWB) array technologies have been proposed to service such functionalities, but, although exhibiting large instantaneous bandwidths, remain expensive to fabricate and difficult to scale above X-band due to design complexities. To circumvent these issues, PUMA arrays [1–5] were developed and fabricated as a low-cost, modular, dual-polarized UWB alternative that displayed high-performance near the lower limit of K-band at 21 GHz. Despite the practical advantages offered by PUMA arrays, the frequency scalability and bandwidth still remained limited when compared to other efficient state-of-the-art array technologies. As shown in Fig. 1.1(a) and Fig. 1.1(b), Vivaldi arrays [6], although expensive, are able to achieve higher bandwidths up to K_u -band, whereas low-cost microstrip-printed stacked patch arrays [7] with minimal relative bandwidth are able to exclusively achieve operation at extremely-high frequencies. Ultimately, a void exists in the availability of mm-wave and low-cost/high-bandwidth UWB array technology, and the PUMAv3 array introduced in this work seeks to become a solution to these issues.

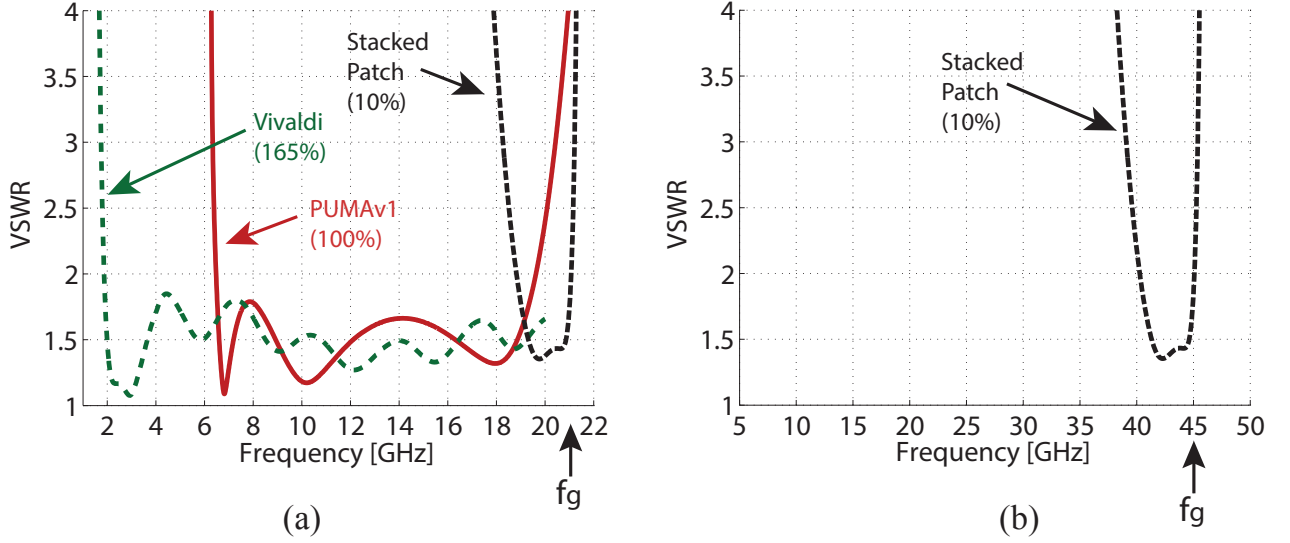


Figure 1.1. Comparison of fractional instantaneous bandwidths (FBW $[\%] = \frac{f_{high} - f_{low}}{f_{mid}} \times 100$) of several established array technologies over different operating frequencies, including the stacked microstrip patch, Vivaldi, and PUMA arrays. (a) Available options at frequencies up to 21 GHz; (b) Available options at frequencies up to 45 GHz.

1.2 Significance

1.2.1 Multi-Band, Multifunctional Systems

An increasing interest in programmable RF front-ends persists in modern research under initiatives such as DARPA's RF-FPGA program [8], the Navy's Advanced Multifunction RF Concept [9], and various software-defined radio efforts [10–12]. The underlying theme shared between these research directions is the consolidation of multiple sub-systems serving different purposes into a single or small number of systems to minimize real estate, weight, radar cross section (RCS), electromagnetic interference (EMI), and cost. These sub-systems realistically support narrowband applications extending over a wide range of frequencies up into extremely-high frequencies (EHF), including radionavigation, radio astronomy, communications, terrestrial research, etc., as shown in Fig. 1.2, where ideally a UWB array with high instantaneous bandwidth could service each operation through a single aperture. For instance, tightly-packed

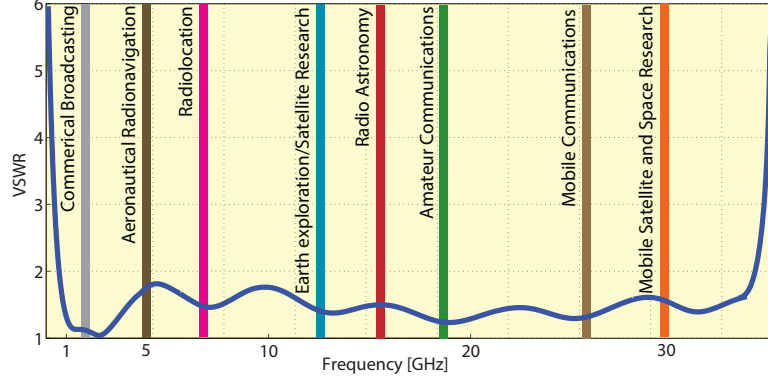


Figure 1.2. VSWR chart over a wide frequency range highlighting several narrowband applications that could be serviced by a single ultrawideband aperture as opposed to multiple narrowband sub-systems.

networks of antennas serving just a portion of these narrowband applications are highlighted by the cluttered ‘antenna forests’ or ‘antenna farms’ upon the USS George Washington [13] in Fig. 1.3 and the RC-12N Guardrail aircraft [14] in Fig. 1.4 (quoted to “look like a dog that just finished chasing a family of porcupines”).

Dual-polarized UWB arrays are the cornerstone components of adaptive/reconfigurable RF systems due to their frequency, pattern, and polarization adaptability and flexibility. Despite that, UWB arrays continue to have expensive fabrication processes, complicated integration with RF front-ends, and electrical limitations arising from design complexities that also inhibits their frequency scalability. As a result, the cost-efficient concept behind multifunctional systems is still difficult to realize due to the expensive nature of UWB arrays and precludes their operation at mm-wave frequencies. If this work is successful, multifunctional systems will become a reality at mm-waves to enable more efficient use of the RF spectrum and furthermore remain low-cost with higher instantaneous bandwidth, proliferating their use to commercial applications and improving performance for military applications, e.g. EMI, RCS, etc.



Figure 1.3. A photo taken of the USS George Washington mast highlighting its utilization of several antennas in a dense, cluttered area.



Figure 1.4. A picture of an RC-12N Guardrail aircraft, specifically created to intercept enemy communications for intelligence, surveillance, and reconnaissance (ISR) at several frequencies through the use of many narrowband antennas.

1.2.2 Wide Instantaneous Bandwidth Applications

Apart from multifunctional systems, the demand for battlefield instantaneous bandwidth continues to grow at an exponential rate. Outlined by several DARPA programs [15–17], it is of critical importance to provide high instantaneous bandwidth communications for troops in remote forward operating locations, which requires the development of efficient, steerable mm-wave antennas to aid intelligence, surveillance, and reconnaissance (ISR) assets and communication links. Specifically, DARPA aims to have small Unmanned Aerial Vehicles (UAVs), like the one shown in Fig. 1.5, serve as flying nodes on the mobile high-speed backbone of a backhaul network by equipping them with mm-wave, high-bandwidth, steerable antennas [16]. Furthermore, the Office of Naval Research remains interested in efficient, wideband electronic attack (EA) transmitter systems operating through mm-waves that utilize UWB steerable apertures [18]. UWB array technology also finds employment with sensing applications such as through-wall imaging for first-responder rescue operations [19, 20] as shown in Fig. 1.6, ground penetrating radars for underground exploration [21–23] and unexploded ordinance (UXO) detection [24] like that displayed in Fig. 1.7, and astronomy/radio telescope [25–27] as depicted in Fig. 1.8. Additionally, considerable attention has been drawn to the utilization of UWB arrays for the detection of early-stage breast cancer [28, 29].

In addition to military and defense employment, the low-cost, mm-wave scalable UWB array to be introduced in this work also aims to extend availability to commercial customers. Due to its improved bandwidth and extended frequency scalability, these affordable arrays could provide a viable solution for a condensed aperture servicing mm-wave communication with satellites, Wi-Fi, and radio networks over a broad range. Lastly, the work to be presented enters the domain of the virtually unexplored area of research of mm-wave UWB arrays and seeks to enable mm-wave research directions through its affordability and efficient, high-performance.



Figure 1.5. A soldier prepares an Unmanned Aerial Vehicle (UAV) for an Afghanistan flight, where future plans include utilizing UAVs as flying nodes in mm-wave communication networks with steerable, high-bandwidth antennas [16].



Figure 1.6. A special operations team employing a UWB through-wall imaging radar for tactical use [20].



Figure 1.7. A soldier using a handheld UWB device to scan for underground threats such as unexploded ordinances (UXO) [23].



Figure 1.8. Artistic depiction of a multi-beam array utilized for radio telescope [27].

1.3 Previous Work

Various UWB array technologies have been explored over the past few decades. Flared-notch (Vivaldi) radiators are perhaps the most well-known wideband array element, but modern research directions demand more cost-efficient and low-profile options for low-cost conformal platform integration and improved scan performance (namely in the diagonal plane). This section will acknowledge previous work accomplished in an effort to achieve low-profile UWB arrays.

1.3.1 Low-Profile Vertically-Integrated UWB Arrays

Several low-profile ($h \leq \lambda_{high}/2$, where λ_{high} is the highest operating wavelength), vertically-integrated arrays have been developed within the decade to deliver wide-scan UWB performance. Such arrays include the Bunny-ear [30], printed dipoles with integrated baluns [31, 32], and balanced antipodal Vivaldi antennas (BAVA) [33–36]. The printed dipole arrays utilize Marchand baluns to achieve wideband impedance matches of 6:1 in single-polarized configurations [31], but predicted bandwidth for a dual-polarized assembly shown in Fig. 1.9 with coincident phase center in an infinite environment was reported to drop to approximately 3:1 [32]. The Bunny-ear array displayed within Fig. 1.10 is able to achieve bandwidths of 5:1 by connecting film resistors between the elements and the ground plane to dissipate problematic resonances [37] while being fed through external baluns/hybrids. Similarly, earlier versions of BAVA and its doubly-mirrored extension (DmBAVA) shown in Fig. 1.11 are able to maintain up to 5:1 bandwidths while also utilizing external baluns/hybrids in the feeding network.

To eliminate the necessity of external baluns/hybrids in these arrays, the Banyan Tree Antenna (BTA) [38] array was developed to achieve a 4:1 bandwidth when fed directly with an unbalanced 50Ω feed line by mitigating in-band common-mode resonances with shorting strips connected to the radiating arms as shown in Fig. 1.12.

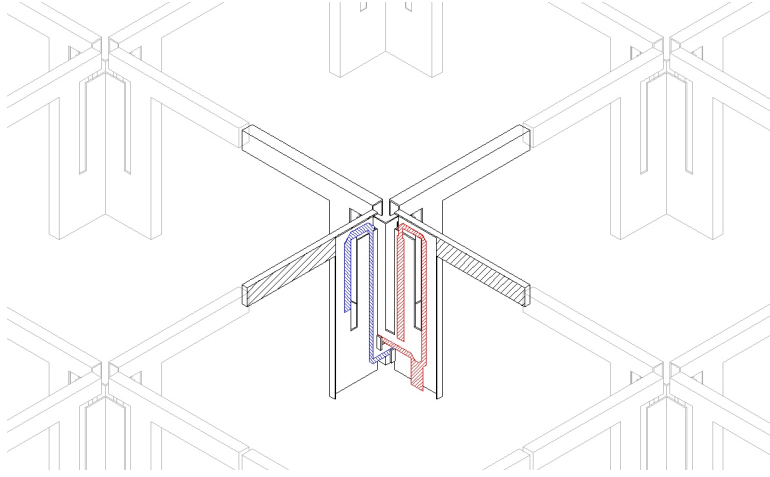


Figure 1.9. Depiction of a coincident phase center dipole array with orthogonally integrated Marchand baluns [32].

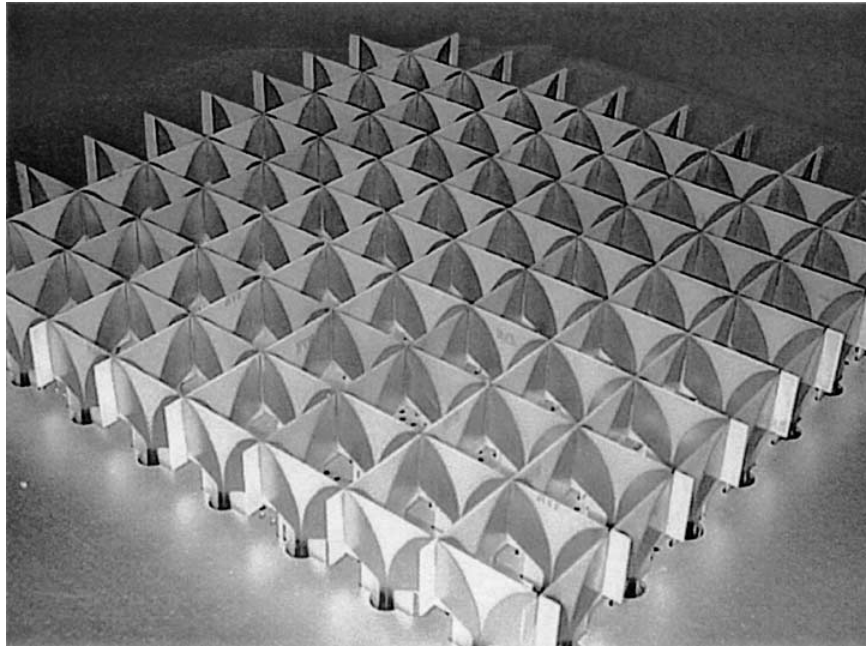


Figure 1.10. An isometric view of a 9×9 Bunny-Ear array operating over 1-5 GHz [30].

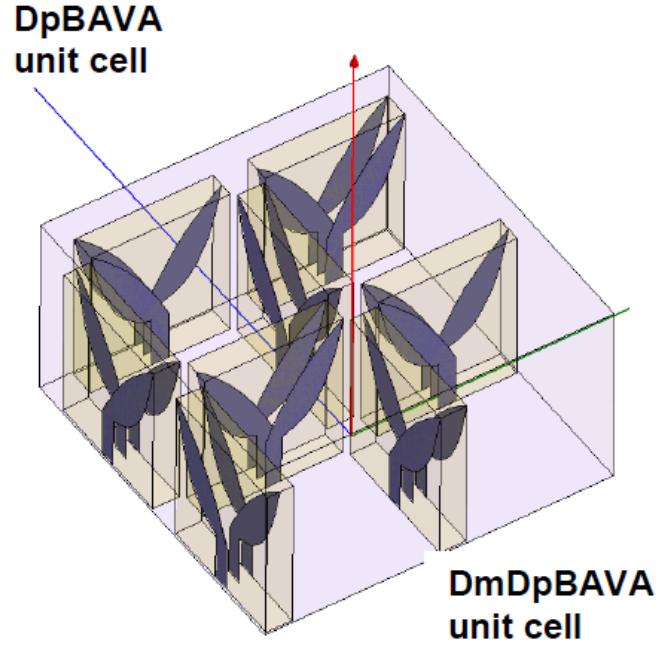


Figure 1.11. Unit cells of a dual-pol. Balanced Antipodal Vivaldi Antenna (DpBAVA) array and its doubly-mirrored extension (DmDpBAVA) [36].

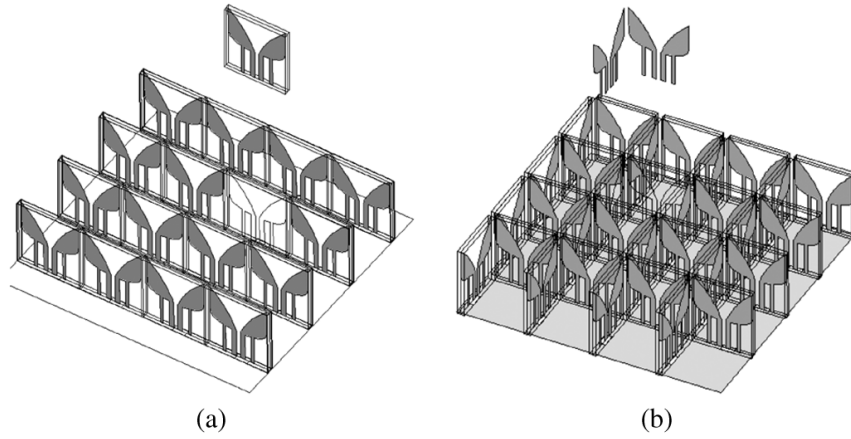


Figure 1.12. Isometric views of Banyan Tree Antenna (BTA) arrays utilizing shorting strips connected to the radiating arms [38]. (a) Single-polarized configuration; (b) Dual-polarized configuration.

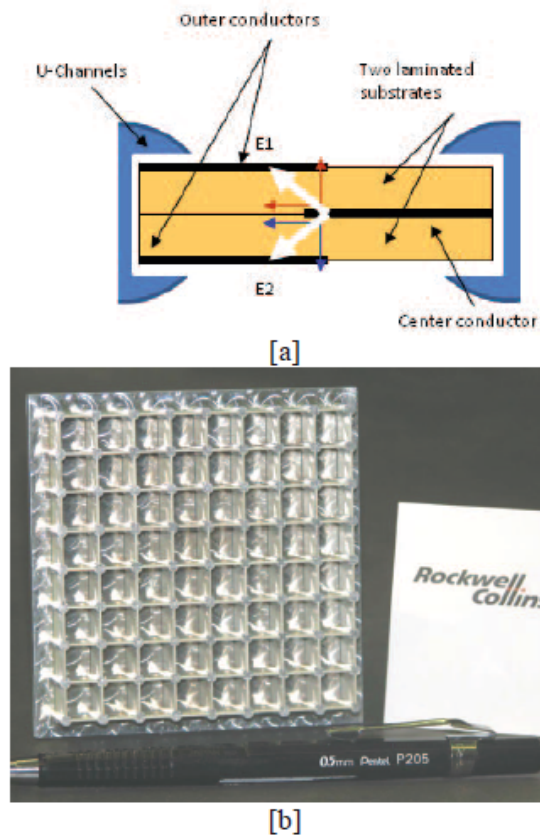


Figure 1.13. A 10:1 dual-polarized BAVA array [39]. (a) Unit cell of a single-polarized array; (b) 8×9 prototype of a dual-polarized configuration.

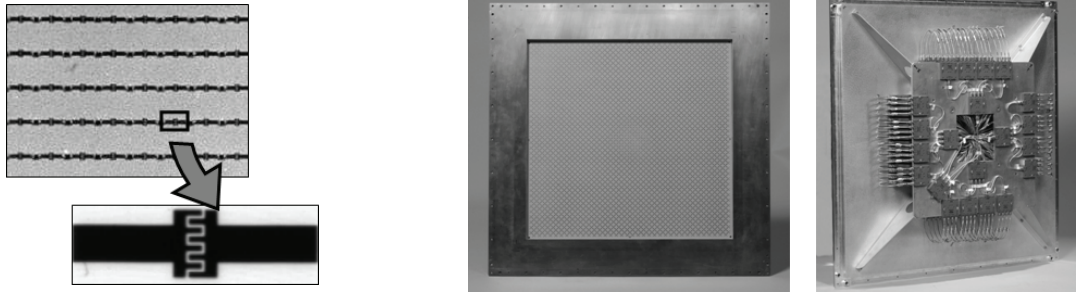


Figure 1.14. Current Sheet Antenna (CSA) arrays [40]. (a) Single-polarized CSA array highlighting the interdigitated capacitors to achieve high inter-element coupling; (b) Dual-polarized CSA array aperture and feed network designed for operation over 2-18 GHz.

Further advancements in unbalanced feeding including a recently designed modified BAVA array that offers a 10:1 bandwidth without the use of baluns or matching networks [39]. This array provides wide bandwidth and convenient assembly at the expense of VSWR levels (<2.75 broadside, <4.2 at 45°) and additional mechanical machining for the newly introduced metallic U-shaped channels highlighted within pictures of the array in Fig. 1.13. Although these low-profile, vertically-integrated arrays exhibit UWB performance, reported frequency scalability is difficult above K_u -band and the architectures are more complex than planar counterparts.

1.3.2 “Quasi-Planar” UWB Arrays

Due to their simple fabrication, ease of integration, low-profile, and good wide-scan performance, planar technologies have become an appealing area of research in ultrawideband arrays. However, although the radiating apertures of the arrays to be discussed in this section are entirely planar, three-dimensional devices such as baluns are required to overcome electrical limitations and retain a wide bandwidth, thus engendering the description of the arrays as “quasi-planar”.

Several notable arrays were developed to elucidate the demand for maximal bandwidth with a planar architecture. The current sheet antenna (CSA) array [40] is one

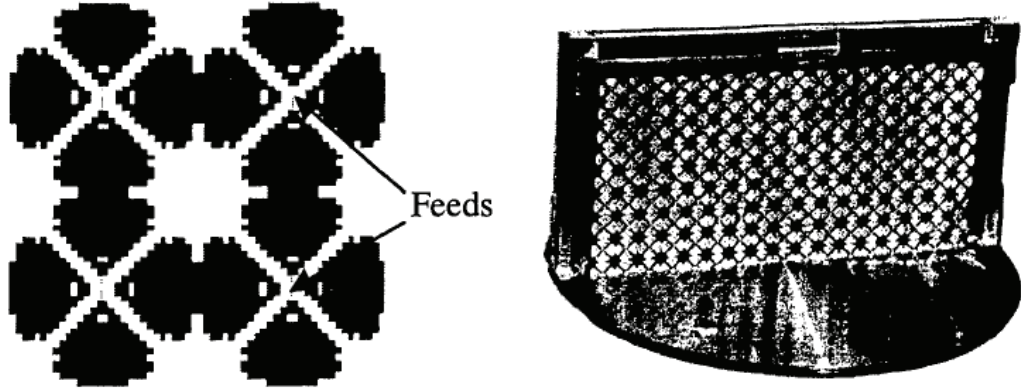


Figure 1.15. A Fragmented Aperture Array (FAA) optimized for operation over 1.25 to 10 GHz [42]. (a) A 2×2 FAA; (b) A $17 \times 8\frac{1}{2}$ FAA mounted on a brass plate for measurement.

such array that employs Wheelers' current sheet concept [41]. CSAs can achieve up to 9:1 bandwidth by using a dual-polarized (coincident phase center arrangement) tightly-capacitively coupled horizontal dipoles as shown in Fig. 1.14. These printed dipoles are a quarter-wavelength apart from the ground plane at midband, thus they counteract the inductive nature of the ground plane at lower frequencies, leading to increased bandwidth due to better matching at low frequencies. Other planar arrays such as the fragmented aperture array (FAA) [42] in Fig. 1.15 and long slot array [43, 44] in Fig. 1.16 use connected electric or "magnetic" elements that, in free space and infinite array configurations, could yield infinite bandwidth. The elements in these arrays are contiguously connected to form continuous current sheets that can be modeled as an array of center-fed periodically-spaced (typically $\lambda_{high}/2$) dipoles attached at the adjoining ends. To produce unidirectional radiation in such arrays, a ground plane is introduced that inevitably engenders resonances and, thus, lossy screens and R-cards [45, 46] are introduced between the array layer and the ground plane to suppress them. A planar interwoven spiral array has also demonstrated broadside 10:1 performance, but is limited to circular polarization only and scanning performance has yet to be addressed [47].

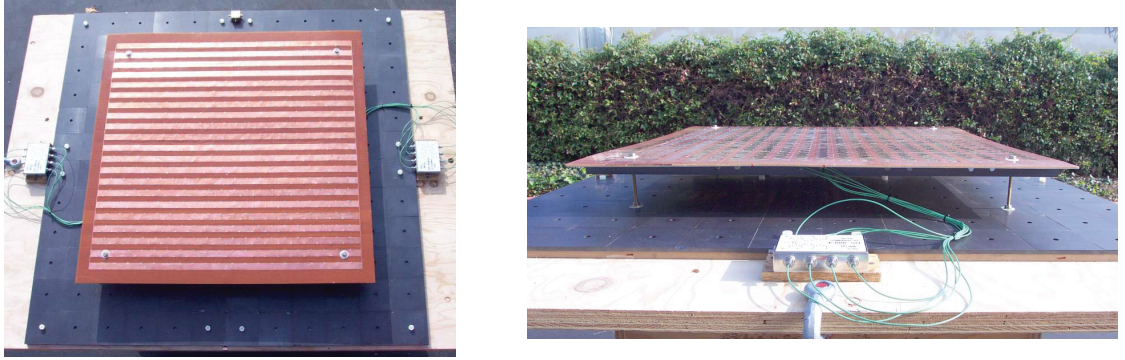


Figure 1.16. A single-polarized long slot array designed for operation over 0.2 to 2 GHz while backed by a ferrite loaded ground plane [40]. (a) Top view; (b) Side view of the array with a 5 cm air gap.

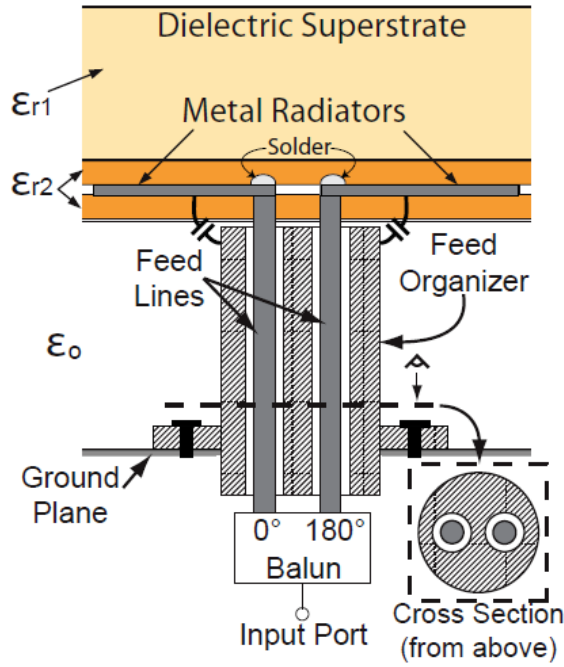


Figure 1.17. Cross-sectional view of a typical quasi-planar UWB array unit cell as depicted from [1].

As mentioned earlier, although each of the addressed array layers are fully printable and planar, each array requires external three-dimensional feeding support mechanisms to maintain their wideband performance. Such devices include wideband external baluns and “cable organizers” [48] that shield the vertical field lines to prevent scan-induced resonances [49] as shown in Fig. 1.17. The organizers complicate manufacturing as they must be mechanically and electrically connected to the ground plane and not realizable above K_u -band due to mechanical limitations, intrinsically inhibiting modularity and frequency scalability. Furthermore, a difficult soldering process is required to connect the vertical cables drawn through the organizers to the dipoles. All of the factors discussed within this section lead to truly non-planar architectures that ultimately impair low-cost manufacturing, radiation efficiency, and manufacturing of UWB arrays at mm-waves.

1.3.3 PUMA Arrays

To circumvent fabrication difficulties, lack of aperture modularity, and performance-limiting feeding methods that plague quasi-planar UWB arrays, the Planar Ultrawideband Modular Antenna (PUMA) array [2, 3] was developed. Unlike other dual-polarized UWB arrays, the PUMA array is manufactured with planar etched circuits and plated vias without the use of external baluns and cable organizers to allow for a simple, low-cost multilayer PCB fabrication process [1]. The array can be constructed modularly and retains a low-profile with a total depth of about $\lambda_{high}/2$. Additionally, a novel unbalanced feed-line scheme enables direct connection to standard RF interfaces and modular construction while mitigating common-modes within the operating band. The first class of PUMA arrays, PUMAv1 (shown in Fig. 1.18), demonstrated low VSWR and good scan performance with low cross-polarization in the D-plane out to $\theta = 45^\circ$ over a 3:1 bandwidth up to 21 GHz when fed directly from a 50Ω unbalanced interface [4]. Although exhibiting strong UWB performance with a low-

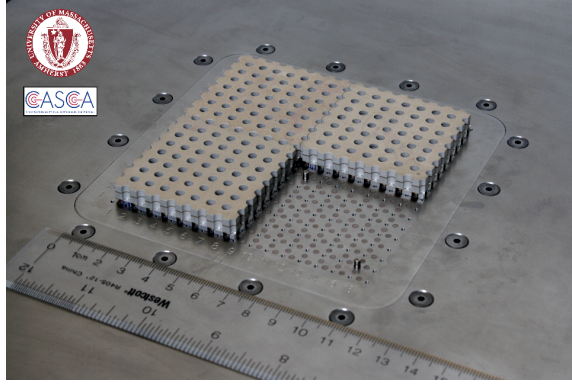


Figure 1.18. Three fabricated 8×8 PUMAv1 modules that operate over 7-21 GHz with a modular architecture while connected to a standard unbalanced 50Ω interface [1].

cost modular topology, a hard limit is inherently imposed upon the array bandwidth due to additional low-end loop modes spurring from the introduction of shorting vias within the topology [5].

Due to the constraints of the shorting vias on the array bandwidth, a second class of PUMA arrays, deemed the PUMAv2, was designed that explored utilizing an external planar matching network that was printed on the opposite side of the ground plane [5]. The principle behind the implementation of the matching network was to compensate for a mismatched array impedance over a wider bandwidth with an LC transmission line circuit, resembling the classic wideband impedance matching concept of a series open-circuit stub and impedance transformer [50, 51], to ultimately yield an improvement up to 5:1. Despite the bandwidth enhancement, several complications came about within the PUMAv2 unit cell as can be seen within Fig. 1.19. The required matching network lateral length was greater than $\lambda_{high}/2$, making it difficult to fit within a dual-polarized unit cell and while retaining aperture modularity. A thin gap was also used to synthesize the matching capacitance that limited its fabrication below 5 GHz. Additionally, the network was implemented using a microstrip

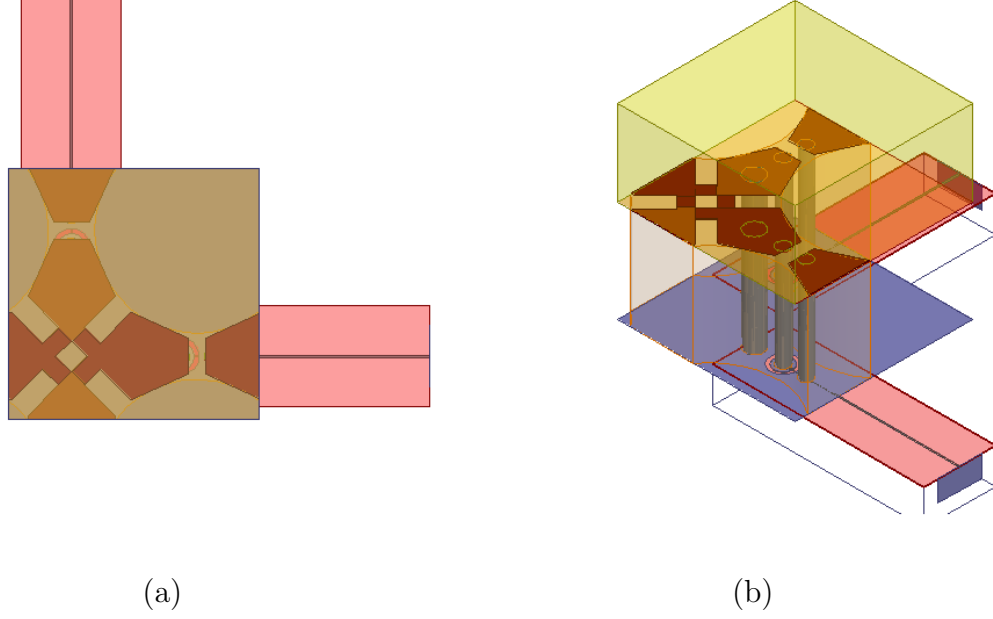


Figure 1.19. Full-wave model of the 1-5 GHz PUMAv2 unit cell with its microstrip backplane matching network designed within [1]. (a) Top view; (b) Isometric view.

design that does not provide necessary shielding from electromagnetic interference and maintain signal integrity with the rest of the RF front-end components.

1.4 Challenges

As mentioned in the previous section, PUMA arrays have laid the foundation for a low-cost, efficient, modular UWB arrays, but have not fully reached their goal of Vivaldi-like bandwidths and mm-wave scalability. To achieve this goal, several challenges need to be overcome:

(1) **Common-mode mitigation that does not inhibit low-end performance:**

PUMA arrays have demonstrated good UWB performance but are restricted from further bandwidth enhancements, without external (printed on the backplane) matching networks, due to low-end limiting loop-modes arising from the shorting vias that are necessary to suppress common-mode resonances. As a

result, innovations in the direction of common-mode suppression without the complementary induction of problematic loop-modes must be explored.

(2) **Achieving maximal bandwidth with minimal or no external circuitry:**

Although an external matching network was shown to enhance the bandwidth, practical implementation of such a circuit complicates the fabrication and increases fabrication uncertainty. The design of such a network in itself is also challenging since it must provide wide-bandwidth matching in real-estate that can fit within a unit cell.

(3) **Concurrently maintaining wide scan performance and a low array**

profile with minimal aperture oversampling: As PUMA arrays utilize thick PTFE substrates ($d \approx \lambda_{high}/2$) for mechanical support of feed lines and shorting vias, surface waves are supported at certain scan angles to engender scan blindnesses[52] within the scan volume. Ideally, scan blindnesses should be pushed above the grating lobe frequency to ensure minimal-to-no aperture oversampling, but the loading of dielectric materials is a critical design parameter in maintaining a strong wideband impedance match over wide angles [50, 53]. Thus, a conflicting relationship is engendered between an acceptable amount of aperture oversampling and the degree of wide-scan performance while retaining acceptable impedance levels. For instance, the high-frequency band-edge may reduce well-below the grating lobe frequency of the array if thick dielectric slabs are required for impedance match at wide angles and result in a vast oversampling of the aperture, requiring more elements (and thus more T/R modules) to fit in a given area. Accordingly, it becomes important to retain a low-profile ($\lambda_{high}/2$ or less) and eliminate scan blindnesses out to wide angles while still improving the bandwidth.

(4) **Produce mm-wave UWB array designs that meet multilayer PCB guidelines and tolerances :** Several issues arise from development of a low-cost UWB array using multilayer PCB fabrication at such high frequencies. As the frequency increases, all design parameters including unit cell and dipole dimensions reduce in size, making it difficult to have manufacturable designs. Specifically, using the current microwave PCB technologies, all the designs should adhere to the following rules:

- Standard minimum trace/space distance ($\approx 2\text{-}4$ mils)
- Via hole aspect ratio ($\approx 8\text{:}1\text{-}12\text{:}1$)
- Minimum soft-substrate PTFE thicknesses (≈ 10 mils) to avoid bending and shrinkage

As a point of reference to the difficulty, PUMAv1 arrays operating up to 21 GHz use the minimum standard thickness of a soft-substrate PTFE to synthesize higher inter-element coupling between orthogonal dipole arms. The PUMAv3 aims to scale to approximately 2.5 times higher in frequency while further increasing the bandwidth by 50% and not violating these guidelines.

1.5 Contributions

This work introduces the PUMAv3 class of arrays that dramatically improves the bandwidth and frequency scalability of PUMA arrays while still minimizing cost and design complexity. Theoretical insights into the control and effects of common-mode resonances in unbalanced-fed dual-polarized dipoles and several new technical innovations that will be discussed shortly are culminated into a full-wave infinite design that ultimately achieves a 50% bandwidth improvement (3:1 to 4.5:1) while operating at a frequency $2.25\times$ than the preceding PUMAv1 (21.3 GHz to 47.6 GHz). Altogether, the contributions of this work can be outlined as:

- (1) **Theoretical understanding of common-mode phenomena and shorting via effects in unbalanced-fed dual-polarized dipole arrays:** Holland in [1] theoretically studied the common-mode resonances in unbalanced-fed single-polarized dipole arrays and these results were used to justify the utilization of shorting vias in PUMA arrays. However, removal of the shorting vias in a dual-polarized PUMA unit cell will be shown to lead only to the onset of common-mode damped *resonances* within the band that do not lead to catastrophic impedance anomalies, but they do inhibit the radiation and gain around the frequency of this damped resonance. Ultimately, the necessity of shorting vias, or, in general, common-mode mitigation, within unbalanced-fed dual-polarized dipole arrays is fully justified and the inevitable bandwidth restrictions imposed from shorting vias are noted.

- (2) **Development of a non-bandwidth-limiting common-mode resonance mitigation method to alleviate the issues in (1):** A novel technical innovation is presented to mitigate common-mode resonances within the operating without imposing low-end bandwidth limitations. Much like the utilization of metallic ridges in waveguides used to reduce their fundamental cut-off frequency, the new common-mode mitigation approach now uses a single disconnected via with a capacitive plate within a unit cell to drop the common-mode frequency below the operational band (as opposed to previously pushing it above). Implementing common-mode mitigation in this fashion avoids the direct connection and shorting of the radiating arms to ground, avoiding the onset of low-end loop-modes. The invention of this common-mode mitigation technique is a major milestone for unbalanced-fed dipole arrays as it eliminates all common-mode detrimental effects within the operating band without deteriorating array performance.

- (3) **Improved scan performance and aperture oversampling through multiple superstrates:** A new superstrate loading scheme is introduced that consists of two unique dielectric layers with different permittivities and perforations that improves broadside and wide-angle impedance matching. As compared to previous PUMA arrays utilizing a single superstrate of uniform permittivity ($\epsilon_r = 1.96$) with thickness $d \approx \lambda_{high}/4$, the new approach enables the utilization of higher-permittivity dielectrics ($\epsilon_r = 4.5$) with thicknesses $d \leq \lambda_{high}/10$. The underlying principle is that the increase in dielectric permittivity enables a smaller dielectric thickness, which has a more profound effect on minimizing the volumetric effective permittivity and thus negating scan blindnesses within the scan volume.
- (4) **Design of the PUMAv3 array:** The PUMAv3 full-wave design is a low-cost mm-wave UWB array that improves the bandwidth of its predecessor, PUMAv1, by 50% (3:1 to 4.5:1). Like the preceding PUMA arrays, PUMAv3 is fed unbalanced, assembled modularly, and uses new via-based implementations to mitigate in-band common-mode resonances. PUMAv3 arrays aim to provide more bandwidth than preceding PUMA arrays without backplane networks as shown in Fig. 1.20(a), but, more importantly, seek to delve into the previously mentioned unexplored region of mm-wave UWB technology and offer more orders of magnitude of bandwidth over stack-patched arrays at similar cost and complexity as displayed in Fig. 1.20(b). The specific contributions of the PUMAv3 and the preceding PUMA array attributes are shown within Table 1.5, highlighting:
- 50% bandwidth improvement over PUMAv1
 - $2.25\times$ the frequency scalability of PUMAv1 and more than $9\times$ that of PUMAv2

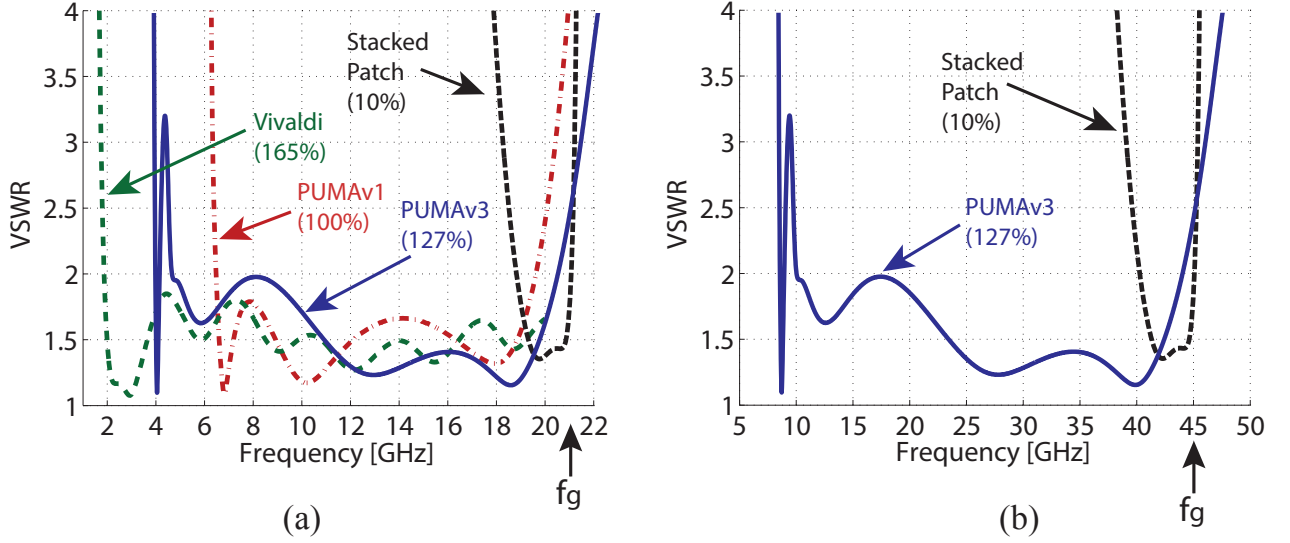


Figure 1.20. Comparison of fractional instantaneous bandwidths (FBW [%] = $\frac{f_{high} - f_{low}}{f_{mid}} \times 100$) of several established array technologies over different operating frequencies, including the stacked microstrip patch, Vivaldi, PUMAv1, and PUMAv3 arrays. (a) Available options at frequencies up to 21 GHz; (b) Available options at frequencies up to 45 GHz.

- >30% reduced profile
- Better f_{high}/f_g ratios for improved aperture oversampling

Additionally, PUMAv3 provides:

- Same-side/-layer bow-tie arms that are less prone to registration error and card bending during bonding. Replaces the overlapping opposite-side parallel-plate capacitors that are prone to these fabrication errors and require stringent spacings.

1.6 Thesis Overview

Chapter 2 provides theoretical insight to common-mode mitigation in unbalanced-fed, dual-polarized dipole arrays. Previously, Holland in [1] placed focus upon the study of common-modes disrupting performance in unbalanced-fed, single-polarized

	Bandwidth	f_{high}	Profile	f_{high}/f_g	Backplane Network?
PUMAv1	3:1	21 GHz	$0.5/\lambda_{high}$	94%	No
PUMAv2	5:1	5 GHz	$0.5/\lambda_{high}$	85%	Yes
PUMAv3	4.5:1	48 GHz	$0.38/\lambda_{high}$	97%	No

Table 1.1. Performance evolution of PUMA arrays.

dipole arrays. Physical explanations are given to expose the detrimental effects of common-mode issues on the electrical performance of the dual-polarized arrays. The conventional PUMA method of utilizing shorting vias to alleviate these common-mode problems is revisited from a dual-polarized perspective. Additionally, drawbacks imposed from implementing this shorting via approach are emphasized. Ultimately, justification for common-mode mitigation in unbalanced-fed, dual-polarized dipole arrays that doesn't inhibit bandwidth will become evident and act as the motivation for a new common-mode control technique to be discussed in Chapter 3.

Chapter 3 encompasses a description of the improved bandwidth, mm-wave scalable PUMAv3 array topology and its enabling components. First, the architecture of the array and its key differences from preceding PUMA arrays are highlighted. From here, the operating principles of the array are discussed in depth with heavy focus upon the advent and implementation of a novel capacitively-loaded via tactic. As compared to the previous common-mode control with shorting vias, the new method avoids bandwidth-limiting loop modes by avoiding direct electrical connection with the radiating arms and still mitigates common-mode phenomena altogether within the operating band. Control tactics for the new method are explored for various scenarios in conjunction with bandwidth enhancement techniques that exploit heightened inter-element coupling introduced from the capacitance synthesized from the approach. Also, an improved superstrate scheme consisting of separate dielectric layers with unique permittivities and perforations is investigated to offer improved

scan performance in comparison to that of the preceding PUMA arrays utilizing a uniform perforated superstrate.

Chapter 4 presents an infinite dual-polarized PUMAv3 array operating near 50 GHz meeting multilayer PCB fabrication guidelines followed by its numerical results from full-wave simulations. The most stringent parametric contingencies of the design that put a limit on additional scalability are highlighted and alternative solutions are offered. Impedance and radiation performance of the designed array are analyzed. Full-wave simulations suggest $VSWR < 2$ at broadside and $VSWR < 2.7$ out to $\theta = 45^\circ$ with -10 dB cross-polarization at 45° in the D-plane.

Chapter 5 provides the conclusion of the thesis and a discussion of future work.

CHAPTER 2

COMMON-MODE PHENOMENA IN UNBALANCED FED DUAL-POLARIZED UWB DIPOLE ARRAYS

2.1 Introduction

The PUMA array topology enables unbalanced feeding in dipole arrays through the mitigation of a broadside catastrophic resonance, referred to as the common-mode resonance, that would otherwise occur due to unequal magnitude currents on the feed lines [1–5]. At the frequency corresponding to the common-mode resonance, the feed lines themselves behave as monopoles protruding orthogonal to the ground plane and become the primary source of radiation, thus exhibiting devastating losses broadside to the array ground plane. As elaborated in [1], the common-mode resonance appears when the diagonal path length between shorted lines becomes half a wavelength, typically arising in the middle or upper portion of the frequency band. To mitigate the resonance, PUMA topologies place shorting vias at dipole arms to effectively push the common-mode resonance above the usable frequency band. Previous PUMA papers analyzed the behavior of the common-mode resonance before and after the insertion of the shorting vias, but only do so in depth for single-polarization scenarios. For clarity, a full analysis of common-mode effects in dual-polarized configurations will be provided and the need for their mitigation will be justified.

2.2 Direct Unbalanced Feeding

In a dual-polarization configuration, the grounded feed-line of the orthogonal dipole inherently act likes a shorting via suppressing common-mode resonances along

the long diagonal path. Without shorting vias, the resonant dimensions of the square dual-polarized unit cell intrinsically reduce to D_x and D_y as shown in Fig. 2.1, suggesting the common-mode frequency, f_{cm} , would ideally occur at the grating lobe frequency with a half-wavelength spacing and that dual-polarization configurations do not need additional shorting via support. However, since PUMA arrays are manufactured with dielectric materials, the effective length of the common-mode resonant dimension is increased by the effective relative permittivity of the substrate. As a result, the common-mode frequency, f_{cm} , is given by [1]

$$f_{cm} \approx \frac{c_o}{2\sqrt{\epsilon_{r,eff}}D} \quad (2.1)$$

where $D = D_x = D_y$ for the square unit cell. As PUMA arrays use dielectrics with low values of $\epsilon_{r,eff}$, the common-mode frequency should theoretically appear at the high-end of the band.

A plot of the active return loss magnitude, Γ_{11}^a in Fig. 2.2 reveals the presence of a small impedance variation at f_{cm} . At first glance, it may appear that unbalanced-fed dual-polarized dipole arrays are immune to common-mode effects, however, complete analysis would require a closer look at observing the effects on the orthogonal port isolation and co- and cross-polarized radiated power per unit cell. Upon charting the magnitude of the active orthogonal port transmission coefficient in Fig. 2.3, the port coupling is seen to deteriorate highly at f_{cm} due to the orthogonally-polarized port. This is expected since the orthogonal port grounded via acts a shorting via, drawing large currents down to the ground at f_{cm} , effectively creating a conduction path that degrades orthogonal port isolation. The balanced feed approach uses a delta-gap source thus minimal coupling occurs. The degradation in port isolation combined with the respective losses from the return-loss ultimately result in problematic radiated power levels as displayed in Fig. 2.4. At f_{cm} , a 6 dB drop in the co-polarized power occurs and the cross-polarized power levels rise maximally to inhibit the array's

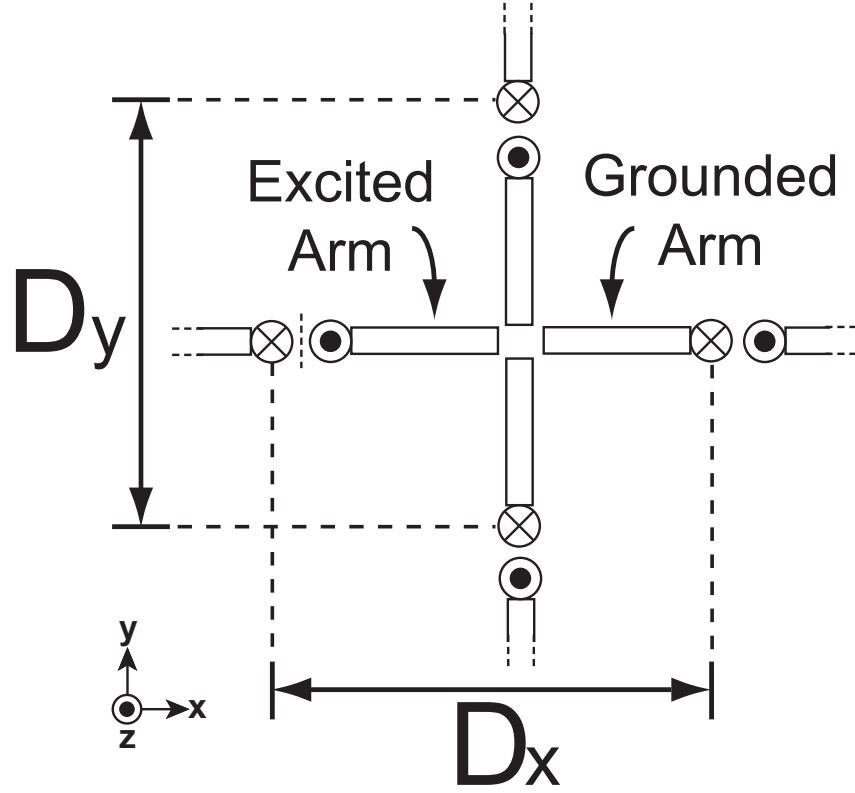


Figure 2.1. Top view of an unbalanced-fed dual-polarized dipole array. The common-mode resonant dimensions intrinsically reduced to its unit cell dimensions, D_x and D_y .

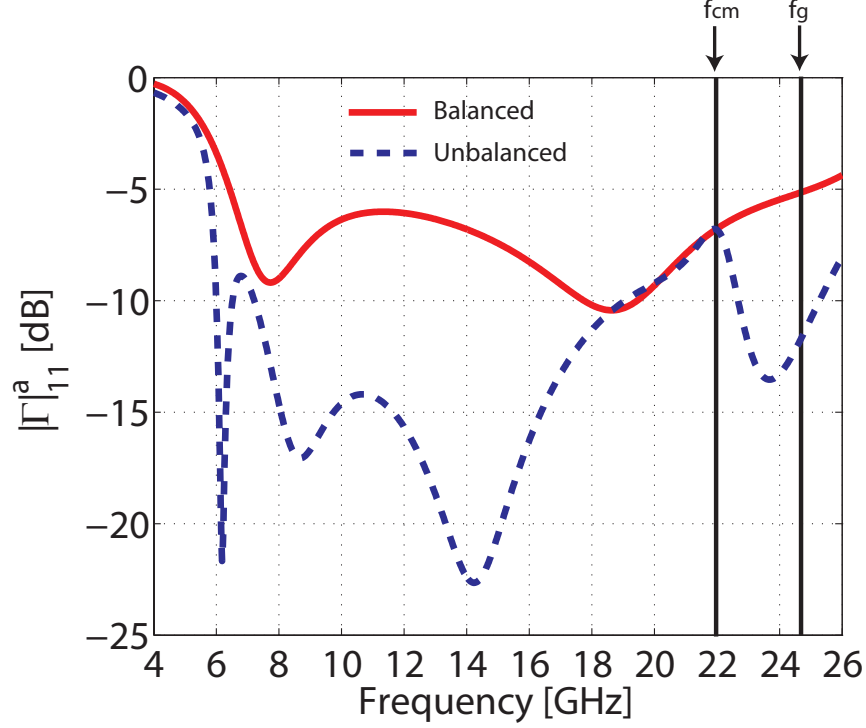


Figure 2.2. Magnitude of the self active reflection coefficient, Γ_{11}^a , of an unbalanced-fed dual-polarized dipole array compared to its balanced-fed equivalent.

operation. Additionally, the skirt surrounding f_{cm} further hinders performance by about 10% beneath its onset location (from 20 to 22 GHz for this instance). As a result, common-mode effects in dual-polarized configurations still decimate the in-band performance and split the operating band to approximately 80% of f_g , yielding a dramatically oversampled aperture. For example, if an array was operating at $0.8f_g$ and was required to occupy an area of $24\lambda \times 24\lambda$ at the highest frequency with a half-wavelength spacing, the array would require 3600 elements and T/R modules. If the high frequency of the array was instead operating at f_g , 2304 elements would be required - *a 36% reduction of elements and T/R modules to fill the given area*. Furthermore, as the common-mode effects in dual-polarized assemblies do not exhibit the purely resonant behavior as their single-polarized counterparts do, they will be referred to as ‘common-mode phenomena’.

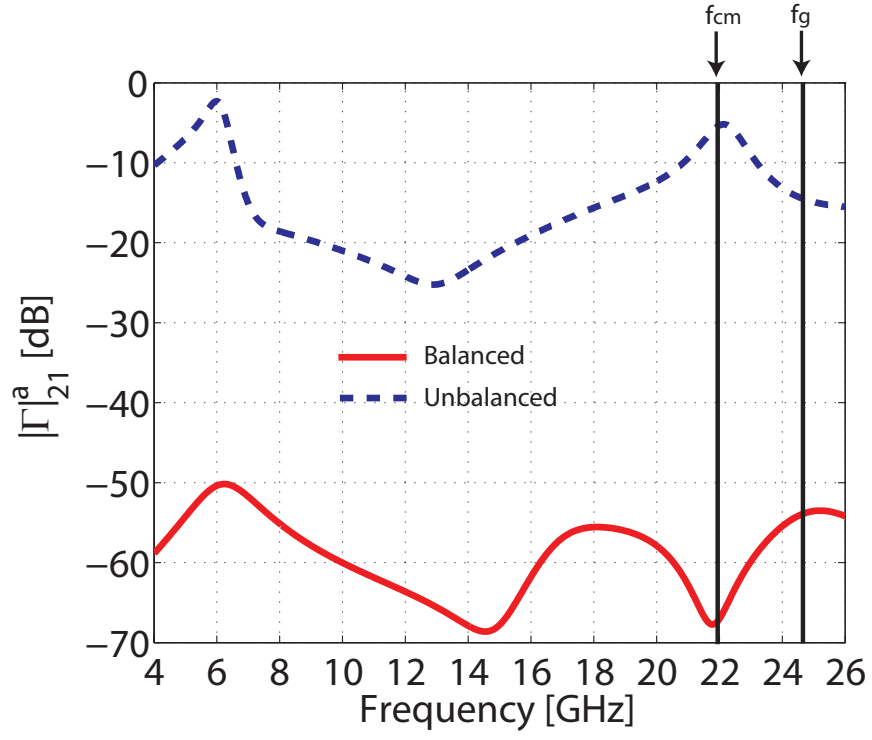


Figure 2.3. Magnitude of the active port transmission coefficient, Γ_{21}^a , of an unbalanced-fed dual-polarized dipole array compared to its balanced-fed equivalent.

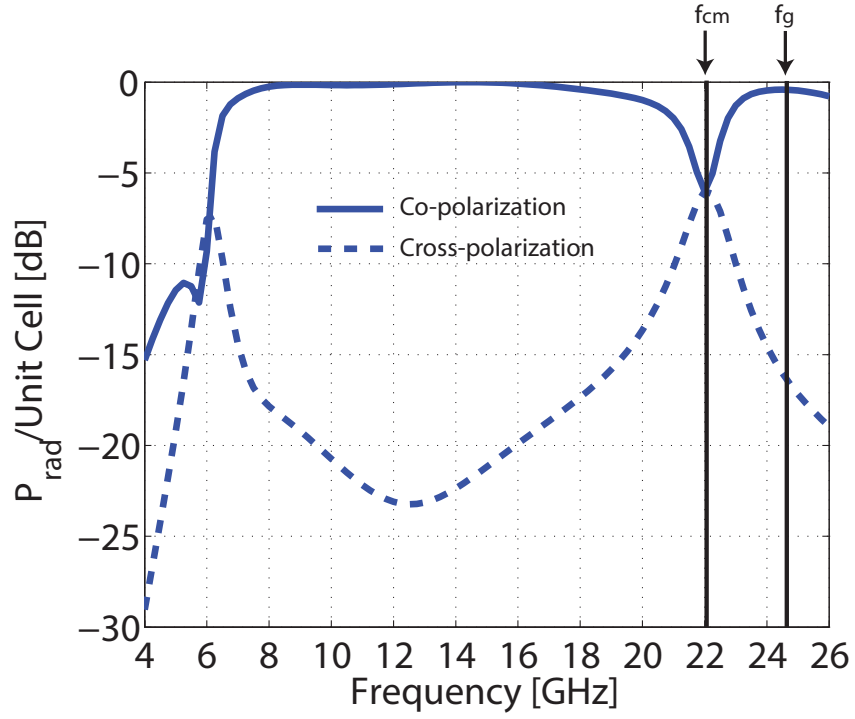


Figure 2.4. Co- and cross-polarization (Ludwigs 3rd definition [59]) radiated power vs. frequency of an unbalanced-fed dual-polarized dipole array.

2.3 Unbalanced Feeding with Shorting Vias (PUMAv1 and v2)

Shorting vias are also employed in dual-polarized configurations to push common-mode phenomena out of the operating band. The design paradigm follows closely to that of single-polarized arrays, except now the shorting via of the orthogonally-polarized arm is utilized to reduce the cross-polarized common-mode length. A top view of an unbalanced-fed dual-polarized with shorting vias is displayed in Fig. 2.5 and highlights the updated reduced resonant lengths in the co- and cross-polarized directions. Assuming that the vias are displaced equally in both directions, the common-mode frequency can be predicted through [1]

$$f_{cm} \approx \frac{c_o}{2\sqrt{\epsilon_{r,eff}}(D - d)} \quad (2.2)$$

where $D = D_x = D_y$ for the square unit cell and d is the displacement distance of the via. Proper selection of d is used to push the common-mode frequency above the frequency band. The active reflection and port transmission coefficients are plotted in Fig. 2.6 and Fig. 2.7, respectively. Ultimately, the co-/cx-polarized levels exhibit good performance throughout the operating band as shown in Fig. 2.8 due to the implementation of shorting vias.

Although shorting vias are shown here to solve the issue of in-band common-mode phenomena, they still pose a major limitation upon inhibiting the low-band edge of the array due to problematic loop modes discussed in [1, 5]. The introduction of shorting vias dramatically changes the low-end behavior of the array by forming a circulating loop between the shorted feed line and the shorting via itself, where the size of the loop dictates the lowest frequency. Ideally, this loop should be designed to be as large as possible to attain the lowest possible low-end for more bandwidth, but, consequently, this translates to decreasing the displacement distance of the via, d , which decreases common-mode frequency. The active reflection and port transmission

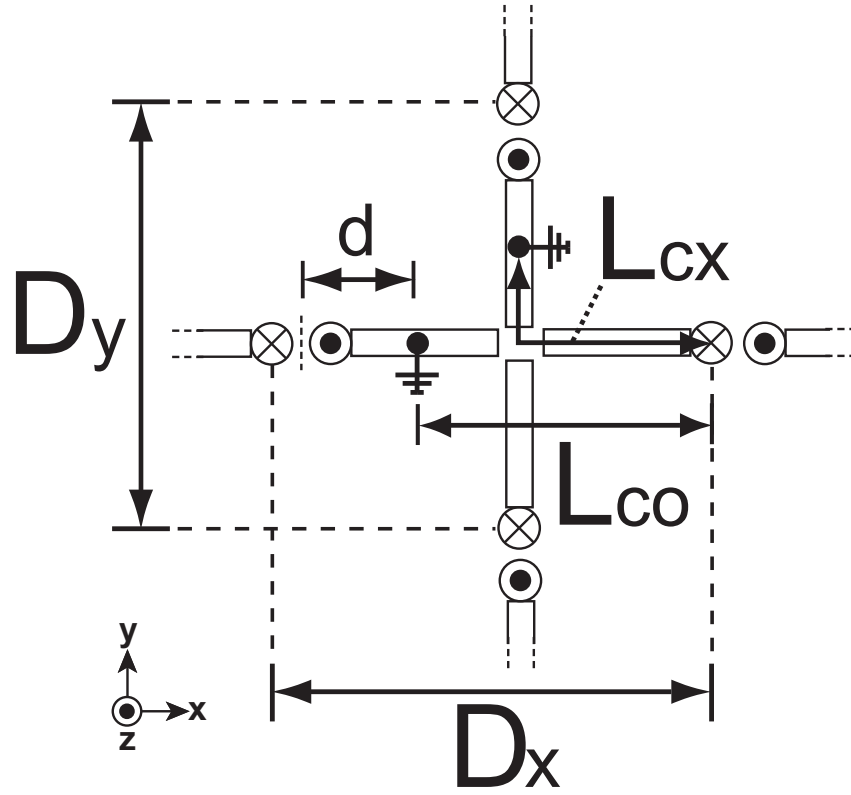


Figure 2.5. Top view of an unbalanced-fed dual-polarized dipole array with shorting vias. The common-mode resonant dimensions are reduced to its unit cell dimensions, L_{co} and L_{cx} .

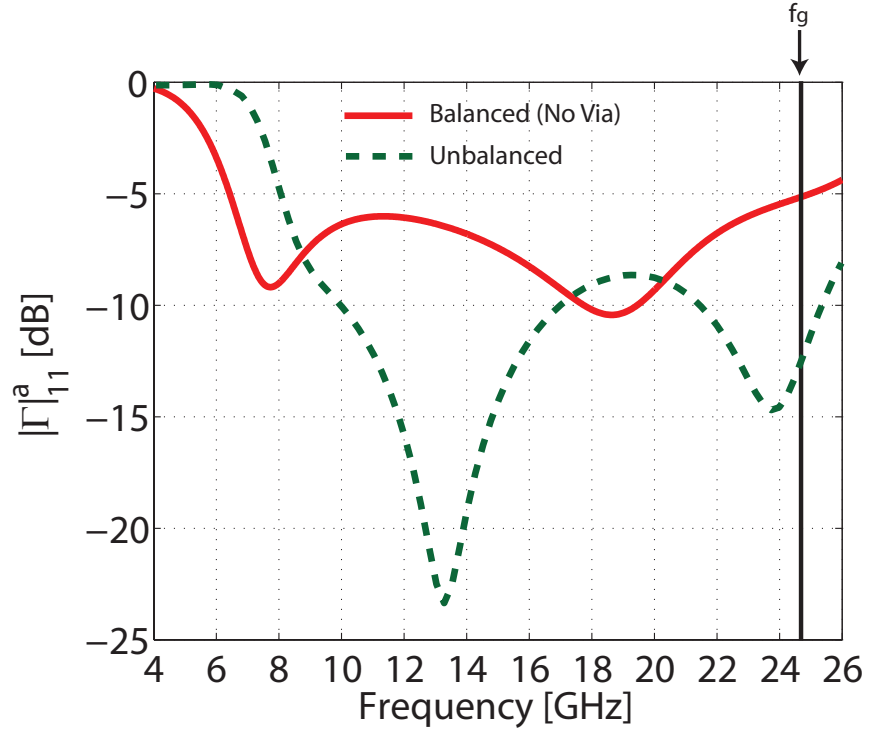


Figure 2.6. Magnitude of the self active reflection coefficient, Γ_{11}^a , of an unbalanced-fed dual-polarized dipole array with shorting vias compared to its balanced-fed equivalent.

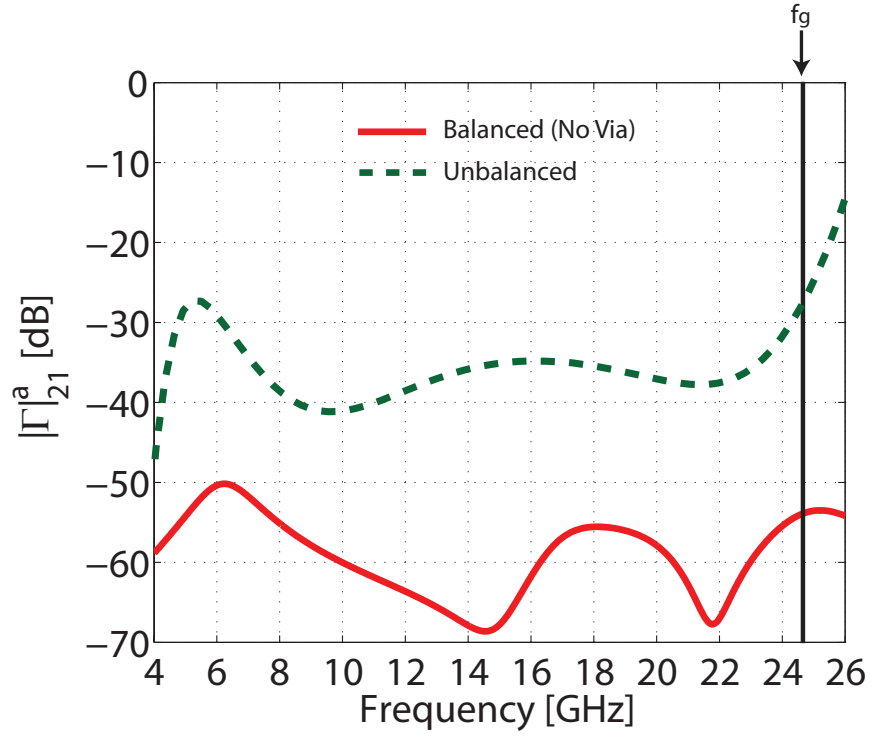


Figure 2.7. Magnitude of the active port transmission coefficient, Γ_{21}^a , of an unbalanced-fed dual-polarized dipole array with shorting vias compared to its balanced-fed equivalent.

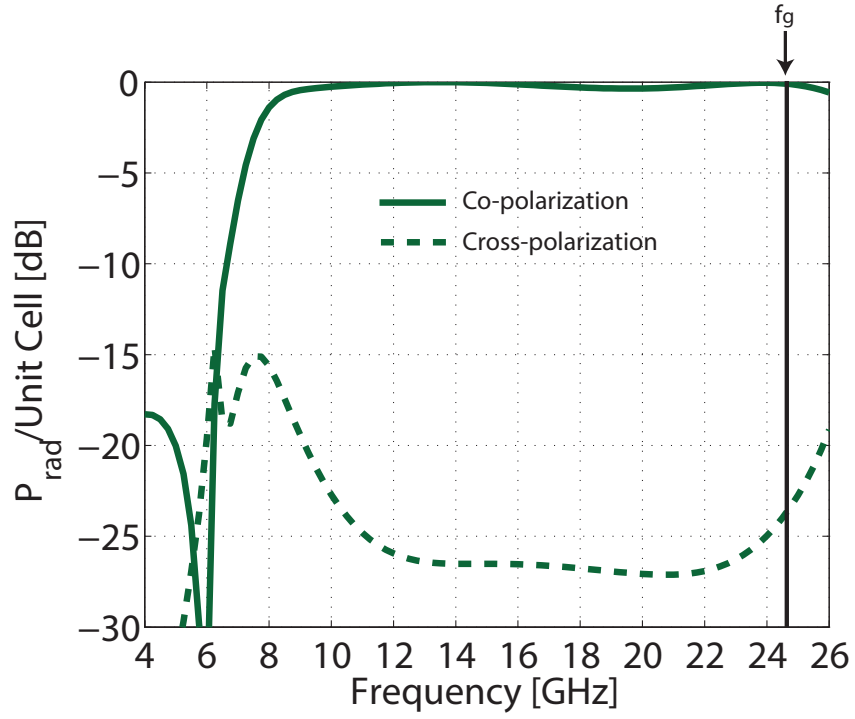


Figure 2.8. Co- and cross-polarization (Ludwigs 3rd definition [59]) radiated power vs. frequency of an unbalanced-fed dual-polarized dipole array with shorting vias.

coefficients of an unbalanced-fed dual-polarized dipole array for cases where shorting vias are present and absent is plotted in Fig. 2.9(a), emphasizing the reduced low-band edge of the case with vias and the poor common-mode mitigation of the case without vias. Further comparisons are shown in Fig. 2.9(b) with the co- over cross-polarized power levels. As a result, an inevitable and necessary trade-off between bandwidth and high-end common-mode mitigation is present with the shorting via approach.

2.4 Conclusion

Unlike single-polarized unbalanced fed UWB dipole arrays that exhibit detrimental resonant return-loss behavior at their common-mode frequency mid-band, dual-polarized configurations display comparatively minor impedance variations at their predicted common-mode frequency at the high-band. However, the effects of common-mode phenomena on dual-polarized arrays cannot be analyzed from observation of the active input impedance alone. If the entire unit cell S-matrix is not properly considered, the operational bandwidth of the array will be misleading due to not considering the power dissipated into the orthogonal port. The effects of common-mode phenomena on dual-polarized PUMA arrays are clearly evident from considering the co-/cross-polarized radiated powers at the predicted common-mode frequency, indicating unacceptable performance due to a 6 dB drop in co-polarized power and a vast increase in cross-polarized power. The gain bandwidth is notched at the high-end due to the common-mode phenomenon and reduces f_{high} to 80% of f_g , ultimately resulting in an approximate 40% bandwidth reduction and a severe oversampling of the aperture. Despite fixing this issue with shorting vias, bandwidth becomes reduced at the low-end as an inevitable trade-off with the implementation and inhibits maximum bandwidth performance.

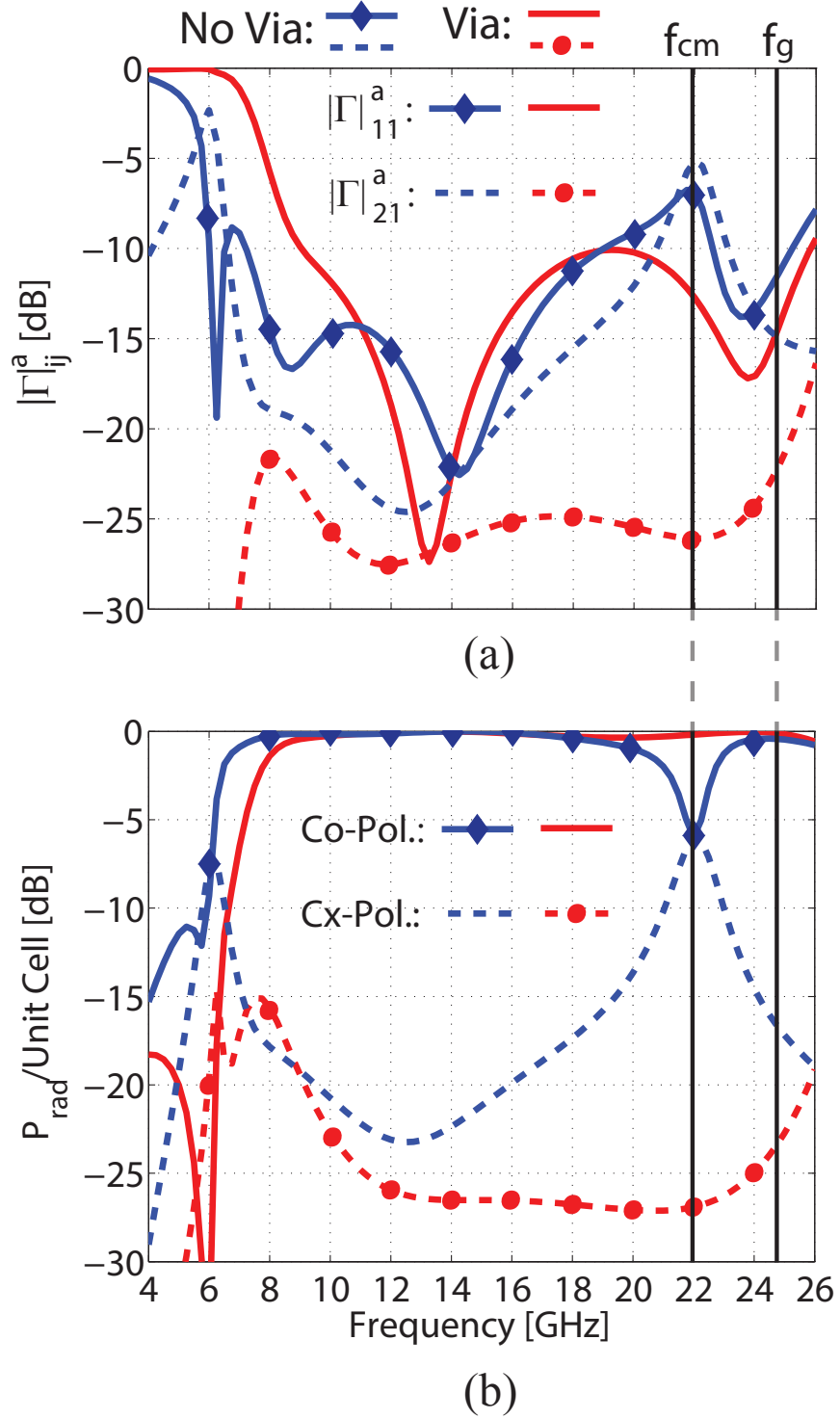


Figure 2.9. Common-mode manifestation in infinite dual-polarized unbalanced fed dipole arrays with (PUMAv1 and v2) and without (direct unbalanced feeding) shorting vias. (a) Broadside active reflection and orthogonal port transmission (isolation) coefficients; (b) Broadside co- and cross-polarized (Ludwig's 3rd definition [59]) radiated power.

CHAPTER 3

PUMA V3 ARRAYS

3.1 Introduction

This section introduces the topology of the new class of PUMA arrays, termed PUMAv3, and its operational theory. As stated in the previous chapter, preceding PUMA arrays enabled unbalanced feeding through the mitigation of broadside catastrophic common-mode resonances with shorting vias, but, in doing so, limited their low-end bandwidth with the induction of loop modes [1–5]. The PUMAv3 directly addresses this issue by employing a new technical innovation, capacitively-loaded vias, that simultaneously eliminates in-band common-mode resonances and improves low-end bandwidth performance. Enabling theory and physical insight will be provided through waveguide approximations and parametric sweeps. Additionally, scan performance is addressed and improved with the introduction of a two-layer superstrate consisting of unique permittivities and perforations.

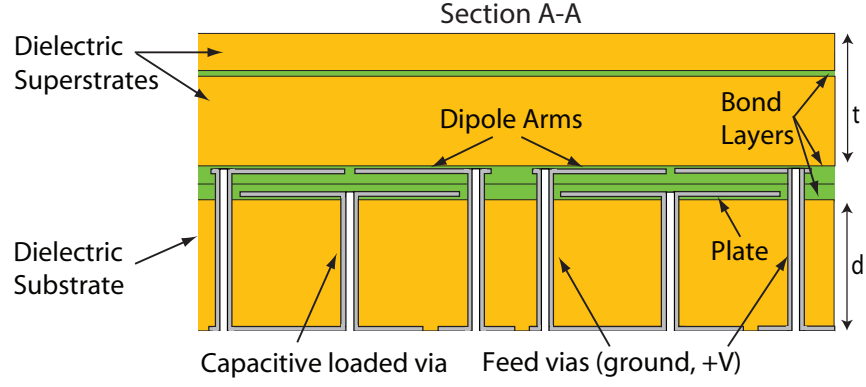
3.2 Topology

The general structure of the PUMAv3 class of arrays was based heavily upon the premise of construction at mm-waves. Due to the reduction in dimension of all critical design parameters with frequency, compliance with standard short-substrate PCB fabrication rules at mm-wave frequencies become a real challenge. Because of the strict fabrication contingencies, the PUMAv3 unit cell is radically different than its predecessors while retaining modularity and direct unbalanced feeding (no

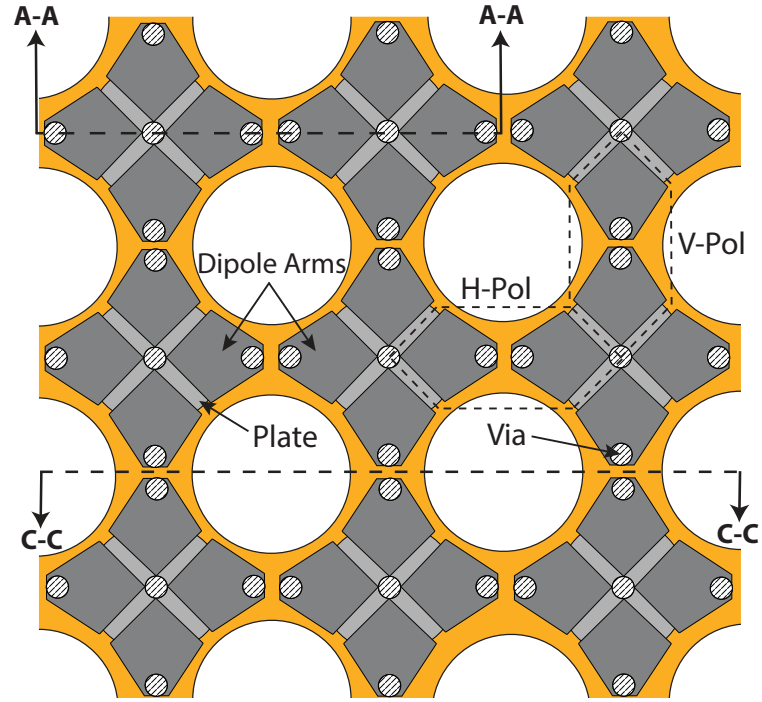
external baluns or matching networks). The lattice configuration itself remains dual-offset dual-polarized, and only dual-polarization topologies will be discussed (although single-polarization are also possible).

In contrast to preceding PUMA arrays, the PUMAv3 dipole arms are diamond-shaped, occupy a much larger area, and reside on the same side of a layer as shown in Fig. 3.1(b). Printing the dipoles on the same layer eliminates manufacturing variations due to registration and card bending during bonding. Instead, a circular metallic plate is registered on the opposite side of the same material with its origin centered between the intersection of the radiator tips. This plate is subject to registration variations, but its precise location and size are not as critical design parameters. Additionally, as shown in Fig. 3.1(a), bond layers could be used as the separation layer between this metallic plate and the dipole arms, where the dipole arms could be comprised of copper foil, for a cheaper and more reliable fabrication process. The capacitive coupling between the cross-polarized dipole arms combined with that between the plate and the dipole layer itself synthesizes a high amount of inter-element coupling, enabling the use of thicker bond layers or soft-substrate layers. The high coupling becomes especially important when considering fabrication at mm-wave frequencies as the thicker layers still remain relatively large after scaling to meet fabrication guidelines.

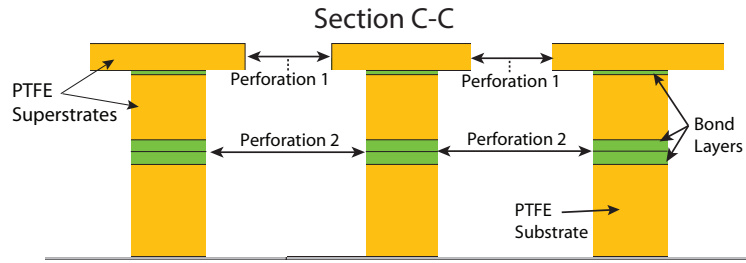
Two PTFE superstrates are used as cover layers, as seen in Fig. 3.1(a) and Fig. 3.1(c), to further improve matching and provide wide-angle impedance matching (WAIM) [53]. Compared to preceding PUMA arrays that use a single superstrate layer, the use of two layers was found to allow the permittivities to be much higher ($\epsilon_r \approx 4.5$) without suffering from surface wave degradation and to reduce the total superstrate from $\lambda_{high}/4$ to $\lambda_{high}/6$, where λ_{high} is the wavelength of the highest operating frequency. The multiple superstrate layers improve impedance performance by providing a smoother, more continuous impedance match to free space with addi-



(a)



(b)



(c)

Figure 3.1. PUMAv3 topological viewpoints (not to scale). (a) Cross-sectional view of a $1 \times 2 \times 2$ PUMAv3 array displaying via connections and dielectric layers stack-up; (b) Top view of a $3 \times 3 \times 2$ array's metallized components and perforated dielectric layers; (c) Cross-sectional view of a $3 \times 3 \times 2$ PUMAv3 between feed lines.

tional degrees of freedom. A bottom dielectric layer of low permittivity ($1 \leq \epsilon_r \leq 2.2$) that supports plated vias with thickness $d \approx \lambda_{high}/4$ is used for mechanical support of the feed lines and grounded connections. As a minimal cost post-plating procedure, perforations are also drilled throughout the entire stackup as visible in Fig. 3.1(a) to help alleviate scan blindnesses at wide angles like in the previous PUMA arrays. Despite their extremely thin thickness, prepreg bonding layers will also be incorporated into the analytical and numerical model as their aggregate height can incorporate almost 5% of the total profile of the array at mm-waves, which tends to about $0.4\lambda_{high}$.

PUMA arrays are well-known for their unique usage of shorting vias to enable unbalanced feed line connections without an external balun by electrically connecting the dipole arm(s) to ground with vias [1–5]. The PUMAv3 also uses vias, but, instead of shorting the dipole arm(s), the vias remain electrically disconnected and capacitively coupled to the dipole arms through the use of the metallic plate shown within Fig. 3.1(a) and Fig. 3.1(b). This critical variation, in conjunction with the augmented inter-element coupling and dielectric loading, enhances the performance of PUMA arrays and enables scalability to mm-wave frequencies through simultaneously mitigating in-band common-mode resonances and low band-edge loop modes induced from directly connected shorting vias [1, 5]. Furthermore, the entire array retains its modular assembly, unbalanced feeding, and eligibility for single microwave multilayer PCB fabrication.

3.3 Theory

Like the preceding PUMA arrays, PUMAv3 attains its wideband performance match by utilizing a modified version of Munk’s implementation of the current sheet principle: tightly-coupled dipoles over a ground plane with dielectric covers for wide-angle impedance matching [40, 54]. As compared to Munk’s array which uses coincident-

phase dual-polarized horizontal dipoles with strong co-polarized capacitive coupling [40], PUMA arrays are comprised of a dual-offset, dual-polarized arrangement to enable modularity and attains their capacitance through cross-polarized coupling [1–5]. Additionally, PUMA arrays serve as convenient feeding solutions by employing shorting vias in a unique fashion [1–5], but in doing so the impedance behavior of the arrays is drastically altered and the maximum potential of the array is ultimately limited. This section will discuss the enabling theory and design strategies to overcome limiting factors and further extend the bandwidth and frequency scalability. The interested reader is encouraged to read previous PUMA papers [1–5] if a stronger background is desired.

3.3.1 The Waveguide Model for Common Modes

Following the insights gained in the PUMAv1 common-mode mitigation approach, where the vias were used in a similar fashion as vias or ridges in a waveguide, this section will explore the possibility of using a waveguide model to justify and study the PUMAv3 common-mode mitigation strategy. It becomes useful to first observe the link in physical behavior between control of critical modes in waveguides and unbalanced-fed dipole arrays. For the investigation, propagation constants of the fundamental TE_{10} mode of a rectangular waveguide with equivalent dimensions of various unbalanced-fed dual-polarized dipole arrays are calculated through full-wave analysis and compared to the location of the common-mode frequencies for the arrays with and without via configurations.

The structural similarities and electric field distributions of the cut-off and common-mode modes for the waveguide and an unbalanced-fed dipole array are shown in the left side of Fig. 3.2 through a cross-sectional point of view. The shorted feed vias of the dipoles mimic the metallic walls in the lateral dimension of the waveguide, and, whereas the excited feed via represents the probe fed excitation of the dominant

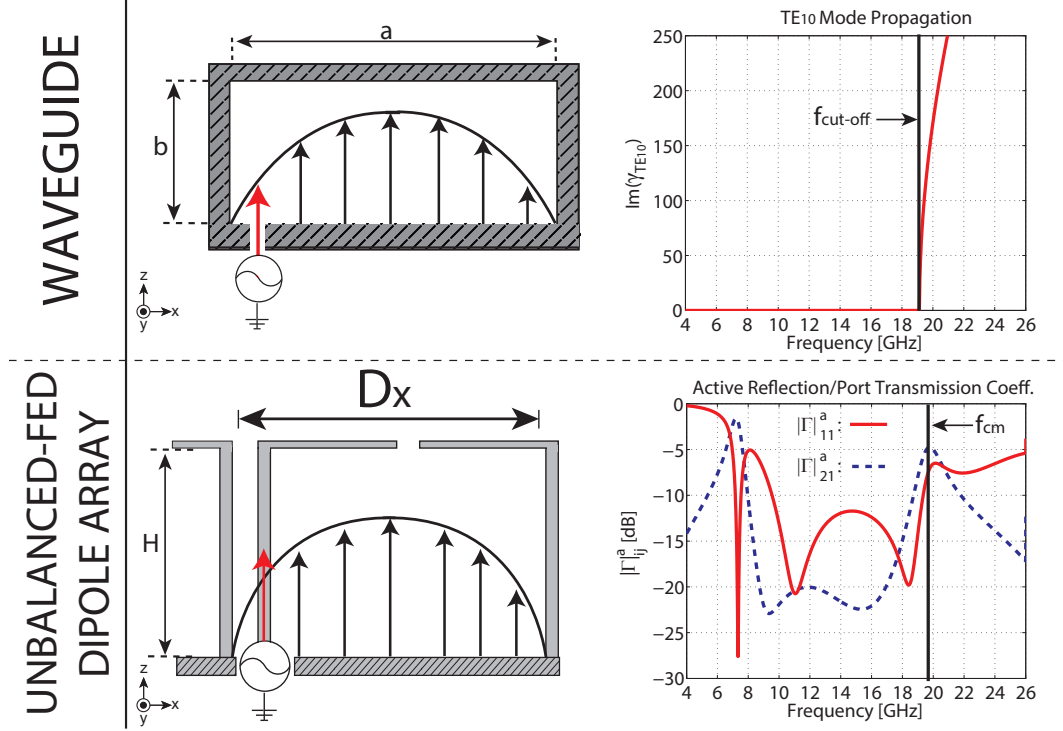


Figure 3.2. Waveguide vs. unbalanced-fed dual-polarized dipole array structural and cut-off/common-mode frequency comparisons for when $a = D_x \approx 6\text{mm}$, $b = H \approx 3\text{mm}$, and both topologies are filled with a homogenous dielectric material of $\epsilon_r = 1.96$.

TE_{10} mode, the ground plane and dipoles themselves resemble the upper and bottom walls. For this example, the dimensions of both the waveguide and unbalanced-fed dual-polarized dipole array are equivalent in the x-/z-direction ($a = D_x \approx 6\text{mm}$ and $b = H \approx 3\text{mm}$) and both are filled with a homogenous dielectric material of $\epsilon_r = 1.96$. The right side of Fig. 3.2 charts the imaginary component of the dominant mode propagation constant, γ_{10} , versus frequency to observe the dominant cut-off frequency, $f_{\text{cut-off}}$, and the active reflection/port transmission coefficients versus frequency to highlight the common-mode frequency, f_{cm} . In both cases, $f_{\text{cut-off}}$ and f_{cm} obstruct the operating bandwidth and appear within 2.5% difference of one another in frequency to suggest the phenomena are physically similar.

As discussed throughout Chapter 2, shorting vias in PUMAv1 are used to push to f_{cm} above the operating band. Similarly in the rectangular waveguide, inserting a

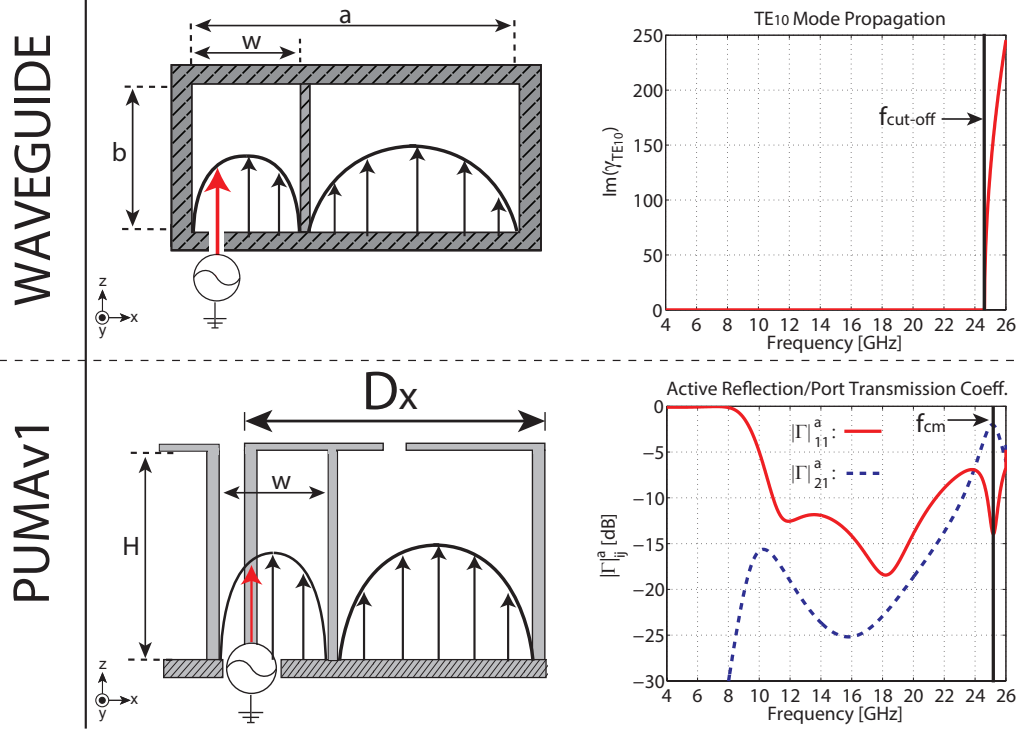


Figure 3.3. Waveguide vs. PUMAv1 (unbalanced-fed dual-polarized dipole array) structural and cut-off/common-mode frequency comparisons with shorting pins/vias for when $a = D_x \approx 6\text{mm}$, $b = H \approx 3\text{mm}$, $w = 1\text{mm}$, and both topologies are filled with a homogenous dielectric material of $\epsilon_r = 1.96$.

shorting ridge down the body of the waveguide with the same separation distance, w , as that of a PUMAv1 topology also pushes its cut-off frequency upwards to within 2.5% of f_{cm} and further concretizes the physical similarities between one another as displayed in the right side of Fig. 3.3. From a physical perspective, the modal solutions are seen to reduce by enforcing another PEC boundary condition and truncating the resonant dimension of the standing waves. However, this approach was shown in [1, 5] to deteriorate the low-end band-edge of the array due to low-end loop modes and limit further bandwidth enhancements.

A known method to shift the cut-off frequency to lower frequencies and, consequently, increase the bandwidth of waveguides, is to insert metallic ridges on the bottom, top, or both top and bottom sides within the waveguide [55, 56]. This ridged waveguide arrangement utilizes the dimensions and placement of the inward metallic

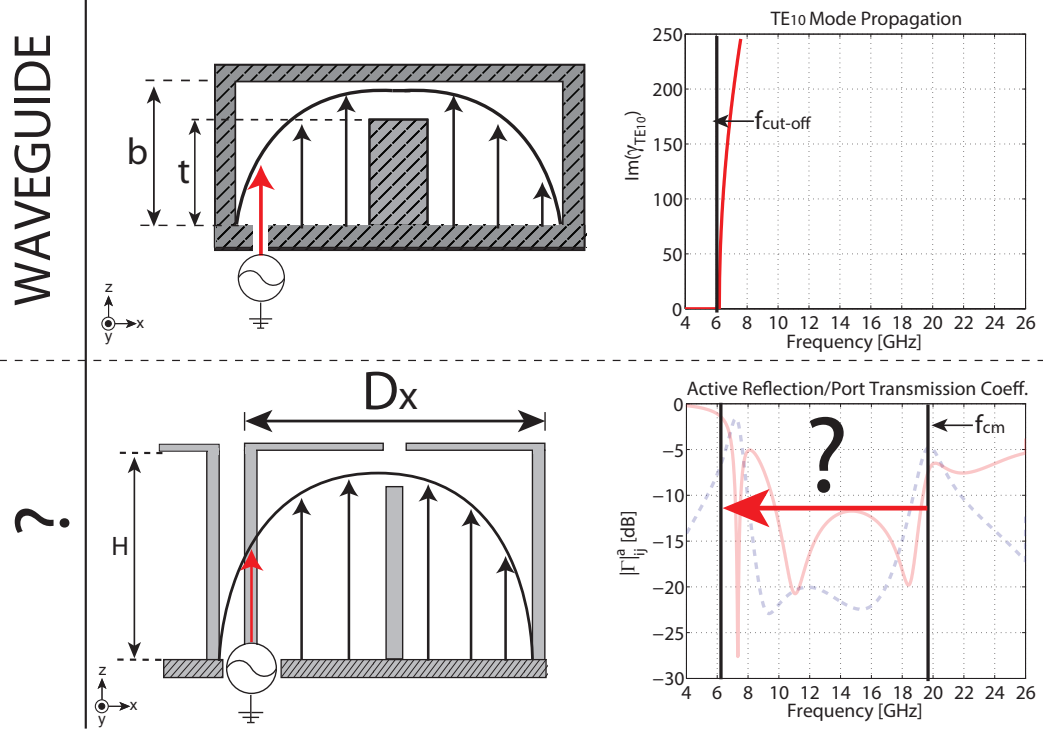


Figure 3.4. Ridged waveguide vs. a new idea of unbalanced-fed dual-polarized dipole array with metallic disconnected vias with unknown properties. Ideally, f_{cm} will be shifted beneath the low-end operating edge of the band near $f_{\text{cut-off}}$ of the ridged waveguide without limiting the low band-edge by inducing loop modes.

ridges to control the location of $f_{\text{cut-off}}$, with one such example shown within Fig. 3.4. An attractive trait that the ridged waveguide embodies is that no direct electrical connection or grounding is made between broad-walls. From the perspective of an unbalanced-fed dipole array, this suggests that no loop modes will be able to exist as no additional shorting of the dipole arms would occur and, thus, no bandwidth limitations at the low-end would be present. The question would therein be the following: could the unbalanced-fed dipole array utilize a ridged waveguide approach and push f_{cm} below the operating band without inducing low-end loop modes?

3.3.2 Ridged Waveguide Analysis

Before attempting to implement a ridged waveguide-like method to control the common-mode frequency, an analysis of the controlling components of the ridged

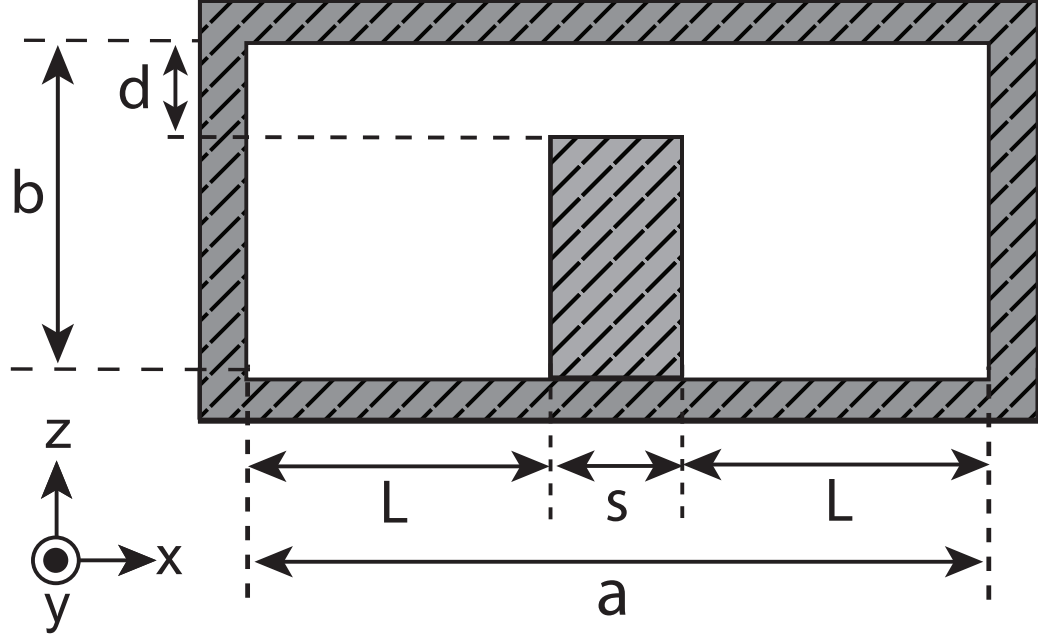


Figure 3.5. A standard ridged waveguide with important labeled dimensions.

waveguide cut-off frequency will be conducted. A standard ridged waveguide is shown in Fig. 3.5 with its characteristic equation given in [55] as

$$\cot k_x L - \frac{b}{d} \tan k_x s/2 - B/Y_{01} = 0 \quad (3.1)$$

where k_x is the propagation in the \hat{x} direction at cut-off, B/Y_{01} is the normalized discontinuity susceptance due to the change in height of the ridge, and b , d , s , and L are the waveguide dimensions labeled within the figure. The main goal will be to observe the effects of these waveguide parameters, for a given a and b , on the propagation constant k_x and its corresponding cut-off frequency $f_{cut-off}$. From here, the knowledge gained to successfully control the cut-off frequency for a waveguide with dimensions a and b can be ideally translated to the control of the common-mode frequency for an unbalanced-fed dual-polarized dipole array with dimensions D_x and H as shown earlier in Fig. 3.4.

3.3.2.1 Graphical Analysis

As Eq. (3.1) is transcendental, a graphical approach will be used to observe the behavior of the cut-off frequency by setting each function within the equation that is dependent upon k_x equal to one another and assuming the quantity B/Y_{01} is a constant parameter. The lateral dimension of the waveguide in the \hat{x} direction will be held constant at a fixed length a and can be seen from Fig. 3.5 to be $2L + s$, and the dimension in the \hat{z} direction, b , is held at half that length at $a/2$. In order to better quantify $f_{cut-off}$, a and b are given specific values of 3 mm and 6 mm, respectively.

To begin, Eq. (3.1) is split apart into three different equations seen at the top of Fig. 3.6 to observe the effects of the parameters. The two trigonometric functions containing k_x are plotted against one another over a discrete value of k_x for varying cases of s , L , and d (labeled within the figure) as shown in the top right charts containing the red/blue curves in each subfigure. It can be seen that as s increases (L decreases) and d decreases (the ridge grows in height), the red curves begin to rise at the low-end. Adversely, L decreasing causes the blue curve to begin to shift higher, so a trade-off would inevitably ensue to find a maximized low-end.

The difference of the two functions is plotted beneath in Fig. 3.6 with green curves and the x-axis is converted to frequency. The TE_{10} mode would normally be able to be quantified from finding where the curves become equal to zero, however, Eq. (3.1) has an additional component: the discontinuity susceptance, B/Y_{01} . The introduction of this factor enables an extra tuning parameter to effectively cancel the higher values at the low-end of the band. Despite this, it is difficult to quantify the exact value of B/Y_{01} . A graph of the discontinuity susceptance for varying d/b (where d is referred to as b') was quantified and measured over for certain values in [57] and is extracted to be shown in Fig. 3.7(a). The underlying concepts to be observed from this chart are that smaller values of d and taller ridges greatly enhance the discontinuity susceptance and

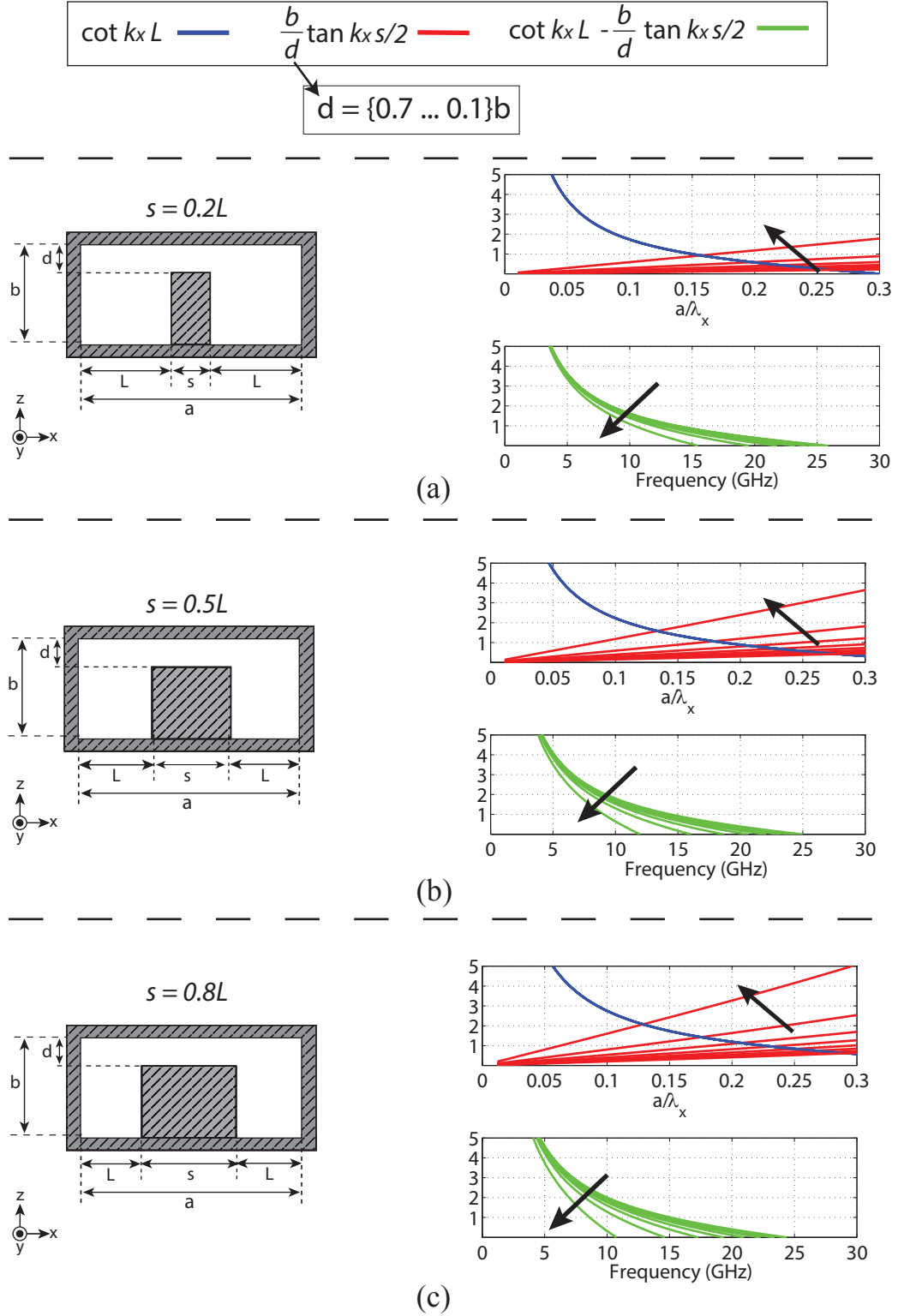


Figure 3.6. Charts of individual functions and their differences within the ridged waveguide equation for varying waveguide parameters s , L , and d and a fixed a and b (6mm and 3mm, respectively) versus the relative guide wavelength in the \hat{x} direction and frequency. (a) $s= 0.2L$; (b) $s=0.5L$; (c) $s=0.8L$.

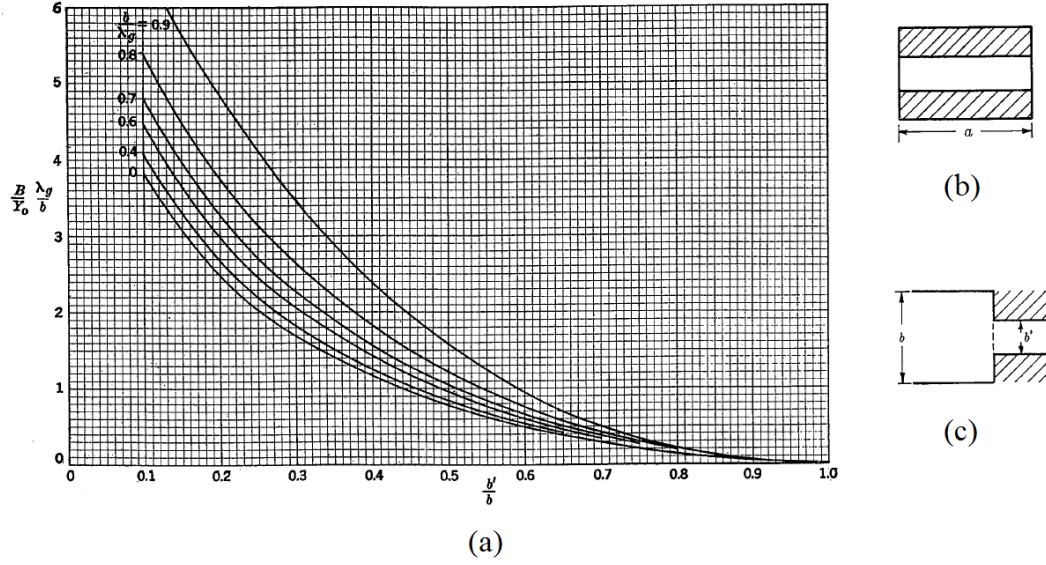


Figure 3.7. Ridged waveguides and discontinuity susceptance [57]. (a) Chart of the discontinuity susceptance, B/Y_{01} , within a ridged waveguide, for varying b versus $\frac{b'}{b}$; (b) Cross-section from a forward view of a ridged waveguide; (c) Side-view of a ridged waveguide with the discontinuity dimension b' .

that the contour of the curves appropriately compliment the difference charts shown previously in Fig. 3.6. From analyzing these graphs, an understanding of the physical phenomena controlling the cut-off frequency in ridged waveguides is understood and can now be analyzed for specific ridged waveguide configurations.

3.3.2.2 Key Factors for Lowering the Dominant Cut-off Frequency

From Eq. (3.1) and the graphical analysis in the preceding subsection, it can be seen that as the ratio of b/d increases (the ridge is taller) and/or the susceptance increases, the dominant TE_{10} mode cut-off frequency decreases. Several variations of the ridge height (b/d ratio) and its effect on the cut-off frequency were computed through full-wave analysis and plotted in Fig. 3.8. As expected, an increasing b/d ratio (increasing height) continually drops the fundamental cut-off frequency lower, suggesting that possibly a tall disconnected via could push the common-mode frequency downwards in an unbalanced-fed dual-polarized dipole array.

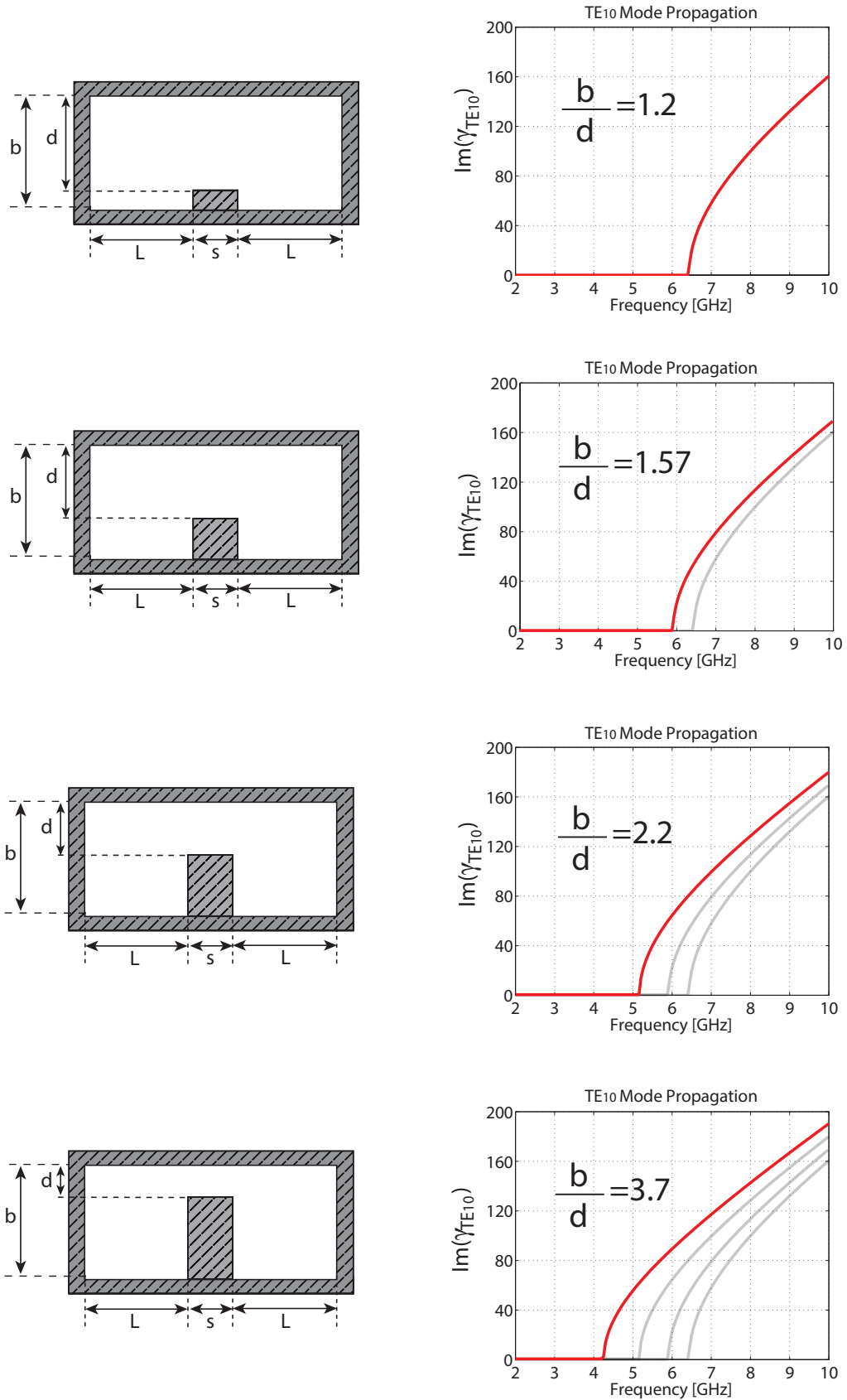
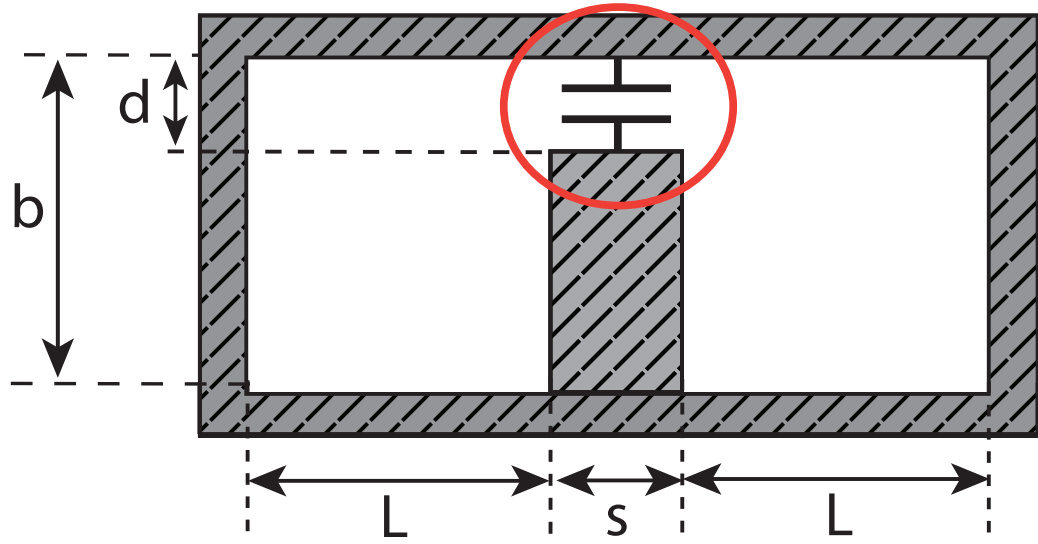


Figure 3.8. Variations of the ridge height (b/d ratio) and its effect on the propagation of the TE_{10} mode.

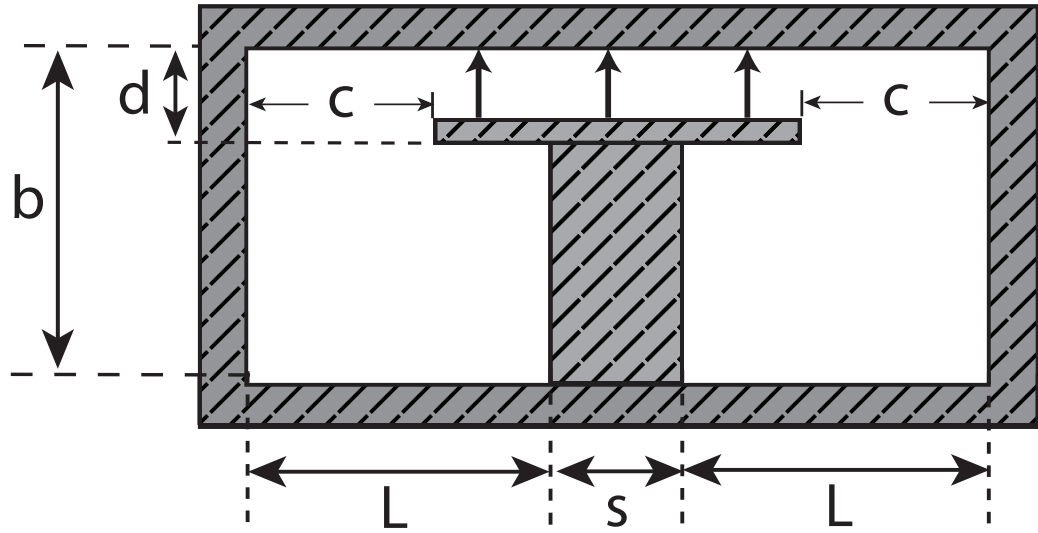
An important characteristic to notice within Fig. 3.8 is that for a linear increase in height, the rate at which the cut-off frequency decreases is non-linear. This can be directly attributed to the fact that the discontinuity susceptance is a function of the protrusion height. As the profile of the ridge nears the opposite wall, the discontinuity susceptance also strengthens to further drop the fundamental mode. From a circuit perspective, the value of B/Y_{01} from Eq. (3.1) is simply modeled as the capacitive junction between the ridge and the upper wall for this case as shown in Fig. 3.9(a). This suggests that if an additional degree of freedom was given to control B/Y_{01} , the cut-off frequency should be able to decrease even further. A simple implementation to accomplish this is to load the ridge with a parallel plate capacitor as depicted in Fig. 3.9(b), where the ratio of $\frac{2L+s}{2c}$ dictates the width of the parallel plate in comparison to the resonant waveguide dimension (similar to the b/d ratio). For instance, if c approaches zero, the parallel plate becomes nearly shorted to the broad-walls of the waveguide and a large amount of capacitance synthesized. Adversely, if c grows large and approaches L , it is virtually non-existent assuming the plate is thin. This ratio controlling c is varied for a constant b/d in Fig. 3.10 and the propagation constant of the fundamental mode is charted for each case. As expected from Eq. (3.1), synthesizing a larger capacitance for this scenario reduced the cut-off frequency even further and provides more physical insight into possible methods of dropping the common-mode frequency in unbalanced fed dipole arrays over a ground plane..

3.3.3 Common-Mode Mitigation with Capacitively-Loaded Vias

When unbalanced feeds are used to feed balanced radiator arrays above ground, it would be desirable to preserve the better low frequency performance of the no via, direct feeding arrangement of Fig. 3.11(a) in conjunction with the high frequency common-mode mitigation attained when shorting vias are present (PUMAv1) like in Fig. 3.11(b). Ideally, the goal in this work is to attain the better parts of the



(a)



(b)

Figure 3.9. A ridged waveguide with a loaded capacitance (discontinuity susceptance) and labeled dimensions. (a) Straightforward circuit representation to heighten the discontinuity susceptance; (b) Realized implementation to heighten the discontinuity susceptance.

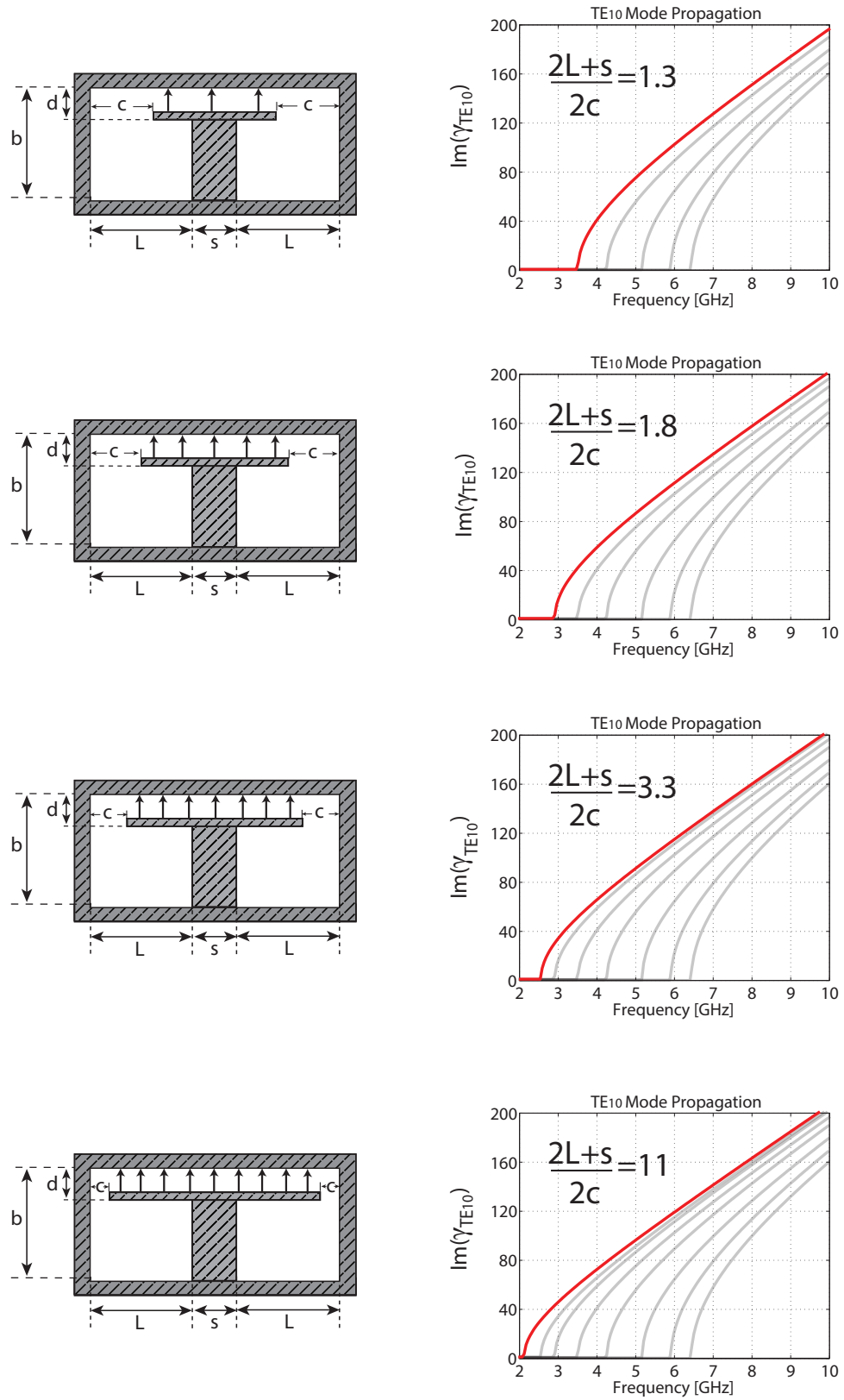


Figure 3.10. Variations of the waveguide ridge parallel plate ($\frac{2L+s}{2c}$ ratio) for a static ridge height and its effect on the propagation of the TE_{10} mode

VSWRs from each case displayed in Fig. 3.11(c) that if combined would lead to a bandwidth 3.5:1 as shown Fig. 3.11(d), where both the loop mode deteriorating the low band-edge and the common-mode splitting the high-end are both avoided.

Up until now, physical insights into the control of the fundamental mode of rectangular waveguides has been investigated and shown to obey the same trends as the problematic common-mode in unbalanced-fed dipole arrays. Specific attention was given to the manipulation of the fundamental mode in ridged waveguides with the variance of the ridge height and discontinuity susceptance, where the cut-off frequency decreased with increasing height and capacitance. Furthermore, no direct electrical connection is made across the guide cavity. *This gives rise to the idea that perhaps a similar approach could be used in unbalanced-fed dipole arrays to push the common-mode frequency beneath the operating band and not have its bandwidth inhibited by loop modes since no direct electrical connection is made.*

To pursue this idea, the PUMA unit cell is transformed to embody the ridged waveguide ideology as shown in Fig. 3.12(a) and Fig. 3.12(b) with isometric and cross-sectional views of the metallized components, respectively. The dipole fins and ground plane form the top and bottom walls of the waveguide with a width D_x , the feed lines of the dipoles enclose the structure and act like the broad walls in the waveguide with a height H , and the excited unbalanced feed line assumes the role of the feed probe in the waveguide. The ridge is emulated through introducing a disconnected via in the center of the unit cell of height h which is less than that of the feed line height H . The metallized components are practically etched and drilled through dielectric materials in multilayer PCB fabrication.

The effects of varying the height of a disconnected via centered in a unit cell is shown in Fig. 3.13. As expected, increasing the via height, h , shifts the common-mode frequency downwards from its initial position with no via present. Additionally, the rate at which the common-mode frequency decreases within the operating band

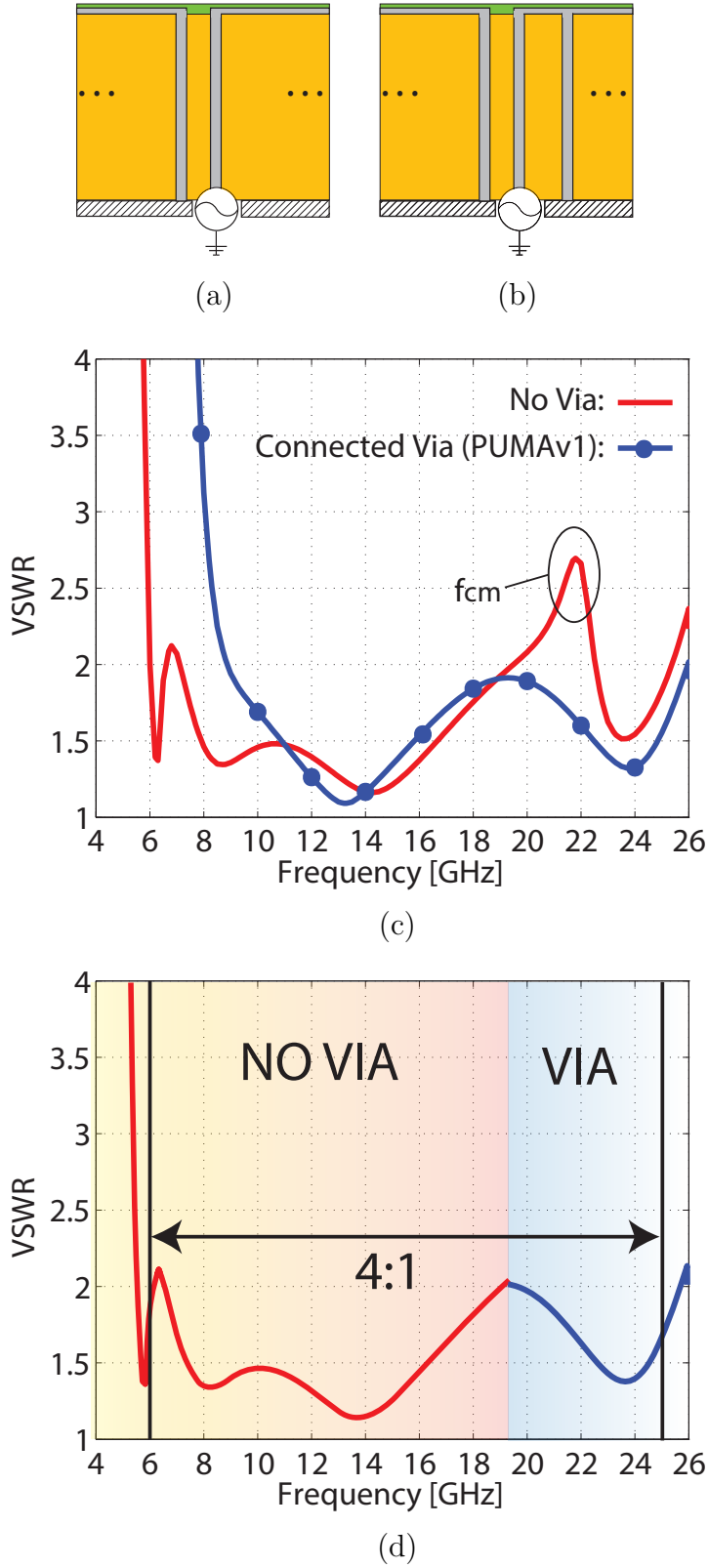


Figure 3.11. Comparisons of different feeding techniques for unbalanced fed arrays and their broadside VSWR vs. frequency. (a) No via; (b) Connected via (PUMAv1); (c) Broadside VSWR vs. frequency; (d) Desired broadside VSWR vs. frequency combining the better low-end when no vias are present and better high-end when vias are present (seen in (c)).

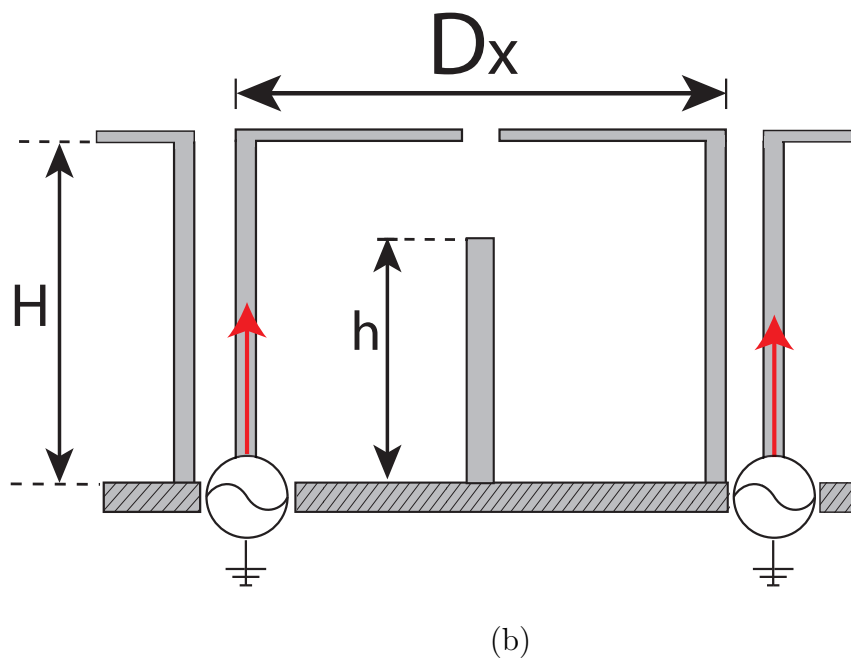
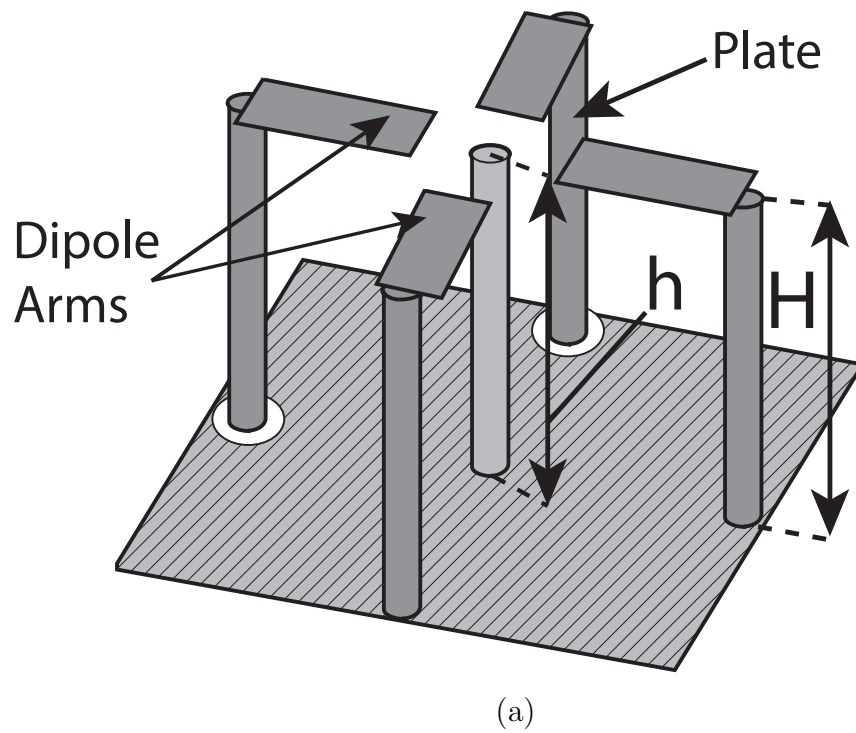


Figure 3.12. Different viewpoints of the PUMAv3 metallized components attempting to embody a ridged waveguide with a disconnected via. (a) Isometric view; (b) Side view with critical dimensions labeled.

is seen to be non-linear with respect to increasing via height and grows faster as the via approaches the height of the dipole arms, H . This is due to increasing the discontinuity susceptance (capacitance), B , between the dipole arms and the via itself, likewise governed by the reduction of the cut-off frequency in ridged waveguides in Eq. (3.1). Despite confirming the suspicion that decreasing the common-mode frequency with disconnected vias mimicks that of lowering the cut-off frequency in rectangular waveguides with metallic ridges, the frequency low-end is only reduced to approximately 10 GHz with a via height that is 97% of the dipole height as seen in Fig. 3.13. Consequently, the disconnected via approach yields lower bandwidth than that of the connected shorting via method ($\approx 2.5:1$ to $3:1$) and additional tactics are necessary to reduce the common-mode frequency further. Furthermore, it is possible to modify the arms to allow the via to proceed above the dipole layer without connection and achieve more low-end common-mode mitigation, but this becomes dangerous as the disconnected via will begin to radiate at a quarter-wavelength due to a monopole mode resonance. Nonetheless, a better solution exists to maximize bandwidth.

Although the common-mode resonance still resides within the operating band while reaching the maximum via height, increasing the discontinuity susceptance has yet to be attempted, giving credible hopes in our pursuit. From Eq. (3.1), a positive value of B will also contribute to lowering the cut-off frequency of a rectangular waveguide, which directly translates to synthesizing more capacitance between the dipole arms and the disconnected via as shown in Fig. 3.14. To realize this capacitance, a metallic plate of radius r_p is loaded on top of the disconnected via to provide a capacitive 'top-hat' as shown in Fig. 3.15(a) and Fig. 3.15(b). A circular plate was chosen for design simplicity, but other shapes such as a square or rectangle are also viable without any known restrictions. Parametric sweeps for different disconnected via heights and plate radii are plotted within Fig. 3.16, where the underlying trend

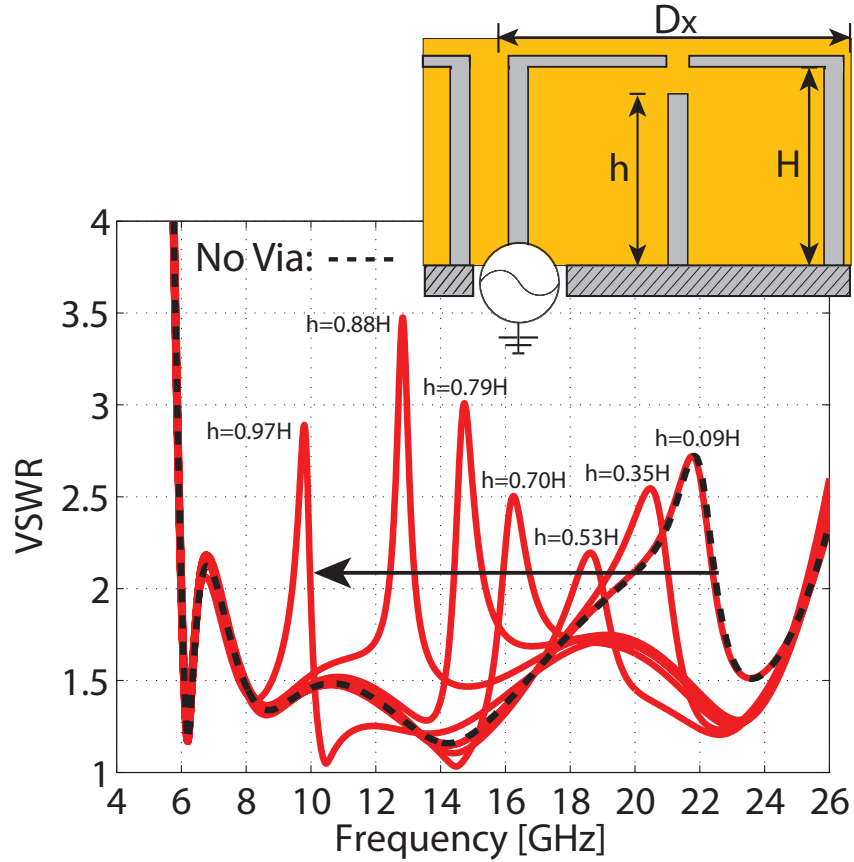


Figure 3.13. Effect of varying the height of a disconnected via for a PUMAv3 array on the broadside VSWR. The via is centered underneath the dipole tips (centered on the unit cell). The common-mode frequency shifts downwards with increasing via height, whereas the low end region remains unaffected.

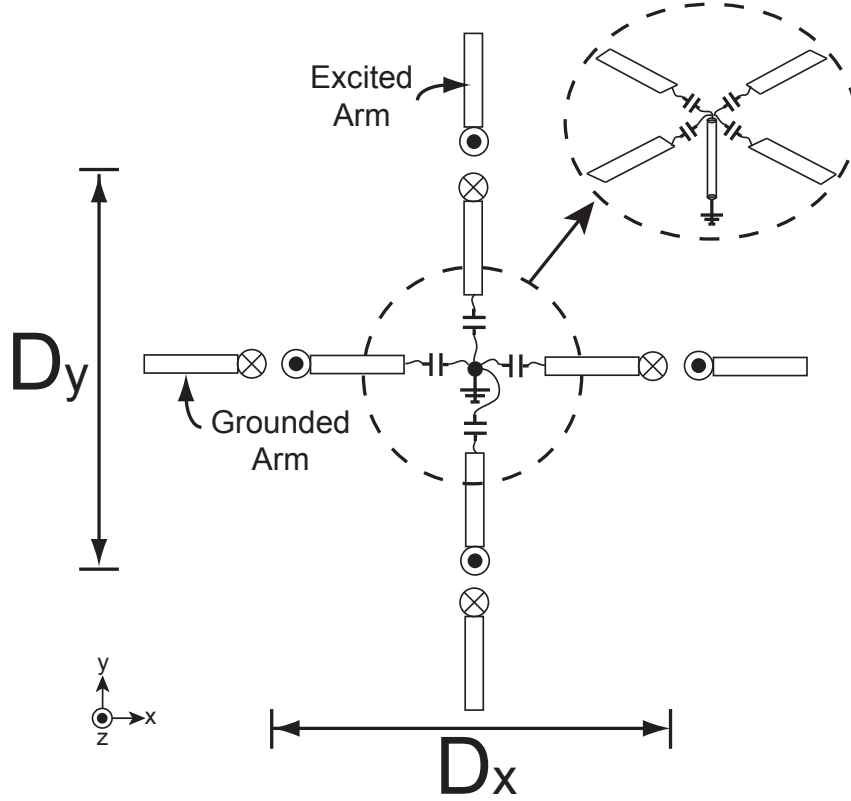


Figure 3.14. Top-view of a PUMAv3 unit cell highlighting the important capacitive junctions between the disconnected via and dipole arms.

is that a taller via and a larger plate (higher capacitance) shifts the common-mode downwards further. In fact, within Fig. 3.16(c) and Fig. 3.16(d), the common-mode frequency is pushed entirely below the operating band. However, the extremely close proximity of the metallic plate to the dipole arms is seen to deteriorate matching levels as shown in Fig. 3.16(d) by oversaturating the capacitance. Thus, design emphasis must be placed upon optimizing low-end performance by pushing f_{cm} below the band but while maintaining proper VSWR.

Finally, to highlight the improved performance from these capacitively-loaded vias, a comparison of the active reflection and port transmission for different via configurations for the same baseline dipole array geometry is shown in Fig. 3.17(a) and Fig. 3.17(b), respectively. The capacitively-loaded via provides a 50% bandwidth

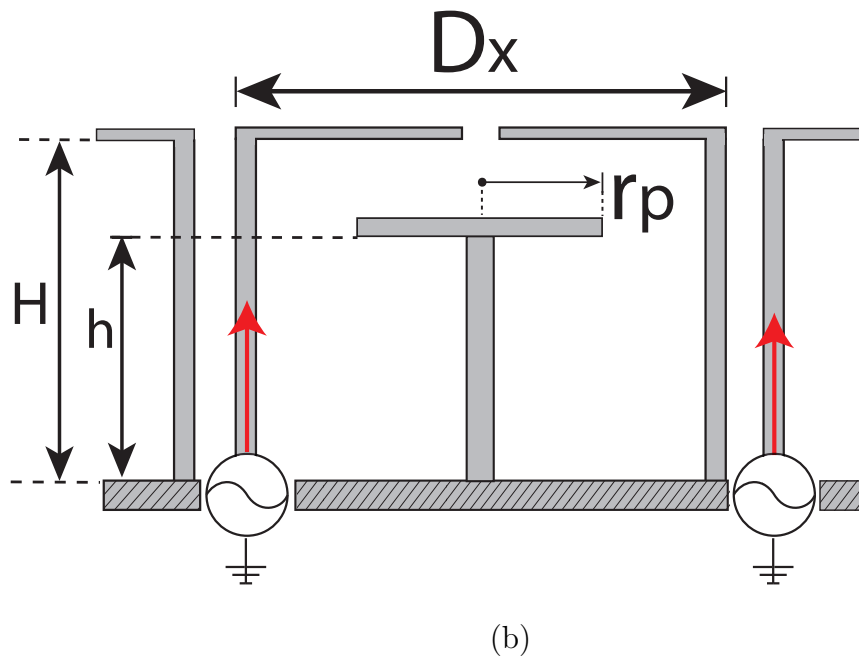
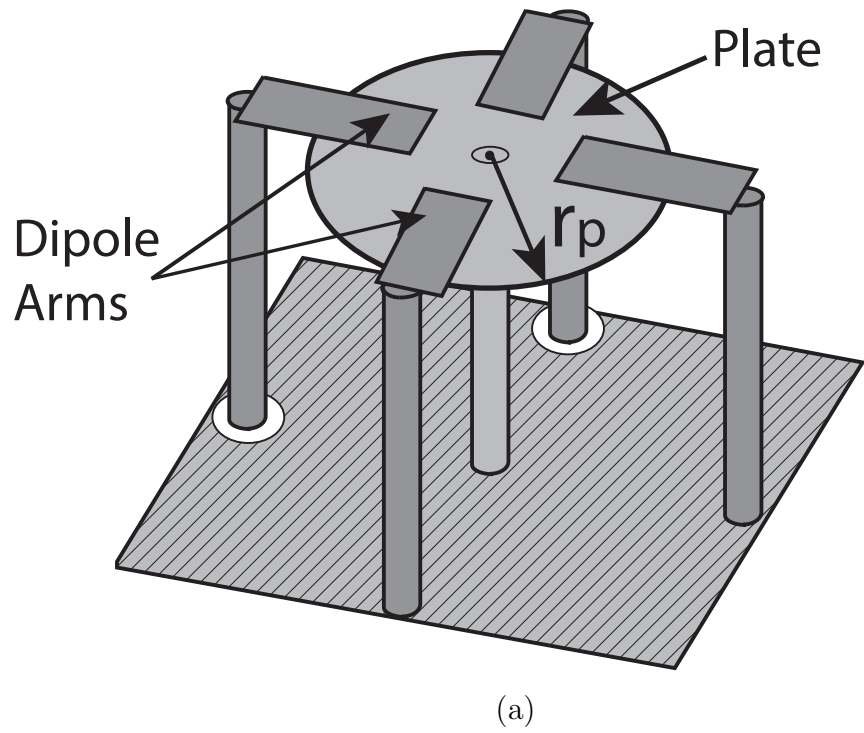


Figure 3.15. Different viewpoints of the PUMAv3 metallized components with the added metallic plate onto the disconnected via. (a) Isometric view; (b) Side view with critical dimensions labeled.

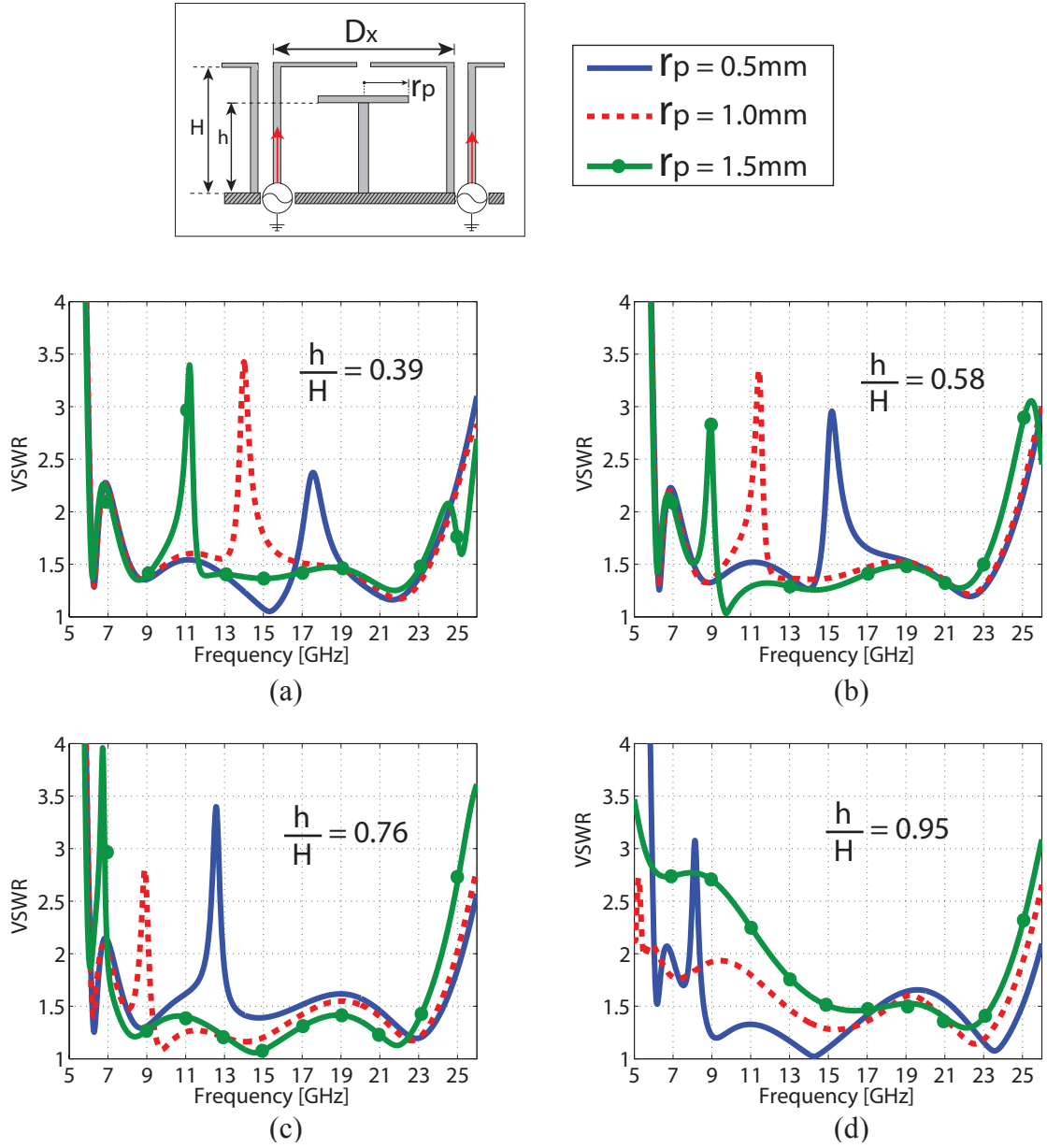


Figure 3.16. Infinite array VSWR performance for a PUMAv3 array with varying disconnected via heights and plate radii. (a) $h/H = 0.39$; (b) $h/H = 0.58$; (c) $h/H = 0.76$; (d) $h/H = 0.95$.

enhancement compared to the original PUMAv1 with connected vias (3:1 to 4.5:1). With proper tuning of the via height and plate radius, the low-band edge itself can be dropped lower than that of when no shorting vias are present and any common-mode phenomena will be pushed below the operating band while maintaining good impedance levels, completely mitigating the broadside catastrophic common-mode plaguing unbalanced fed arrays and improving the bandwidth altogether.

3.3.4 Common-Mode Predictions using the Ridged Waveguide Model

In the previous sections, motivation and application of the ridged waveguide model for common-mode mitigation in unbalanced-fed dual-polarized dipole arrays with a ground plane was presented with good results. As in Section 3.3.1, a high degree of accuracy can be achieved when predicting the common-mode frequency through using waveguide models for cases that use/don't use shorting vias(< 3%). It would be desirable to thus extend this to models using capacitively-loaded vias and observe the accuracy.

To compliment this for the capacitively-loaded via approach in the PUMAv3, the feasibility of common-mode frequency prediction with ridged waveguide models will be explored using the models depicted in Fig. 3.18. The infinite dual-polarized unbalanced-fed dipole array uses the capacitively loaded via described previously in this section as shown in Fig. 3.18(a), and an unbalanced-fed ridged waveguide with the same wall and ridge dimensions is used for comparison as shown in Fig. 3.18(b). Both topologies are filled with a dielectric material of $\epsilon_r = 1.96$. The minor impedance variations indicative of the common-mode frequency are used as markers for f_{cm} on VSWR scales for the PUMAv3 arrays and are compared to the dominant TE_{10} cut-off frequencies (labeled as f_c for this case) for varying plate radii and ridge heights for a ridged waveguide as charted in Fig. 3.19, Fig. 3.20, and Fig. 3.21. All varying

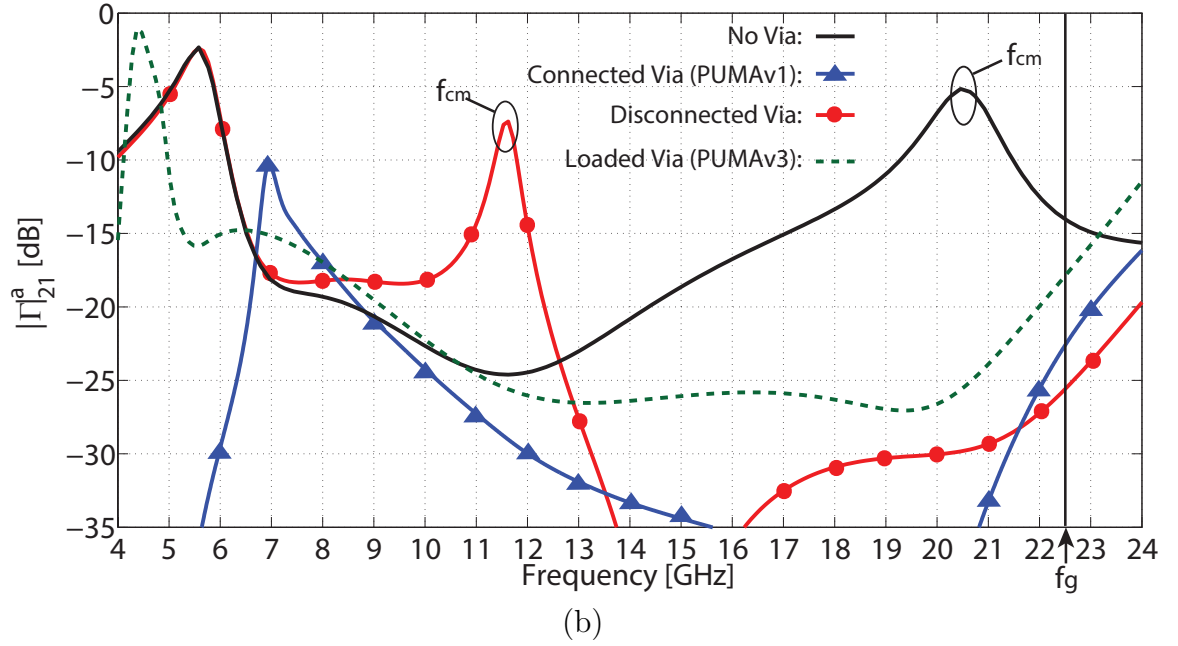
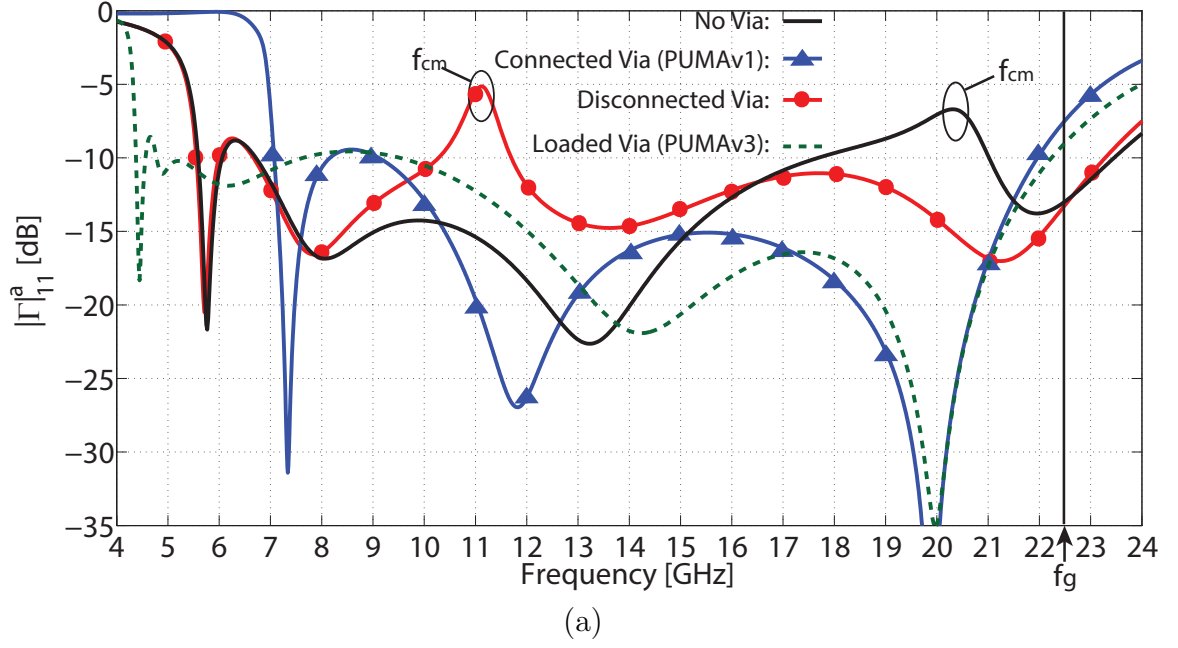


Figure 3.17. Infinite dual-polarized array broadside active reflection and orthogonal-port transmission coefficient magnitudes for different via configurations. (a) Reflection coefficient (return-loss); (b) Orthogonal port transmission coefficient (isolation).

dimensions are referred to λ , where λ is the grating-lobe frequency at half-wavelength spacing for this case.

The data from the charts in Fig. 3.19, Fig. 3.20, and Fig. 3.21 is compiled into Table 3.3.4. It becomes clear that for small plate radii and ridge heights that the error between the two frequencies is very large, but for large plate radii and ridge heights the error is minimal ($< 2\%$). *This is expected due to the fact that the cut-off frequency in the ridged waveguide depends upon the capacitance in the lateral cross-section only (two-dimensional), whereas the common-mode frequency in the PUMAv3 array relies upon the capacitance between a circular plate and dipole layer in a cylinder-like volume (three-dimensional).* The capacitance increases at a faster rate for increasing radii (area of a circle is πr^2 !) and approaches the capacitive saturation of the ridged waveguide case. Therefore, the common-mode frequency can be predicted with high accuracy for configurations with large plates ($r_p \geq \lambda/8$) and large ridges ($d \leq \lambda/8$), closely obeying the physical properties of its ridged waveguide model and, for practical implementation, only large plates and ridges will be used to mitigate common-modes anyways. Additionally, the common-mode frequency can thus be numerically computed from graphical analysis like that of the ridged waveguide as previously discussed if the plates/ridges are large.

3.3.5 Superstrate Design

Similar to PUMAv1 and v2, both broadside and scan performance of the PUMAv3 can be improved using superstrate layers. Like preceding PUMA arrays, the PUMAv3 is designed using thick (approximately $\lambda_{high}/4$) soft-substrate PTFE layers that provide mechanical support for the feed lines and vertical electrical connections through plated vias. Due to this, surface waves can develop at certain angles to induce scan blindnesses within the scan volume and limit operation [52], making it necessary to carefully design the dielectric materials to avoid these detrimental effects. The

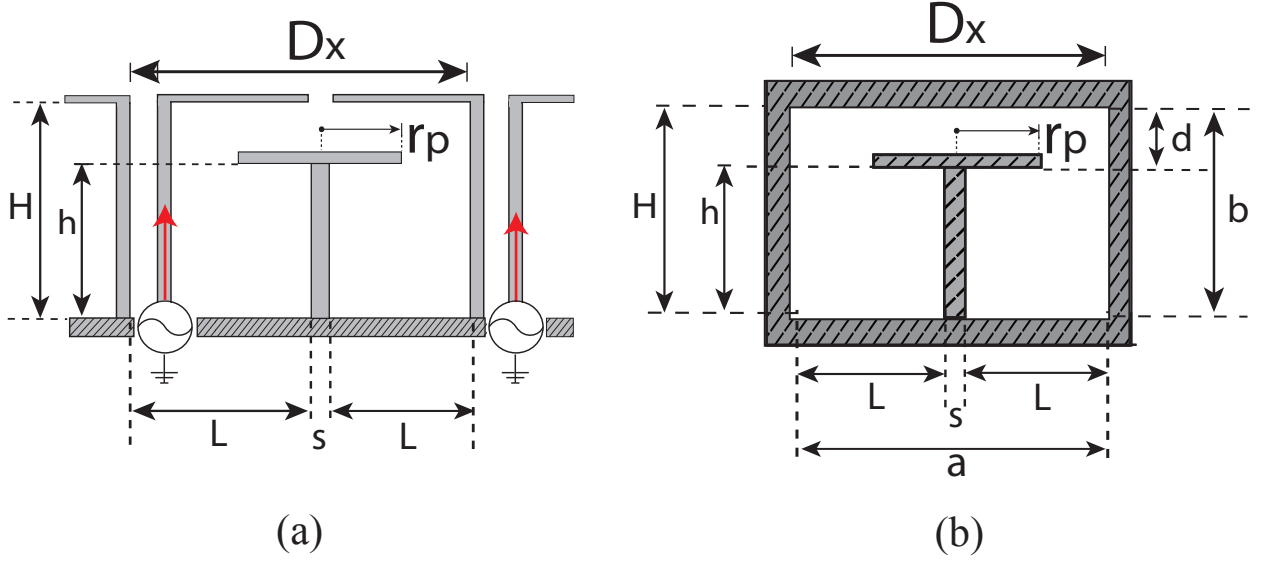


Figure 3.18. An unbalanced-fed dual-polarized dipole array with capacitively-loaded via (PUMAv3) translated to a ridged waveguide model with identical critical dimensions. (a) Unbalanced-fed dual-polarized dipole array with capacitively-loaded via (PUMAv3); (b) Ridged waveguide.

$r_p = \lambda/24$			
d	f_{cm} (GHz)	f_c (GHz)	% Error
$\lambda/6$	19.6	16.7	14.8
$\lambda/8$	18.5	15.0	18.9
$\lambda/12$	16.5	12.5	24.2
$\lambda/24$	15.5	10.5	32.2
$r_p = \lambda/12$			
d	f_{cm} (GHz)	f_c (GHz)	% Error
$\lambda/6$	18.7	16.0	14.4
$\lambda/8$	15.8	13.7	13.3
$\lambda/12$	13.1	11.1	15.3
$\lambda/24$	10.6	9.0	15.1
$r_p = \lambda/8$			
d	f_{cm} (GHz)	f_c (GHz)	% Error
$\lambda/6$	16.1	15.1	6.2
$\lambda/8$	12.3	12.3	0.0
$\lambda/12$	10.2	10.0	2.0
$\lambda/24$	8.1	8.0	1.2

Table 3.1. Calculated common-mode frequencies (f_{cm}) and dominant TE_{10} mode cut-off frequencies (f_c) for various plate radii (r_p) and ridge discontinuity gaps (d) within unbalanced-fed dual-polarized dipole infinite array and ridged waveguides of similar structure.

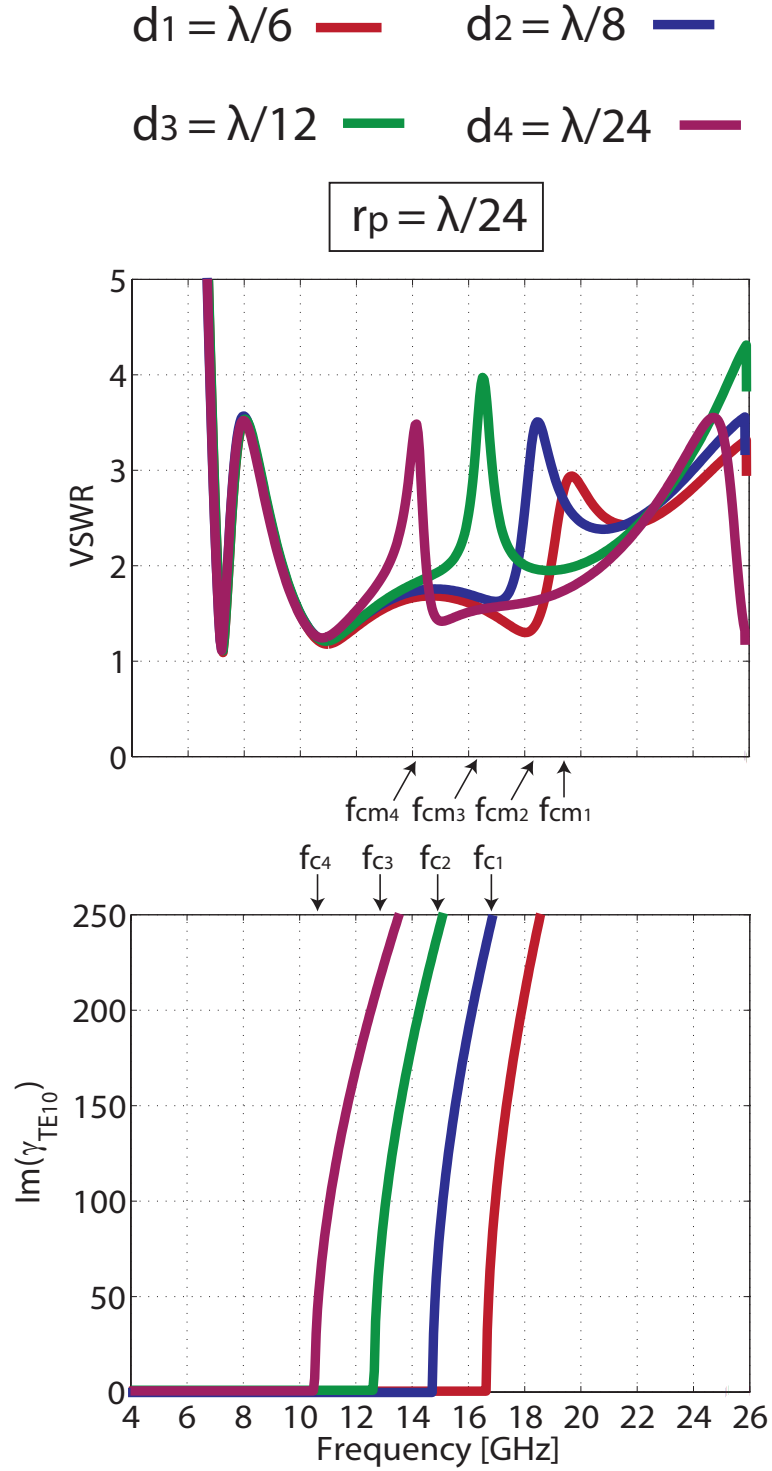


Figure 3.19. Comparison of common-mode frequencies in unbalanced-fed infinite dual-polarized dipole arrays with capacitively-loaded vias and dominant TE_{10} mode cut-off frequencies in ridged waveguides for varying ridge discontinuity heights d and plate radius $r_p = \lambda/24$. The critical dimensions of the two are identical as seen in Fig. 3.18.

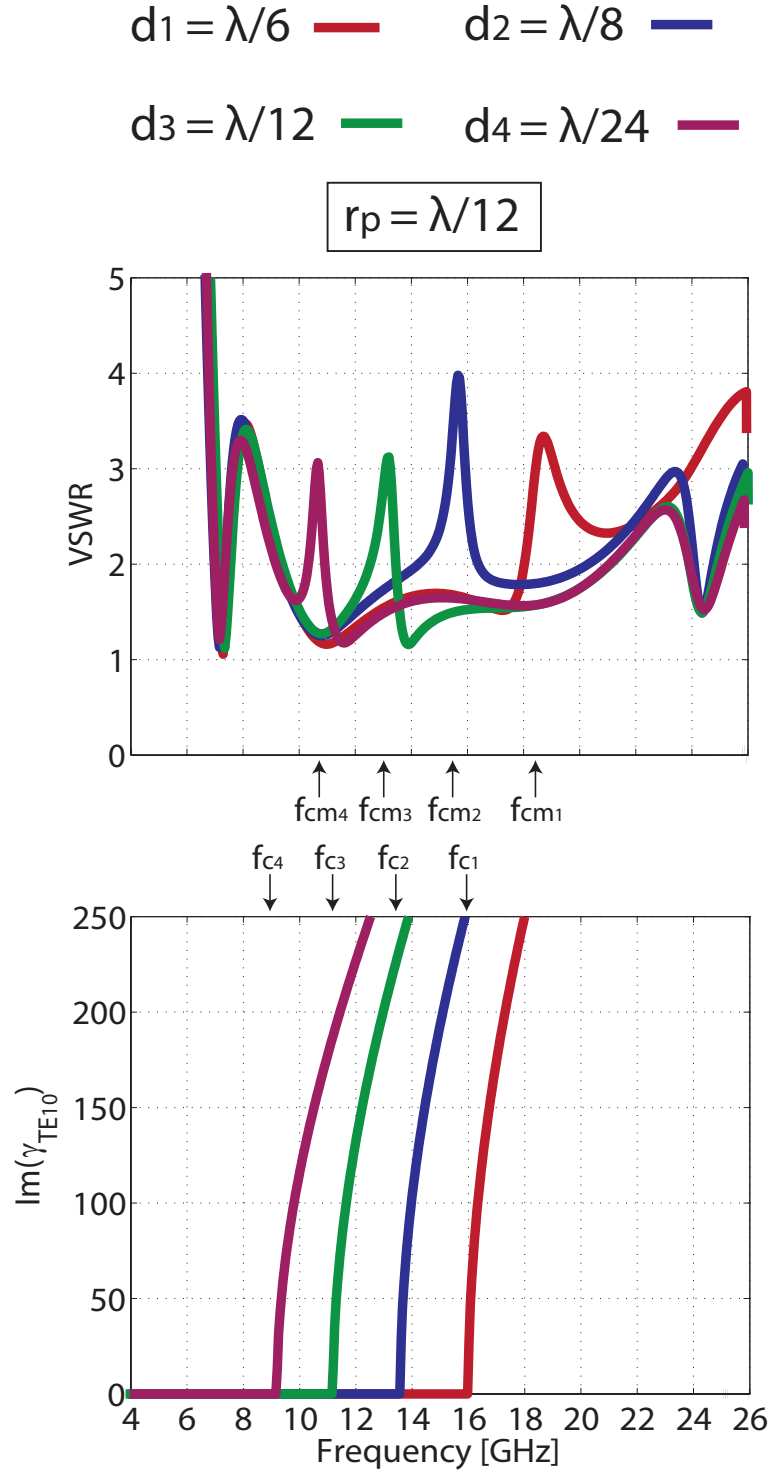


Figure 3.20. Comparison of common-mode frequencies in unbalanced-fed infinite dual-polarized dipole arrays with capacitively-loaded vias and dominant TE_{10} mode cut-off frequencies in ridged waveguides for varying ridge discontinuity heights d and plate radius $r_p = \lambda/12$. The critical dimensions of the two are identical as seen in Fig. 3.18

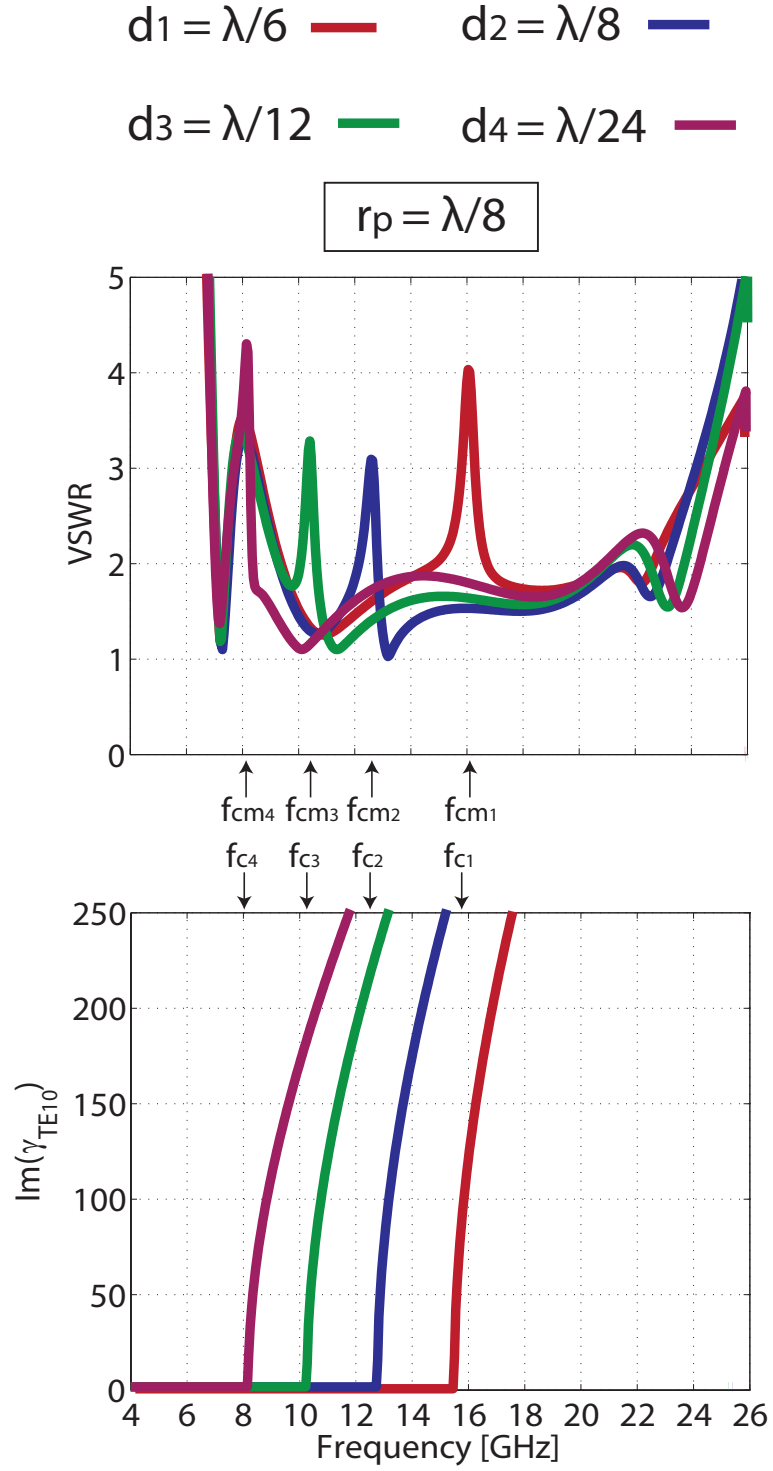


Figure 3.21. Comparison of common-mode frequencies in unbalanced-fed infinite dual-polarized dipole arrays with capacitively-loaded vias and dominant TE_{10} mode cut-off frequencies in ridged waveguides for varying ridge discontinuity heights d and plate radius $r_p = \lambda/8$. The critical dimensions of the two are identical as seen in Fig. 3.18

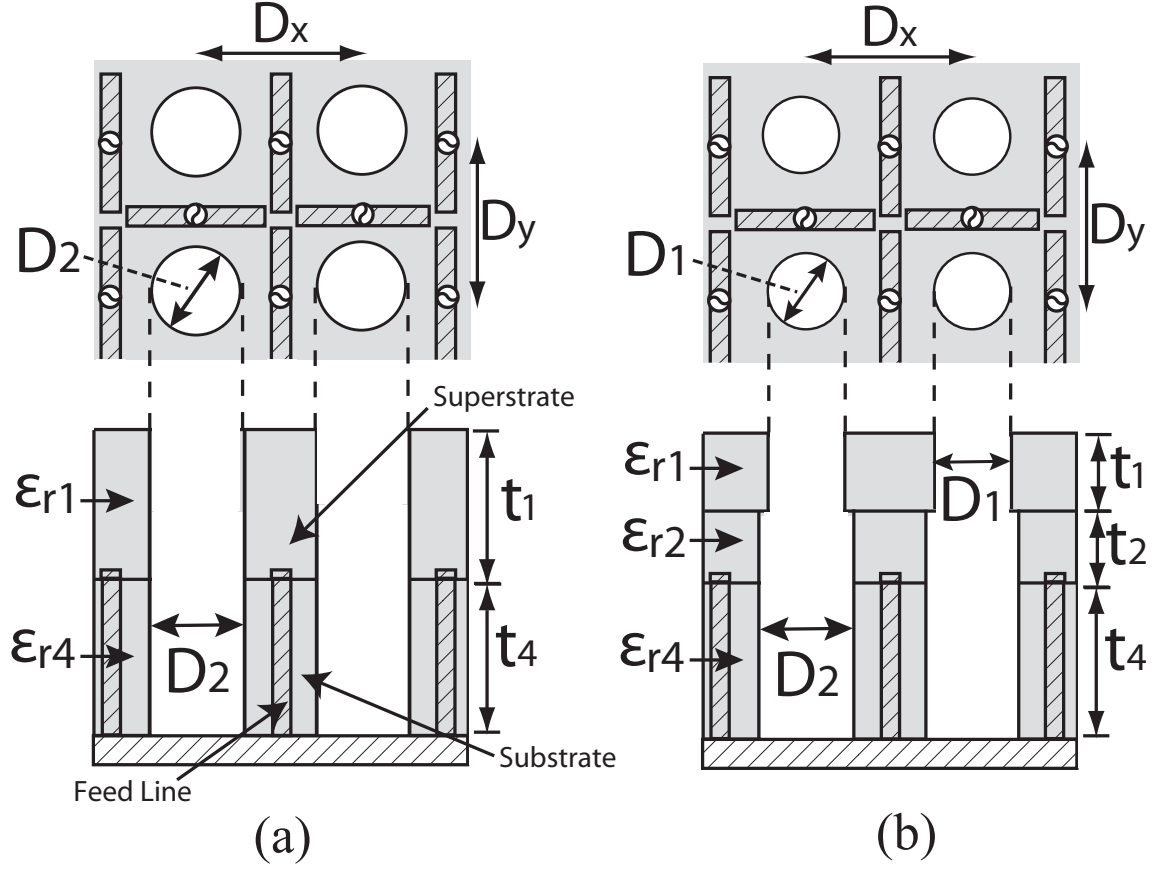


Figure 3.22. PUMA dielectric compositions with standard rectangular dipoles, omitting the metallization layer, modified from [1]. (a) PUMAv1 and PUMAv2 uniform superstrate composition; (b) PUMAv3 multi-layer superstrates, enabling more refined tuning for WAIM by breaking the superstrate into two different permittivity layers with different perforation sizes, D_1 and D_2 .

PUMAv3 dielectric compensation method adds onto that of the original PUMAv1 and PUMAv2 that uses a uniform superstrate as shown in Fig. 3.22(a) by splitting the superstrate into two separate layers as shown in Fig. 3.22(b). In doing so, more refined tuning is enabled for WAIM due to having more degrees of freedom with different perforation sizes, thicknesses, and permittivities between the two layers. Fig. 3.22(b) presents this technique with the PUMAv3 topology (feed vias, capacitive via (not visible)) using standard rectangular dipoles and highlights the several additional degrees of freedom available for precise matching.

The primary reasoning behind the necessity of redesigning the superstrate layer is that the PUMAv3 seeks to operate at 98% of the grating lobe frequency, f_g , while also increasing the overall bandwidth, making it difficult to achieve good impedance levels without surface waves deteriorating the high-end. As a measure of reference, Fig. 3.23 charts the magnitude of the reflection coefficient versus E-/H-plane scan angles at f_{high} (98% f_g) for a case where the PUMAv3 is loaded with a uniform permittivity superstrate ($\epsilon_r = 1.95$) of thickness t_4 and then loaded with various PUMAv3 superstrate configurations. More specifically, the PUMAv3 superstrate data varies the perforation diameter D_1 with fixed permittivities ($\epsilon_{r1} = 4.5$, $\epsilon_{r2} = 1.96$), thicknesses ($t_1 = t_2 = t_4/2$), and perforation diameter D_2 (standard PUMAv1 size). At this frequency ($f_{high} = 0.98f_g$), the uniform superstrate does alleviate the onset of early scan blindnesses in both planes, but the overall matching is severely degraded (even near broadside). When utilizing the PUMAv3 method and varying D_1 , a trade-off is seen to occur as the H-plane blindness location and impedance improves at the sacrifice of E-plane high-end matching and slight degradation of blindness angle. For the particular instance when $D_1 = 3$ mm, scanning out to 55° with $VSWR < 3$ ($|\Gamma| = 0.5$) is achieved, but, since the PUMAv3 introduces several new degrees of freedom, other configurations could produce better results. Design compromises must be made between adequate E-/H-plane active reflection coefficient magnitudes to yield a well-matched wide scan volume with an extremely low oversampling rate of the aperture. Additionally, the PUMAv3 loading scheme enables higher permittivity superstrates to be utilized that contribute to a 15% profile reduction in comparison to PUMAv1.

3.3.6 Conclusion

This section introduced the PUMAv3 class of arrays and its operational theory. Topological analogies were drawn between rectangular waveguides and unbalanced-

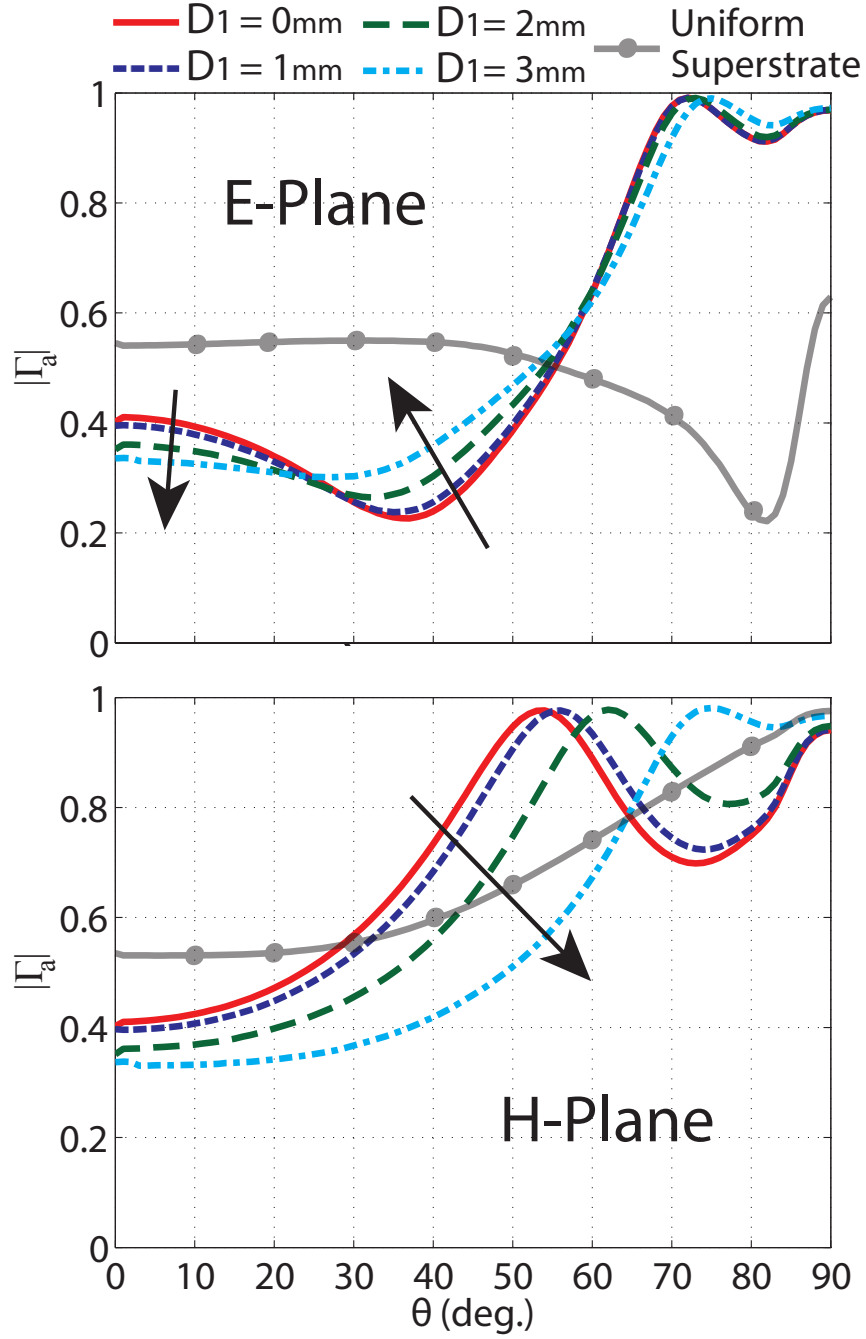


Figure 3.23. Magnitude of the active reflection coefficient, $|\Gamma_a|$, versus E-/H-plane scan angles at $f_{high} = 24.05$ GHz ($98\% f_g$) for varying the perforation diameter D_1 with fixed permittivities ($\epsilon_{r1} = 4.5$, $\epsilon_{r2} = 1.96$), thicknesses ($t_1 = t_2 = t_4/2$), and D_2 (5mm).

fed dual-polarized dipole arrays that led to highlighting the physical similarities between common-mode resonances and dominant cut-off frequencies. Ridged waveguides were studied as potential candidates for the suppression of common-mode resonances through pushing them beneath the low-band edge, as opposed to above the high-band edge with the conventional shorting vias of PUMAv1. High accuracy was achieved for calculating common-mode frequencies through ridged waveguide models when utilizing large metallic plates and ridges. Eventually, a new common-mode mitigation technique was innovated and presented that requires no electrical shorting of the dipole arms and avoids bandwidth-limiting low-end loop modes, ultimately engendering a 50% bandwidth enhancement over the PUMAv1.

CHAPTER 4

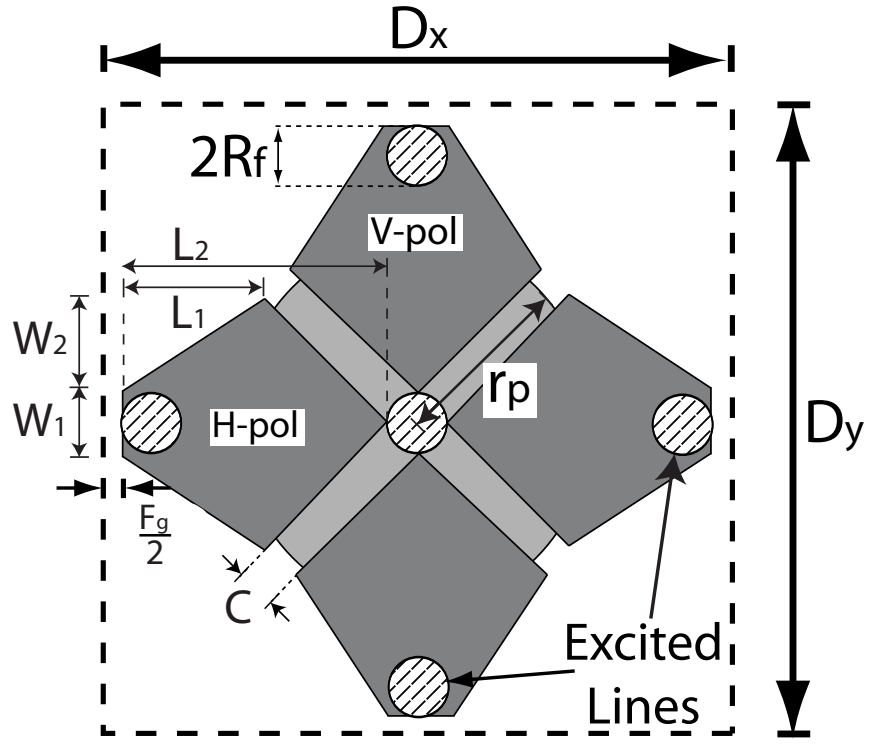
RESULTS

4.1 Introduction

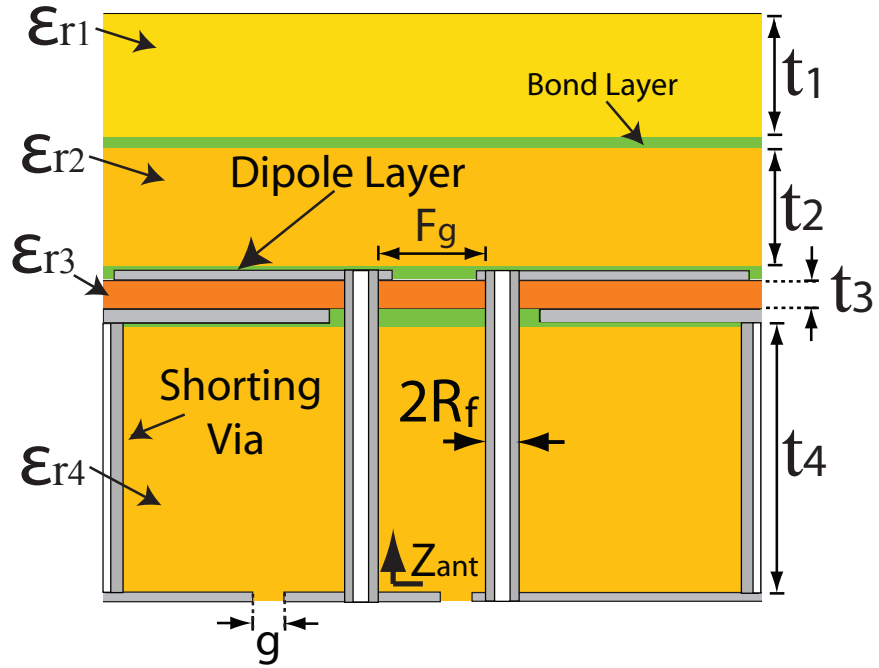
Using the theory and insights detailed thus far, a dual-polarized PUMAv3 array design will be presented that operates over 10.6-47.6 GHz (4.5:1) with good scan performance out to $\theta = 45^\circ$. The PUMAv3 array was simulated in an infinite array environment using Ansoft/Ansys HFSS [58]. All metallized components and vias were assumed to be PEC and only the standard dielectric materials discussed in the previous section were used. All results to be shown are referenced to $Z_0 = 50\Omega$ with one polarization excited and the other terminated to a $Z_0 = 50\Omega$ matched load. The port is excited utilizing a coaxial cable with a waveport and a PML is placed approximately $1.2\lambda_{high}$ above the array.

4.2 Array Geometry

The PUMAv3 array configuration for a $3 \times 3 \times 2$ unit cell was shown in Fig. 3.1 to retain the dual-polarized, dual-offset lattice of previous PUMA arrays but with several key differences to enhance frequency scalability and bandwidth. The most critical aspect is the capacitive synergy between the broad, diamond-shaped dipole arms and the disconnected capacitively-loaded via. With proper design, collaboration between both components achieves mitigation of in-band common-mode phenomena, avoidance of low-end loop modes induced from connected vias, and augmentation of the inter-element coupling.



(a)



(b)

Figure 4.1. Viewpoints of a PUMAv3 array unit cell. (a) Top view; (b) Cross-sectional view.

The PUMAv3 overcomes several limitations of preceding versions to enable mm-wave scalability. The former PUMA arrays produced inter-element coupling through the overlapping of orthogonally-polarized dipole arms on different sides of a thin soft-substrate layer to act as parallel plate capacitors. Unfortunately, the overlapping portions of the arms were forced to be small as they formed a “loop” that, when the mean circumference became approximately half a wavelength, spurred a new resonance as the array scanned in the H-plane when using connected shorting vias [5]. Due to this scanning limitation, the orthogonally-polarized dipole arms needed to be tightly-spaced to maximize capacitance and the minimum thickness for its soft-substrate layer was met at 21 GHz. The PUMAv3 topology offers heightened inter-element coupling to avoid the same manufacturing constraint and remains unaffected by the H-plane scanning limitation as the shorting vias are not connected. Together, the close-proximity of the arms and the plate synthesize a vast amount of inter-element coupling that allows for a thicker PTFE layer and larger gaps between the dipole arms themselves. The associated schematics and values for the designed PUMAv3 are found in Fig. 3.1 and Table 4.1, respectively.

The PUMAv3 utilizes a more complex superstrate loading scheme as discussed in Section IV-C. A cross-sectional view revealing the dielectric stackup is shown in Fig. 10(b). Dielectric layers 2 and 4 are comprised of Rogers 5880LZ ($\epsilon_r = 1.96$) and dielectric layer 3 consists of Rogers 6002 ($\epsilon_r = 2.94$), while all are perforated with cylindrical holes of radius $D_2 = 2.5$ mm. Additionally, the z-axis coefficient of thermal expansion of dielectric layer 3 is extremely low to ensure reliability of plated vias through the substrate containing the radiating arms and metallic plate. Dielectric layer 1 is made of Rogers TMM4 ($\epsilon_r = 4.5$) and is perforated with a cylindrical hole of radius $D_1 = 1.5$ mm. The thin bonding layers adjoining each layer are also included in analysis with a median ϵ_r of 2.6 and thickness of 2 mils. Furthermore, simulations include the dielectric loss tangent from all of these materials.

Table 4.1. 4.5:1 50 GHz Dual-pol PUMAv3 array dimensions

D_x [mm]	D_y [mm]	D_z [mm]	C [mm]
3.05	3.05	2.5	0.061 (2.5 mils)
t_1 [mm]	t_2 [mm]	t_3 [mm]	t_4 [mm]
0.525 (21 mils)	0.450 (18 mils)	0.127 (5 mils)	1.25 (50 mils)
ϵ_{r1}	ϵ_{r2}	ϵ_{r3}	ϵ_{r4}
4.5	1.96	2.94	1.96
L_1 [mm]	L_2 [mm]	W_1 [mm]	W_2 [mm]
0.628 (25 mils)	1.28	0.684 (27 mils)	1.33
R_f [mm]	g [mm]	F_g [mm]	r_p [mm]
0.127 (5 mils)	0.127 (5 mils)	0.190 (7.5 mils)	0.75 (29.5 mils)

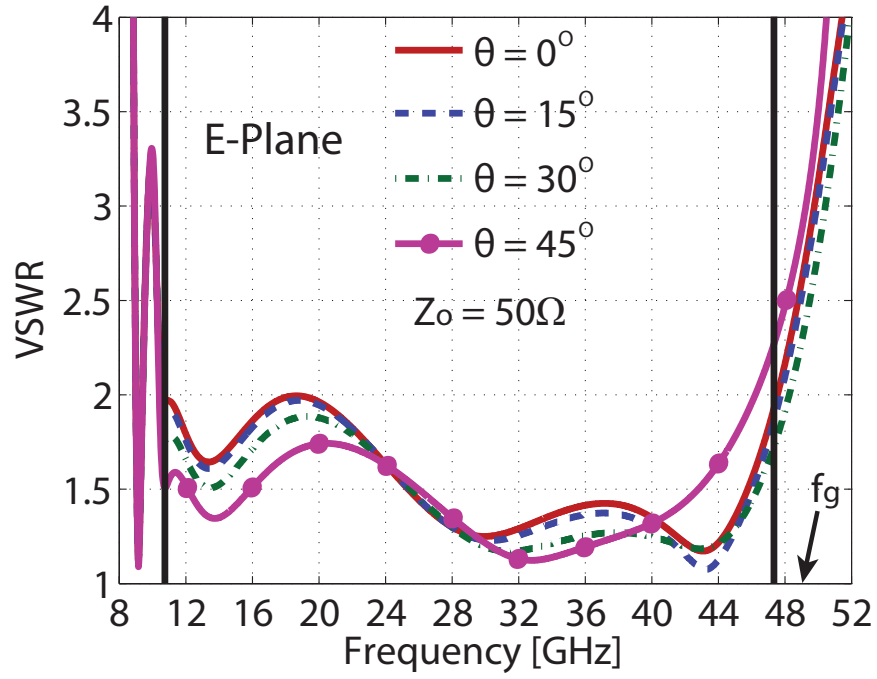
4.3 Numerical Results

4.3.1 Impedance vs. Scan

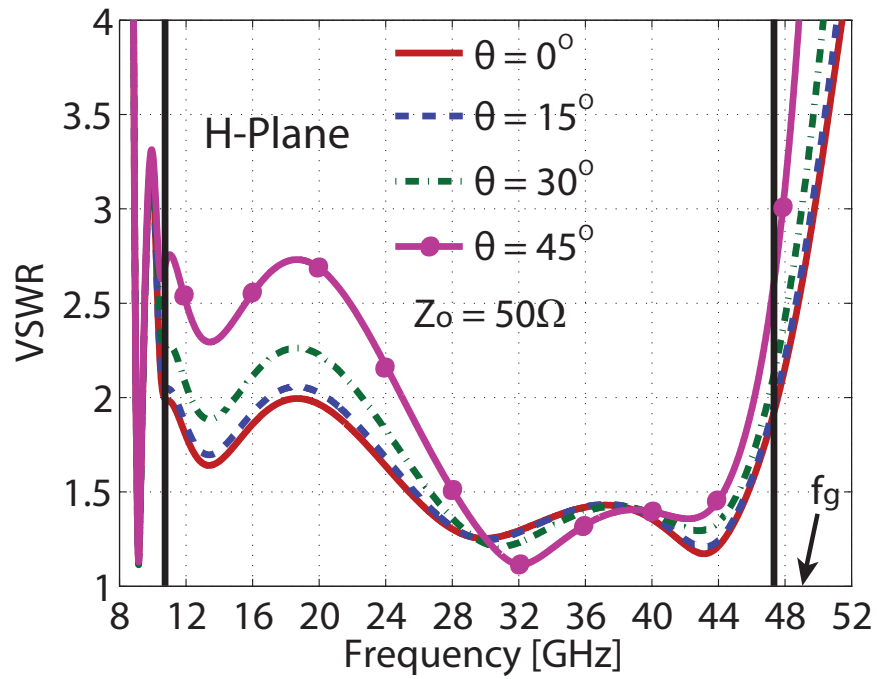
VSWR charts are shown for E-/H-plane scans out to $\theta = 45^\circ$ in Figs. 4.2(a) and 4.2(b), respectively. The vertical lines indicate the low (10.6 GHz) and high (47.6 GHz) band edges for a 4.5:1 bandwidth, and f_g signifies the grating lobe frequency corresponding to a spacing of $\lambda/2$ (49.2 GHz), resulting in a 97% f_{high}/f_g ratio. Predictions suggest a broadside VSWR < 2 and 45° E-/H-plane VSWR < 2.7 . Low-end impedance levels are the limiting factor in further reducing the low-band edge and are controlled by the inter-element coupling.

4.3.2 Cross-Polarization vs. Scan

Once the impedance performance has been studied, the far-field performance is next to be analyzed. In this section, co- and cross-polarizations are calculated assuming Ludwig's 3rd definition [59] by integrating the Poynting vector over the unit cell, and then normalizing the data to the incident power at the input port. The resulting co-/cross-polarized radiated powers per unit cell are plotted in Fig. 4.3 for broadside and E-/H-/D-plane scans at 45° . The co-polarized power is seen to remain near 0 dB throughout the entire band and drop by a maximum of 1.25 dB at the low-end. The cross-polarized power stays well below 15 dB for the majority of the



(a)



(b)

Figure 4.2. Infinite PUMAv3 array VSWR vs. frequency for varying scan angles. (a) E-plane scan; (b) H-plane scan.

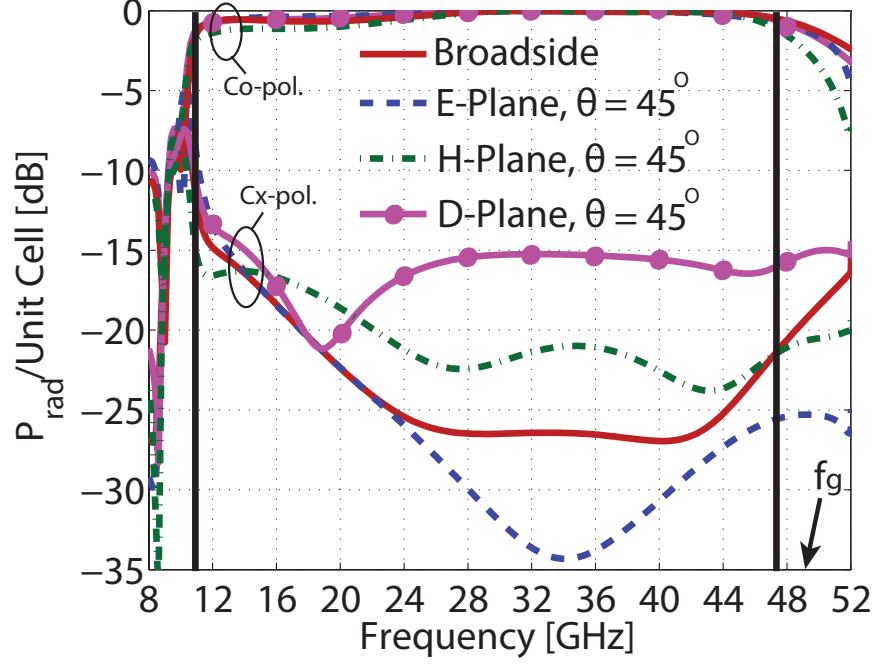


Figure 4.3. Infinite PUMAv3 array co- and cross-polarization (Ludwig’s 3rd definition [59]) radiated power vs. frequency for various scan planes.

band for all curves except the D-plane, which hovers around 15 dB. Low-band edge cross-polarized begins to rise with the E-plane scan reaching about -8.5 dB and the others staying below 10 dB.

4.3.3 Broadside Gain and Embedded Element Patterns

The broadside realized embedded element gain, $G_{embedded}$, is plotted against the ideal directivity, D , in Fig. 4.4, where

$$D = \frac{4\pi A}{\lambda^2} \quad (4.1)$$

and

$$G_{embedded} = \frac{4\pi A}{\lambda^2} (1 - |S_{11} + S_{21}|^2) \epsilon_D \quad (4.2)$$

The realized embedded element gain incorporates the mismatch, port coupling, and dielectric losses (ϵ_D) into the calculation, disregarding conductor losses as only PECs

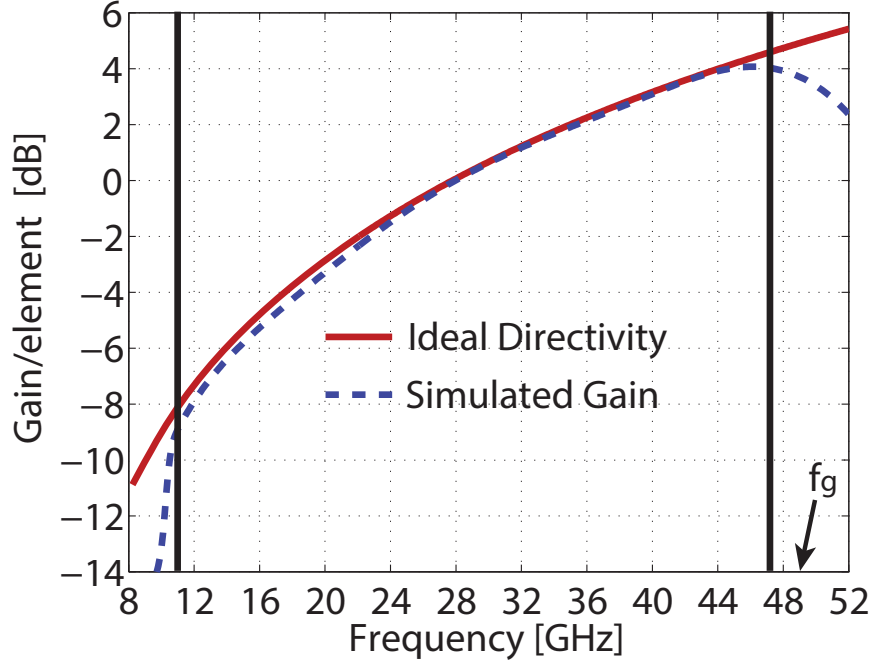


Figure 4.4. Infinite PUMAv3 array broadside realized gain (incorporates mismatch, port coupling, dielectric, and conductor losses) and ideal directivity vs. frequency.

were used. The realized gain remains nearly even with the ideal directivity for almost the entirety of the band. Realized gain drops by 0.2 dB at the low-end and 0.5 dB at the high-end due to mismatch and port coupling losses.

The normalized co-and cross-polarized embedded element patterns for E-plane, D-plane, and H-plane scans are plotted in Fig. 4.5, Fig. 4.6, and Fig. 4.7, respectively, for 15, 30, and 45 GHz. Co-polarization levels remain 15 dB above cross-polarization levels for all E-/H-plane scans. However, the D-plane is seen to highly deteriorate after 45° , implying that scanning to even wider angles poses a significant issue. Additionally, the D-plane cross-polarization is shown to increase with lower frequencies, indicating a possible limitation if the low-end bandwidth of the array were to further decrease.

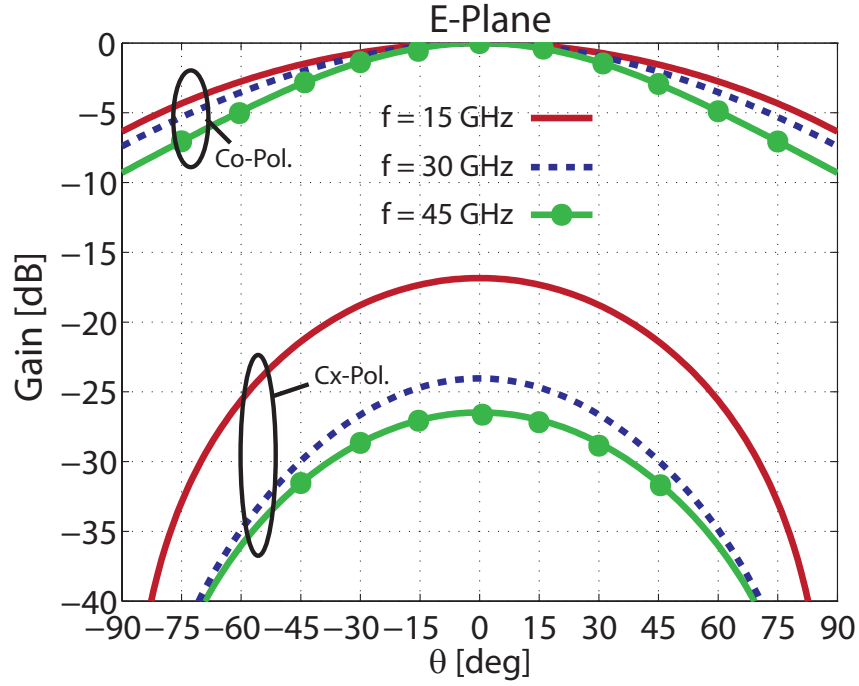


Figure 4.5. Simulated co-/cross-polarized normalized E-plane element patterns for different frequencies ($f = 15, 30, 45$ GHz).

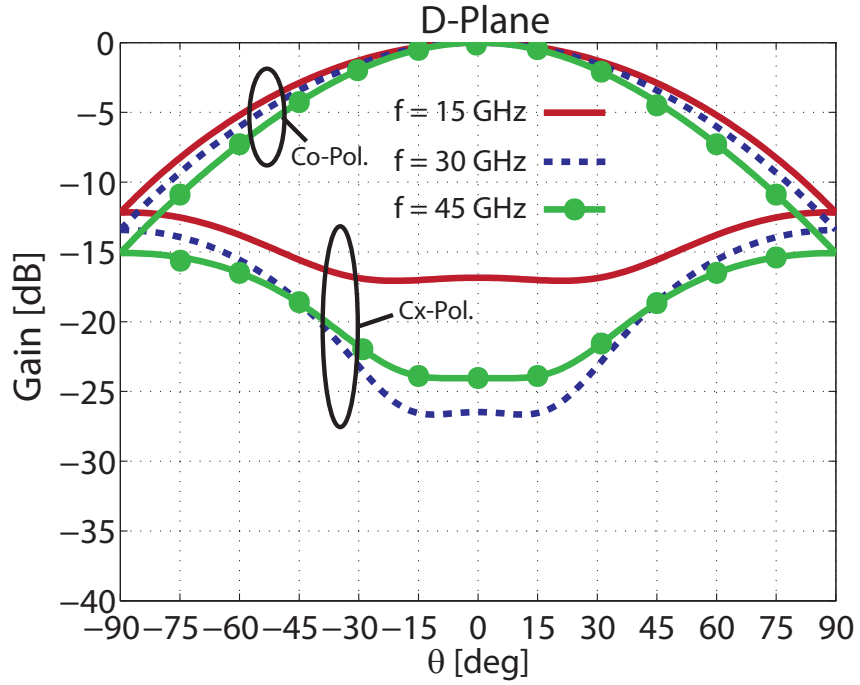


Figure 4.6. Simulated co-/cross-polarized normalized D-plane embedded element patterns for different frequencies ($f = 15, 30, 45$ GHz).

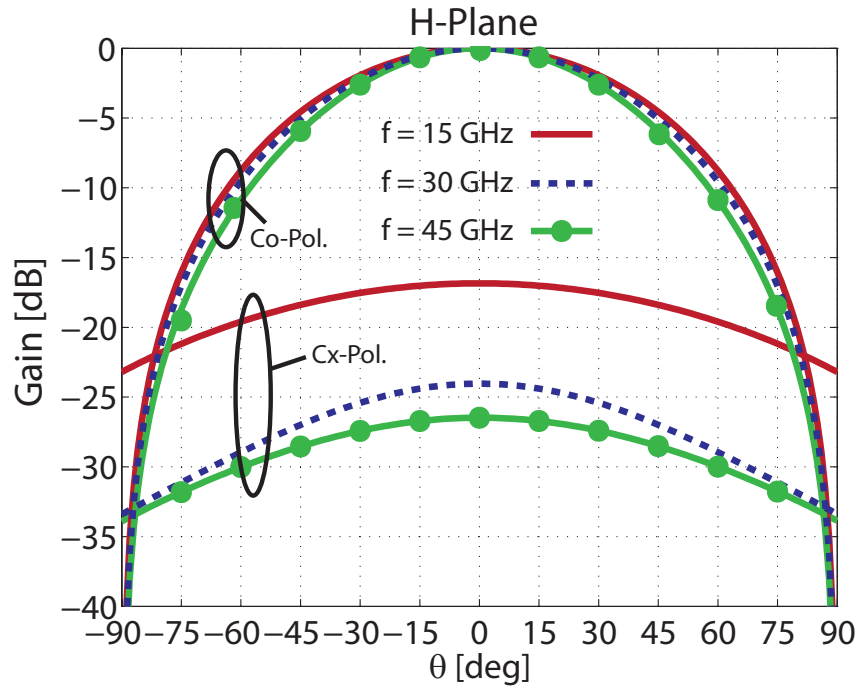


Figure 4.7. Simulated co-/cross-polarized normalized H-plane embedded element patterns for different frequencies ($f = 15, 30, 45$ GHz).

CHAPTER 5

EPILOGUE

This thesis presents a new class of PUMA arrays, termed PUMAv3, that offers improved bandwidth and mm-wave scalability while maintaining direct unbalanced feeding, modular assembly, and low-cost fabrication through standard microwave multilayer PCB manufacturing.

5.1 Conclusions

PUMA arrays were designed to make practical, low-cost UWB arrays readily available/affordable by enabling unbalanced feeding with a modular architecture. However, the bandwidth and frequency scalability of these arrays were ultimately limited by the shorting vias used to mitigate broadside common-mode resonances. This research investigated and proposed new techniques that mitigate broadside common-mode manifestations in unbalanced-fed dual-polarized dipole arrays without inhibiting bandwidth performance and frequency scalability.

The investigation focus was first placed upon the physical manifestation of common-modes in unbalanced-fed dual-polarized dipole arrays. It was shown that, as opposed to single-polarized counterparts, dual-polarized configurations exhibit a damped resonance behavior at the common-mode frequency due to the introduction of an orthogonal port. After analysis of the entire S-matrix, the net losses from return-loss and port coupling was shown to highly deteriorate co.-/cx.- polarization levels in-band at the common-mode frequency (approximately 80% of f_g). Consequently, the aperture

of the array would require 25% oversampling in the direction of each polarization and result in an increase of about 56% elements and T/R modules for a planar grid.

Using insights drawn from bandwidth enhancement methods from waveguides such as ridged waveguides, theory and background behind the design of the PUMAv3 array architecture was presented. The critical component of the PUMAv3 was shown to be the reconfiguration of the previously connected shorting via feeding scheme to a capacitively-loaded disconnected via placed underneath the orthogonal dipole end-tips. This arrangement pushes the detrimental common-mode below the operating band without inducing low-end limiting loop modes. Additionally, scan performance was optimized with a redesigned superstrate loading approach that resulted in a 30% profile reduction and helped achieve a 97% f_{high}/f_g ratio to minimize aperture oversampling.

Lasltly, a dual-polarized PUMAv3 infinite array was designed and its respective results suggested a 4.5:1 bandwidth over 10.6-47.6 GHz with broadside VSWR < 2 , scanned VSWR < 2.7 in all planes out to 45° , -10 dB cross-polarization out to 45° in the diagonal plane, and minimal losses in the broadside embedded element gain. As compared to the PUMAv2, the PUMAv3 doesn't require an external matching network to maintain its wideband performance and additionally operates 12% closer to f_g (85% to 97%), thus requiring 30% less elements and T/R modules for a planar aperture. The PUMAv3 ultimately offers a maximum operating frequency of more than double its predecessor, PUMAv1, while providing a 50% bandwidth improvement.

5.2 Future work

Several research directions could arise from the work proposed in this thesis:

- PUMAv2 arrays utilize a backplane matching network to extend bandwidth from 3:1 to 5:1 (67% increase), but frequency scalability becomes severely lim-

ited and the aperture is oversampled by a dramatic amount. It would be worthwhile to investigate a means of implementing a matching network that satisfies fabrication guidelines at mm-wave frequencies and does not impose issues upon integration with RF front-ends. Specifically, this would most likely translate to a stripline or coax design to preserve signal integrity and reduce electromagnetic interference with RF front-end components, posing further challenges to implement at higher frequencies as stripline conductors are thinner than that of microstrip. In addition, it would be interesting to observe if the same enhancement in bandwidth is possible with the PUMAv3 architecture, which would result in a 4.5:1 to 7.5:1 improvement if the 67% increase seen in the PUMAv2 was held true for the PUMAv3.

- A potential avenue to extend the research in this work would be to re-direct the design to ultra-wide scan (UWS) arrays instead of UWB arrays. Throughout this research it was found that bandwidth and scan angle appear to be related, implying that one could be traded for the other. A possible re-tuning of PUMAv3 with 2:1 bandwidth could potentially offer scan out to 75 or 80 degrees. A possible challenge in this direction would be to find methods that increase cross-polarized port isolation at wide angles, especially at the diagonal plane.
- Although the simulations predict strong performance over a 4.5:1 bandwidth with unbalanced feeding, a prototype must be built to validate performance. Completion and measurement of the prototype would mark a first step in the construction of a mm-wave UWB array. However, much work would need to be put into the development of a measurement approach, as mm-wave frequency array testing is not common and could pose implications.

- PUMA arrays seek to highly reduce the cost of UWB arrays while still offering comparable performance by designing a planar, modular, UWB element with unbalanced feeding. However, another cost consideration of arrays is reducing the amount of elements within a given area while still maintaining good performance to further drive down expenses. Wavelength-scaled arrays (WSAs) offer a significant reduction in the number of elements required to meet the same functionality as traditional arrays [60]. A possible research direction could delve into combining the low-cost and practical benefits of PUMA arrays with a WSA architecture, thus reducing not only cost involved with the elements themselves but also the entire array.
- The discovery of a non-bandwidth-limiting common-mode mitigation mechanism for unbalanced-fed dipole arrays presented within this work could be applied to other array architectures to enable and investigate the feasibility of unbalanced feeding and perhaps reduce cost. Additionally, PUMAv3 ideas may be applied to very small arrays, e.g. 2×2 , or even single antennas that are UWB.
- There appears to be a relationship between the VSWR level of the first "hump" and the extent to which the low end can be reduced. This is universal to all UWB arrays, but nobody has a physical understanding why, and nobody has a quantitative theory about it. That would be a possible theoretical direction.
- Simulations and results that were shown assumed an infinite array environment. In reality, all arrays to be constructed will be of finite extent and thus be subjected to truncation effects. A possible research direction could undergo an analysis of finite array effects on PUMAv3 arrays and observe any drawbacks/trade-offs that may inhibit operation.

BIBLIOGRAPHY

- [1] S. S. Holland, *Low-profile, modular, ultra-wideband phased arrays*. PhD thesis, University of Massachusetts Amherst, July 2011.
- [2] S. S. Holland and M. N. Vouvakis, “The planar ultrawideband modular antenna (PUMA) array.” U.S. Patent 20120146869, June 14, 2012.
- [3] S. S. Holland and M. N. Vouvakis, “A fully planar ultrawideband array,” *Antenna Applications Symposium, Allerton Park, Monticello, IL*, pp. 221–232, Sept. 2010.
- [4] S. Holland, D. Schaubert, and M. Vouvakis, “A 7-21 GHz dual-polarized planar ultrawideband modular antenna (PUMA) array,” *Antennas and Propagation, IEEE Transactions on*, vol. 60, pp. 4589–4600, Oct. 2012.
- [5] S. S. Holland and M. N. Vouvakis, “The planar ultrawideband modular antenna (PUMA) array,” *IEEE Trans. Antennas Propag.*, vol. 60, pp. 130 –140, Jan. 2012.
- [6] M. N. Vouvakis and D. H. Schaubert, “Vivaldi antenna arrays,” in *Frontiers in Antennas: Next Generation Design & Engineering*, McGraw Hill, F. B. Gross ed., 2011.
- [7] D. M. Pozar and D. H. Schaubert, “Microstrip antenna array design,” in *Microstrip Antennas: The Analysis and Design of Microstrip Antennas and Arrays*, John Wiley & Sons, 2011.
- [8] Military and Aerospace Electronics, “DARPA RF-FPGA program awards six contracts to develop programmable RF front-ends.” [http:](http://)

- [//www.militaryaerospace.com/articles/2012/08/darpa-rf-fpga.html](http://www.militaryaerospace.com/articles/2012/08/darpa-rf-fpga.html), Aug 2012.
- [9] G. Tavik, C. Hilterbrick, J. Evins, J. Alter, J. Crnkovich, J.G., J. De Graaf, I. Habicht, W., G. P. Hrin, S. Lessin, D. Wu, and S. Hagedwood, “The advanced multifunction rf concept,” *Microwave Theory and Techniques, IEEE Transactions on*, vol. 53, no. 3, pp. 1009–1020, 2005.
- [10] General Dynamics, “General Dynamics demonstrates wideband networking capability using JTRS HMS PRC-155 manpack radios.” http://www.generaldynamics.com/news/press-releases/detail.cfm?customel_dataPageID_1811=17737, May 2012.
- [11] Space War, “US army’s soldier radio waveform demonstrated on Raytheon’s next gen air and ground radios.” http://www.spacewar.com/reports/US_Armys_Soldier_Radio_Waveform_demonstrated_on_Raytheons_next_gen_air_and_ground_radios_999.html, Nov 2012.
- [12] Semantic Community, “Joint tactical radio system, network enterprise domain (JTRS-NED).” [http://semanticscommunity.info/Army_Weapon_Systems_Handbook_2012/Joint_Tactical_Radio_System,_Network_Enterprise_Domain_\(JTRS_NED\)](http://semanticscommunity.info/Army_Weapon_Systems_Handbook_2012/Joint_Tactical_Radio_System,_Network_Enterprise_Domain_(JTRS_NED)), Dec 2011.
- [13] Ed Walsh, “Felling antenna forests ONR’s AMRF-C.” <http://www.light-science.com/onrfell.html>, Oct 2002.
- [14] Defense Industry Daily staff, “The USAs RC-12X Guardrail SIG-INT Modernization.” <http://www.defenseindustrydaily.com/up-to-462m-for-rc-12-guardrail-modernization-03756/>, Mar. 2013.
- [15] DARPA Strategic Technology Office, “Mobile hotspots.” http://www.darpa.mil/Our_Work/STO/Programs/Mobile_Hotspots.aspx, Feb 2012.

- [16] DARPA Strategic Technology Office, “DARPA to develop mobile millimeter-wave backhaul networks.” http://www.darpa.mil/NewsEvents/Releases/2012/2012/02/10_DARPA_TO_DEVELOP_MOBILE_MILLIMETER-WAVE_BACKHAUL_NETWORKS.aspx, Feb 2012.
- [17] DARPA Strategic Technology Office, “Fixed wireless at a distance.” http://www.darpa.mil/Our_Work/STO/Programs/Fixed_Wireless_at_a_Distance.aspx, Feb 2013.
- [18] Office of Naval Research, “ONR electronic warfare & industry day.” <http://www.onr.navy.mil/~media/Files/Funding-Announcements/BAA/2011/11-006-Amendment-0001-Industry-Day.ashx>, Dec 2010.
- [19] K. Yemelyanov, N. Engheta, A. Hoorfar, and J. McVay, “Adaptive polarization contrast techniques for through-wall microwave imaging applications,” *Geoscience and Remote Sensing, IEEE Transactions on*, vol. 47, no. 5, pp. 1362–1374, 2009.
- [20] Camero staff, “Tactical through-wall imaging solutions.” <http://www.camero-tech.com/>, April 2013.
- [21] Y.-J. Park, S.-B. Cho, K.-H. Kim, and D.-G. Youn, “Development of an ultra wideband ground penetrating radar (uwb gpr) for nondestructive testing of underground objects,” in *Antennas and Propagation Society International Symposium, 2004. IEEE*, vol. 2, pp. 1279–1282 Vol.2, 2004.
- [22] M. Oyan, S.-E. Hamran, L. Hanssen, T. Berger, and D. Plettemeier, “Ultrawideband gated step frequency ground-penetrating radar,” *Geoscience and Remote Sensing, IEEE Transactions on*, vol. 50, no. 1, pp. 212–220, 2012.
- [23] Army-Technology staff, “Hidden agenda: IED detection using ultra-wideband radar.” <http://www.army-technology.com/features/>

- featureied-detection-ultra-wideband-microwave-radar-darpa-jieddo,
Jan. 2013.
- [24] T. Jin and Z. Zhou, “Ultrawideband synthetic aperture radar unexploded ordnance detection,” *Aerospace and Electronic Systems, IEEE Transactions on*, vol. 46, no. 3, pp. 1201–1213, 2010.
 - [25] A. Konovalenko, I. Falkovich, A. Gridin, P. Tokarsky, and S. Yerin, “Uwb active antenna array for low frequency radio astronomy,” in *Ultrawideband and Ultrashort Impulse Signals (UWBUSIS), 2012 6th International Conference on*, pp. 39–43, 2012.
 - [26] E. De Lera Acedo, N. Razavi-Ghods, L. Garcia, P. Duffett-Smith, and P. Alexander, “Ultra-wideband aperture array element design for low frequency radio astronomy,” *Antennas and Propagation, IEEE Transactions on*, vol. 59, no. 6, pp. 1808–1816, 2011.
 - [27] Chalmers staff, “Smart array antennas.” <http://www.chalmers.se/en/projects/Pages/Smart-array-antennas.aspx>, April 2013.
 - [28] T. Henriksson, M. Klemm, D. Gibbins, J. Leendertz, T. Horseman, A. Preece, R. Benjamin, and I. Craddock, “Clinical trials of a multistatic uwb radar for breast imaging,” in *Antennas and Propagation Conference (LAPC), 2011 Loughborough*, pp. 1–4, Nov. 2011.
 - [29] M. Bialkowski, D. Ireland, Y. Wang, and A. Abbosh, “Ultra-wideband array antenna system for breast imaging,” in *Microwave Conference Proceedings (APMC), 2010 Asia-Pacific*, pp. 267–270, Dec. 2010.
 - [30] J. J. Lee, S. Livingston, and R. Koenig, “A low-profile wide-band (5:1) dual-pol array,” *Antennas and Wireless Propagation Letters, IEEE*, vol. 2, no. 1, pp. 46–49, 2003.

- [31] J. Doane, K. Sertel, and J. Volakis, “A 6.3:1 bandwidth scanning tightly coupled dipole array with co-designed compact balun,” in *Antennas and Propagation Society International Symposium (APSURSI), 2012 IEEE*, pp. 1–2, July 2012.
- [32] W. Pickles and W. Dorsey, “Proposed coincident phase center orthogonal dipoles,” *Antenna Applications Symposium, Allerton Park, Monticello, IL*, pp. 106–124, Sept. 2007.
- [33] J. D. S. Langley, P. Hall, and P. Newham, “Balanced antipodal vivaldi antenna for wide bandwidth phased arrays,” *Microwaves, Antennas and Propagation, IEE Proceedings*, vol. 143, no. 2, pp. 97–102, 1996.
- [34] M. W. Elsallal, *Doubly-Mirrored Balanced Antipodal Vivaldi Antenna (Dm-BAVA) for high performance arrays of electrically short, modular elements*. PhD thesis, University of Massachusetts Amherst, Jan. 2008.
- [35] M. Elsallal, D. H. Schaubert, and J. B. West, “Advanced in the development of electronically scanned arrays of balanced antipodal Vivaldi antenna,” *Antenna Applications Symposium, Allerton Park, Monticello, IL*, pp. 1–16, Sept. 2008.
- [36] W. J. Otter, B. Pirollo, R. I. Henderson, and R. Lewis, “Multi-octave bava radiating elements for use in modular phased array antennas,” in *Antennas and Propagation, 2009. EuCAP 2009. 3rd European Conference on*, pp. 1324–1328, 2009.
- [37] E. De Lera Acedo, E. Garcia, V. Gonzalez-Posadas, J. Vazquez-Roy, R. Maaskant, and D. Segovia, “Study and design of a differentially-fed tapered slot antenna array,” *Antennas and Propagation, IEEE Transactions on*, vol. 58, no. 1, pp. 68–78, 2010.
- [38] S. S. Holland and M. N. Vouvakis, “The Banyan tree antenna array,” *Antennas and Propagation, IEEE Transactions on*, vol. 59, pp. 4060–4070, Nov. 2011.

- [39] M. Elsallal and J. Mather, “An ultra-thin, decade (10:1) bandwidth, modular “BAVA” array with low cross-polarization,” in *Antennas and Propagation (AP-SURSI), 2011 IEEE International Symposium on*, pp. 1980–1983, July 2011.
- [40] B. Munk, R. Taylor, T. Durharn, W. Croswell, B. Pigon, R. Boozer, S. Brown, M. M. Jones, J. Pryor, S. Ortiz, J. Rawnick, K. Krebs, M. Vanstrum, G. Gothard, and D. Wiebelt, “A low-profile broadband phased array antenna,” *IEEE Antennas and Propagation Society Int. Symp.*, vol. 2, pp. 448–451, June 2003.
- [41] H. A. Wheeler, “Simple relations derived from a phased-array antenna made of an infinite current sheet,” *IEEE Trans. Antennas Propag.*, vol. 13, pp. 506–514, July 1965.
- [42] P. Friederich, L. Pringle, L. Fountain, P. Harms, D. Denison, E. Kuster, S. Blalock, G. Smith, J. Maloney, and M. Kesler, “A new class of broadband planar apertures,” *Antenna Applications Symposium, Allerton Park, Monticello, IL*, pp. 561–587, Sept. 2001.
- [43] A. Neto and J. J. Lee, “Ultrawide-band properties of long slot arrays,” *IEEE Trans. Antennas Propag.*, vol. 54, pp. 534–543, Feb. 2006.
- [44] A. Neto and J. Lee, ““Infinite bandwidth” long slot array antenna,” *Antennas and Wireless Propagation Letters, IEEE*, vol. 4, pp. 75 – 78, 2005.
- [45] J. J. Lee, S. Livingston, and D. Nagata, “A low profile 10:1 (200-2000 MHz) wide band long slot array,” *IEEE Antennas and Propagation Society Int. Symp.*, pp. 1–4, July 5-11, 2008.
- [46] W. Croswell, T. Durham, M. Jones, D. Schaubert, P. Friederich, and J. Maloney, “Wideband antenna arrays,” in *Modern Antenna Handbook* (C. A. Balanis, ed.), John Wiley & Sons, 2008.

- [47] I. Tzanidis, K. Sertel, and J. Volakis, “Interwoven spiral array (ISPA) with a 10:1 bandwidth on a ground plane,” *Antennas and Wireless Propagation Letters, IEEE*, vol. 10, pp. 115–118, 2011.
- [48] M. Jones and J. Rawnick, “A new approach to broadband array design using tightly coupled elements,” *IEEE Military Communications. Conference 2007*, pp. 1–7, Oct. 2007.
- [49] J. R. Bayard, D. H. Schaubert, and M. E. Cooley, “E-plane scan performance of infinite arrays of dipoles printed on protruding dielectric substrates: coplanar feed line and E-plane metallic wall effects,” *IEEE Trans. Antennas Propag.*, vol. 41, pp. 837–841, June 1993.
- [50] B. Munk in *Finite Antenna Arrays and FSS*, Wiley, 2003.
- [51] J. Nelson and G. Stavis, “Impedance matching, transformers and baluns,” in *Very High-Frequency Techniques* (H. J. Reich and L. S. McDowell, eds.), McGraw-Hill Book Company, Inc., 1947.
- [52] D. Pozar and D. Schaubert, “Scan blindness in infinite phased arrays of printed dipoles,” *Antennas and Propagation, IEEE Transactions on*, vol. 32, pp. 602–610, June 1984.
- [53] E. Magill and H. Wheeler, “Wide-angle impedance matching of a planar array antenna by a dielectric sheet,” in *Antennas and Propagation Society International Symposium, 1965*, vol. 3, pp. 164–169, Aug. 1965.
- [54] B. Munk, *Finite Antenna Arrays and FSS*. Wiley, 2003.
- [55] S. Hopfer, “The design of ridged waveguides,” *Microwave Theory and Techniques, IRE Transactions on*, vol. 3, pp. 20–29, Oct. 1955.

- [56] S. Cohn, “Properties of ridge wave guide,” *Proceedings of the IRE*, vol. 35, pp. 783 – 788, Aug. 1947.
- [57] N. Marcuvitz in *Waveguide Handbook*, The Institution of Engineering and Technology, 1986.
- [58] Ansoft HFSS, version 14.0, www.ansoft.com.
- [59] A. Ludwig, “The definition of cross polarization,” *Antennas and Propagation, IEEE Transactions on*, vol. 21, pp. 116 – 119, Jan. 1973.
- [60] R. Kindt and M. Kragalott, “A wavelength-scaled ultra-wide bandwidth array,” in *Antennas and Propagation Society International Symposium, 2009. APSURSI '09. IEEE*, pp. 1–4, June 2009.